# T2K ND280
# Conceptual Design Report

*Version 1.0*
*November 6, 2005*

(T2K Internal Document)

**Abstract**

The T2K experiment will study oscillations of an off-axis muon neutrino beam between the JPARC accelerator complex and the Super-Kamiokande detector, with special emphasis on measuring the unknown mixing angle $\theta_{13}$ by observing the sub-dominant $\nu_\mu \rightarrow \nu_e$ oscillation. The neutrino energy spectrum, flavor content, and interaction rates of the unoscillated beam will be measured by a set of detectors located 280 m from the neutrino production target, and used to predict the neutrino interactions at Super-Kamiokande. The primary detector at the 280 m site is a magnetized off-axis tracking detector called the ND280. The ND280 detector elements are contained inside the magnet from the UA1 experiment. Inside the upstream end of this magnet sits a Pi-Zero Detector (P0D) consisting of tracking planes of scintillating bars alternating with lead foil. Downstream of the P0D three time projection chambers (TPCs), together with two fine-grained detectors (FGDs) consisting of layers of finely segmented scintillating bars, are optimized to measure charged current interactions. The P0D, TPCs, and FGDs are all surrounded by an electromagnetic calorimeter for detecting $\gamma$-rays that don't convert in the inner detectors, while the sides of the magnet are instrumented with scintillator to measure the ranges of muons that exit the sides of the ND280. In addition to the ND280 a separate array of iron/scintillator detectors called N-GRID will measure the on-axis neutrino beam profile at the 280 m site, while a set of muon monitor detectors located downstream of the beam dump will monitor the beam direction and profile by detecting high energy muons from pion decay. This conceptual design report details the physics requirements, motivations, and design considerations for each of these detectors.

# The T2K Collaboration
## *– ND280 group –*


J. Coulombe, C. Hearty, S. Oser, J. Wendland
*University of British Columbia, Canada*

T. Mathie, R. Tacik
*University of Regina, Canada*

J. Martin
*Toronto University, Canada*

P. Birney, A. Dowling, K. Fransham, C. Hansen, D. Karlen, R. Langstaff, M. Lenckowski, P. Poffenberger, M. Roney
*Univeristy of Victoria and TRIUMF, Canada*

P. Amaudruz, H. Coombes, W. Faszer, P. Gumplinger, R. Helmer, R. Henderson, I. Kato, P. Kitching, A. Konaka, L. Kurchaninov, A. Miller, K. Olchanski, R. Openshaw, J.M. Poutissou, R. Poutissou, F. Retiere, P. Vincent, S. Yen
*TRIUMF, Canada*

S. Bhadra
*York University, Canada*

P. Baron, J. Bouchez, D. Calvet, Ch. Cavata, P. Colas, E. Delagnes, A. Delbart, F. Druillole, M. Fechner, A. Giganon, Y. Giomataris, J.-Ph. Mols, F. Pierre, M. Zito
*DSM/Dapnia, CEA/Saclay, F-91191 Gif-sur-Yvette France*

M.G. Catanesi, E. Radicioni
*INFN, Sezione di Bari, Italy*

G. De Rosa, V. Palladino
*Univ. & INFN Napoli, Italy*

M. Laveder, M. Mezzetto
*Univ. & INFN Padova, Italy*

U. Dore, C. Gargiulo, P.F. Loverre, L. Ludovici, C. Mariani
*Universita' "La Sapienza" and INFN , Rome , Italy*

T. Takahashi
*ADSM, Hiroshima University, Hiroshima 739-8530, Japan*

Y. Fujii, Y. Hayato, A.K. Ichikawa, T. Ishida, T. Ishii, T. Kobayashi, T. Nakadaira, K. Nakamura, Y. Oyama, T. Sekiguchi, M. Tada, Y. Yamada
*KEK, Ibaraki 305-0801, Japan*

S. Aoki, T. Hara, A. Suzuki
*Kobe University, Hyogo 657-8501, Japan*

K. Nishikawa, T. Nakaya, M. Yokoyama, H. Tanaka, K. Hiraide, J. Kubota, K.Ezawa, Y. Kurimoto, Y. Kurosawa, T. Nobuhara, M. Taguchi, K. Matsuoka
*Kyoto University, Kyoto 606-8502, Japan*

K. Kaneyuki, H. Nishino
*ICRR, University of Tokyo, Chiba 277-8582, Japan*

T.Abe, H.Aihara, N.Hastings, M.Iwasaki, H.Kakuno
*University of Tokyo, Tokyo 113-0033, Japan*

J.Y. Kim, I.T. Lim
*Chonnam National University, Korea*

M.Y. Pac
*Dongshin University, Korea*

S.K. Nam
*Kangwon University, Korea*

W. Kim, V. Batourine
*Kyungpook National University, Korea*

I.G. Park
*Gyeongsang National University, Korea*

Y.D. Kim
*Sejong University, Korea*

S. Choi, E.J. Jeon, K.K. Joo, S.B. Kim
*Seoul National University, Korea*

Y.I. Choi, C.W. Park
*SungKyunKwan University, Korea*

M. Khabibullin, A. Khotjantsev, Y. Kudenko, B. Lubsandorjiev, V. Matveev, O. Mineev, Y. Mussienko, N. Yershov
*Institute for Nuclear Research, 60 October Revolution Pr. 7A 117312 Moscow, Russia*

M. Sorel, A. Cervera-Villanueva, J.J. Gomez-Cadenas, P. Novella, J. Catala, A. Tornero, E. Couce
*Valencia University, Spain*

S. Andringa, E. Fernández,T. Lux,F. Sánchez
*Universitat Autònoma de Barcelona, Institut de Fìsica d'Altes Energies, Bellaterra E-08193, Barcelona, Spain*

A. Blondel, P. Bene, A. Cervera, D. Ferrere, F. Masciocchi, E. Perrin, R. Schroeter
*DPNC, Section de Physique, University of Geneva CH1211 Geneva 4, Switzerland*

S. Boyd, P. Dornan, G. Hall, M. Raymond, I. Taylor, Y. Uchida, A. Vacheret, F. van Schalkwyk, D. Wark
*Imperial College London, London, UK*

Iain Bertram, Laura Kormos, Peter Ratoff
*Lancaster University, Lancaster LA1 4YB, UK*

C. Touramanis, J. Fry, R. Gamet, D. Payne, C. Chavez, P. Sutcliffe
*The University of Liverpool, Oliver Lodge Laboratory L69 7ZE, Liverpool, UK*

F.Di Lodovico, R.A. Owen, A. Poll, C. Williams
*Queen Mary, University of London, London E1 4NS, UK*

A. Belias, M. French, R. Halsall, T.C. Nicholls, G.F. Pearce, A. Weber
*CCLRC - Rutherford Appleton Laboratory, Chilton, Didcot, OX11 0QX, UK*

C.N. Booth, S.L. Cartwright, R. French, E.V. Korolkova, M.L. Navin, L.F. Thompson
*University of Sheffield, Sheffield S3 7RH, UK*

G.J. Barker, R. Bridgland, P.F. Harrison, A. Lovejoy, B. Morgan, J.A. Thornby
*Warwick University, UK*

T.M. Goon, R. Gould, S. Hatakeyama, T. Kutter, K. McBryde, R. Svoboda
*Louisiana State University, 202 Nicholson Hall Tower Drive Baton Rouge, Louisiana 70803, USA*

C.K. Jung, K. Kobayashi, G. Lopez, C. McGrew, A. Sarrat, L.P. Trung, L. Whitehead, C. Yanagisawa
*Department of Physics and Astronomy, The State University of New York at Stony Brook, Stony Brook, New York 11794-3800, U.S.A.*

A. Bodek, R. Bradford, H. Budd, J. Chvojka, S. Manly, K. McFarland, J. Park, W. Sakumoto, J. Steinman
*Department of Physics and Astronomy, University of Rochester, Rochester, New York 14627, USA*

H.G. Berns, R.J. Wilkes
*Dept. of Physics, University of Washington, Seattle, Washington 98195, USA*

# Contents

# Chapter 1

# Introduction

## 1.1 The Current Situation in Neutrino Oscillation Physics

Over the last 7 years neutrino physics has crossed a threshold in its basic understanding of the fundamental nature of neutrinos. Initial indications of an anomaly in the flux of neutrinos from the sun came from the pioneering experiments of Ray Davis and his collaborators [1], and from the Kamiokande experiment [2], supported by measurements of the low-energy solar neutrino fluxes by the SAGE [3] and GALLEX [4] experiments. While this was under investigation the Super-Kamiokande experiment showed a zenith-angle dependent suppression of muon neutrinos (arising from cosmic ray interactions with the atmosphere) in a manner that indicated that neutrinos have mass [5]. Recently the SNO [6] experiment has demonstrated that the solar neutrino anomaly is caused by neutrinos changing flavour, a result which was shown to be consistent with mass-induced neutrino oscillations by the recent results from the KamLAND experiment [7]. Most recently results from the K2K long-baseline neutrino oscillation experiment [8] have shown that the atmospheric neutrino anomaly observed by Super-Kamiokande appears in experiments with a controlled neutrino beam as well, strongly implicating neutrino oscillations as the cause.

Neutrino oscillations arise quite naturally in a model in which the weak eigenstates of the neutrinos $\nu_l$ are a mixture of the mass eigenstates $\nu_i$:

$$|\nu_l\rangle = \sum U_{li}|\nu_i\rangle \tag{1.1}$$

The matrix $U_{li}$ is called the Maki-Nakagawa-Sakata-Pontecorvo (MNSP) mixing matrix [9]. It is analogous to the CKM matrix which mixes the weak and strong eigenstates of the quarks, and like the CKM matrix it can be written for the case of three Dirac neutrinos as:

$$U_{ij} = \begin{pmatrix} 1 & 0 & 0 \\ 0 & c_{23} & s_{23} \\ 0 & -s_{23} & c_{23} \end{pmatrix} \begin{pmatrix} c_{13} & 0 & e^{i\delta}s_{13} \\ 0 & 1 & 0 \\ -e^{-i\delta}s_{13} & 0 & c_{13} \end{pmatrix} \begin{pmatrix} c_{12} & s_{12} & 0 \\ -s_{12} & c_{12} & 0 \\ 0 & 0 & 1 \end{pmatrix} \tag{1.2}$$

where $c_{ij} \equiv \cos\theta_{ij}$, $s_{ij} \equiv \sin\theta_{ij}$, and where the angles $\theta_{ij}$ parameterize the three possible rotations between the neutrino states. Pure $\nu_l$ states are emitted in weak interactions, but what matters for neutrino propagation are the $\nu_i$ states. If the masses of the $\nu_i$ are different they will build up a relative phase difference, and therefore when their superposition is decomposed back into the $\nu_l$ states an admixture of a "wrong" flavour (i.e., a flavour not emitted in the weak interaction that created the neutrino) appears. We call this phenomenon neutrino oscillations. For the simplest case, where only two of the mass states dominate the oscillations, the familiar formula which

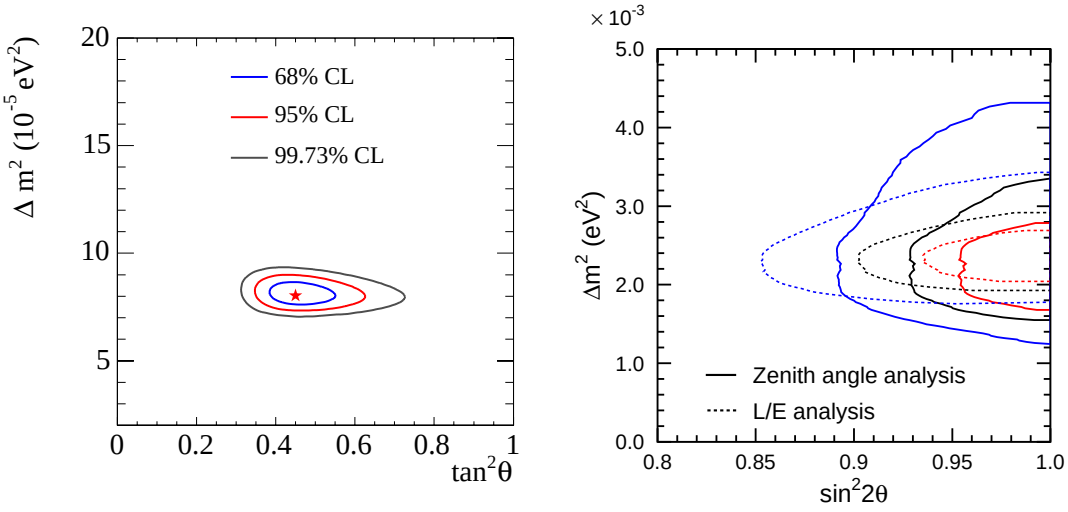


Figure 1.1: Allowed regions for 2-neutrino mixing parameters for solar+KamLAND (left figure) and from the latest Super-Kamiokande analysis (right figure). Note that the oscillations in the right figure are vacuum oscillations, and hence a plot in $\tan^2\theta$ would be symmetric about 1 (i.e., the sign of $\Delta m^2_{23}$ is not determined).

governs the appearance of one flavour, say $\nu_e$, in an initially pure beam of another flavour, say $\nu_\mu$, can be derived:

$$P(\nu_\mu \to \nu_e) = \sin^2 2\theta \ \sin^2\left(\frac{1.27\Delta m^2 L}{E}\right) \tag{1.3}$$

where $\theta$ is whichever of the angles is contributing to this particular mixing, $L$ is the distance from the source to the detector, $E$ is the energy of the neutrino, and $\Delta m^2 = m_j^2 - m_i^2$ is the difference in the squares of the masses of the two $\nu_i$ states that are mixing. The numerical constant 1.27 is valid for $L$ in kilometers, $E$ in GeV, and $\Delta m^2$ in eV$^2$. Note that these oscillations depend only on $|\Delta m^2|$, that is, they do not depend on either the absolute mass scale or ordering of the mass states. While this formula is valid in vacuum, interactions with electrons in matter can modify the oscillations (the MSW effect [10]) leading to their enhancement (or suppression). These matter effects do depend on the sign of $\Delta m^2$, and thereby provide a way to determine the ordering of the mass states (although not the absolute masses).

The current results for oscillations from solar neutrino plus KamLAND data can be fit using such matter-enhanced two-neutrino oscillations, and the resulting parameters are shown in the left part of Figure 1.1. Similarly, for the atmospheric oscillations the current best fit parameters from Super-Kamiokande are shown in the right part of Figure 1.1. Taken together these results constrain the values of two of the mixing angles from the MNSP matrix ($\theta_{12}$ and $\theta_{23}$), the value and the sign of $\Delta m^2_{12}$, and the value of $|\Delta m^2_{23}|$. It must be noted at this point that there is another claim of neutrino oscillations currently in the literature — that of the LSND collaboration [11]. They claim observation of $\overline{\nu}_\mu \to \overline{\nu}_e$ oscillations in a beam of $\overline{\nu}_\mu$ from stopped $\pi$ decay. The KARMEN experiment [12], which had similar sensitivity, has failed to confirm these results, but

has not completely excluded all of the range of parameters indicated by LSND. The $\Delta m^2$ value favored by the LSND claim is much larger ($\sim$ 1 eV$^2$) than that seen in solar or atmospheric neutrino oscillations. A new experiment (MiniBooNE [13]) at Fermilab is currently checking the LSND claim and should have results in 2005. If the LSND results are confirmed it will require a complete reevaluation of our current picture of neutrino oscillations, which cannot accommodate so many separate $\Delta m^2$ values with just three neutrinos. However, whatever new picture emerged would require new experimental constraints on other mixings even more urgently, so the case for the new experiment proposed below would be even stronger.

Ignoring LSND, what more do we need to learn about neutrino oscillations? There are still three undetermined parameters in the MNSP matrix — the angle $\theta_{13}$, the sign of $\Delta m^2_{23}$, and the value of the CP-violating phase $\delta$. These are fundamental parameters which should be predicted by a deeper theory of particle physics, and hence intrinsically interesting in themselves. It should be pointed out that measurements of the corresponding CKM parameters have been the focus of much of particle physics over the last three decades, and provided the physics justification for many facilities, including the current B factories at SLAC and KEK. The MNSP matrix elements, due to the lack of hadronic corrections, can probably be determined to greater accuracy than can the CKM matrix elements, which have been the focus of so much determined effort. Another powerful reason to pursue these studies is provided by the still unexplained matter-antimatter asymmetry of the present-day Universe. One possible source of the CP violation needed to explain this asymmetry is the neutrino sector, via the mechanism known as leptogenesis [14], and measuring the CP-violating phase $\delta$ in the MNSP matrix should give valuable insight into the CP properties of neutrinos. It is exactly this measurement of $\delta$ which provides the physics case behind the current worldwide efforts to develop a Neutrino Factory and a $\beta$-beam facility at CERN. However, as will be explained below, measuring $\delta$ is only possible if $\theta_{13}$ is sufficiently large, and hence a measurement of $\theta_{13}$ is critical to the case for a Neutrino Factory or a $\beta$-beam facility.

Our current knowledge of $\theta_{13}$ comes from three sources. Atmospheric and solar neutrino oscillation results give some information, but the most useful data for constraining the value of $\theta_{13}$ comes from the Chooz reactor $\bar{\nu}_e$ oscillation experiment [15]. This experiment measured the flux of $\bar{\nu}_e$ at a distance of 1 km from the Chooz reactor in France. Given the strong constraints on $\Delta m^2_{13}$ arising from the other oscillation results we know that a suppression of this flux should have been seen if $\theta_{13}$ were large (like the two other angles), and therefore we are able to constrain $\sin^2\theta_{13}$ to be less than $\sim 6 \times 10^{-2}$ at the 90% C.L. in the region of $\Delta m^2_{13}$ indicated by Super-Kamiokande (see Figure 1.2).

## 1.2 Future Progress in Neutrino Oscillation Physics

In addition to the MiniBooNE experiment mentioned above, the next few years should see the beginning of data taking by two long baseline oscillation programs — the NuMI neutrino beam from Fermilab [16], which is aimed at the MINOS detector 735 kilometers away in the Soudan mine; and the CNGS neutrino beam from CERN, which is aimed at the Laboratori Nazionali del Gran Sasso (LNGS) in Italy, where two experiments (OPERA [17] and ICARUS [18]) are currently under construction. The MINOS detector will make sensitive measurements of muon neutrino disappearance, and thereby make a measurement of $\Delta m^2_{23}$ accurate to about 10%. The CNGS experiments are using a higher-energy neutrino beam, and are aimed at making a conclusive demonstration of the mechanism for atmospheric neutrino disappearance by actually observing the appearance of $\nu_\tau$ from $\nu_\mu \rightarrow \nu_\tau$ oscillations.

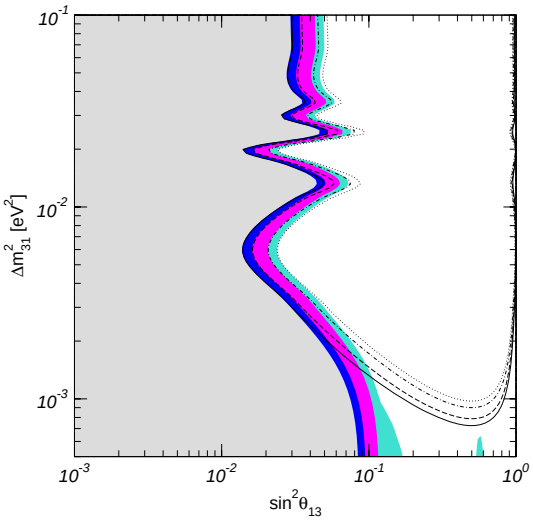


Figure 1.2: Allowed region for $\theta_{13}$ from Chooz alone (lines) and also including data from solar neutrino experiments and Kamland (colored regions) at 90%, 95%, 99%, and $3\sigma$. From Maltoni *et al*, hep-ph/0309130.

The next goal would then be to improve our sensitivity to $\theta_{13}$ in the hope of a positive observation. Our current knowledge of neutrino oscillations tells us that all neutrino oscillations observable on the Earth will be dominated by the two oscillations measured with solar and atmospheric neutrinos, and that any $\theta_{13}$ experiment must therefore look to small corrections to these oscillations caused by the sub-dominant effects which are all that $\theta_{13}$ will give rise to (given that we already know that $\theta_{13}$ is small). To understand these sub-dominant effects we need to go beyond the 2-neutrino formula shown above and look at the oscillation formula taking into account the full 3-neutrino mixing matrix:

$$\begin{aligned}
P(\nu_\mu \to \nu_e) = \quad & 4C_{13}^2 S_{13}^2 S_{23}^2 \sin^2\ \Phi_{31} \times \left(1 + \tfrac{2a}{\Delta m^2_{31}}(1 - 2S_{13}^2)\right) \\
+ \quad & 8C_{13}^2 S_{12} S_{13} S_{23} (C_{12} C_{23} \cos\ \delta - S_{12} S_{13} S_{23}) \cos\ \Phi_{32} \cdot \sin\ \Phi_{31} \cdot \sin\ \Phi_{21} \\
- \quad & 8C_{13}^2 C_{12} C_{23} S_{12} S_{13} S_{23} \sin\ \delta \cdot \sin\ \Phi_{32} \cdot \sin\ \Phi_{31} \cdot \sin\ \Phi_{21} \\
+ \quad & 4S_{12}^2 C_{13}^2 \left(C_{12}^2 C_{23}^2 + S_{12}^2 S_{23}^2 S_{13}^2 - 2C_{12} C_{23} S_{12} S_{23} S_{13} \cos\ \delta\right) \sin^2\ \Phi_{21} \\
- \quad & 8C_{13}^2 S_{13}^2 S_{23}^2 \left(1 - 2S_{13}^2\right) \tfrac{aL}{4E_\nu} \cos\ \Phi_{32} \cdot \sin\ \Phi_{31}. \qquad (1.4)
\end{aligned}$$

Here, $\Phi_{ij} \equiv \Delta m^2_{ij} L/4E$. This expression is complex, and even this is only an approximation (the matter effects come in through the terms multiplied by the parameter $a$, which depends upon the electron density, fundamental constants and mass differences, and in this formula the matter effects are calculated in the approximation of constant density). Analyzing the predictions of this formula is currently rather difficult, as it contains three unknown quantities ($\delta$, $\theta_{13}$, and the sign of $\Delta m^2_{23}$, which comes into the matter effect parameter $a$), as well as all the other oscillation constants, which of course have uncertainties in their measured values. However given the already known limits on the parameters it is possible to produce an approximate form of this formula that makes the point of the T2K experiment a little easier to explain:

$$P(\nu_\mu \to \nu_e) \quad \approx \quad \sin^2 2\theta_{13} \sin^2 2\theta_{23} \sin^2 \Delta$$

$$
\begin{aligned}
&\pm \quad \alpha \sin 2\theta_{13} \sin\delta \cos\theta_{13} \sin 2\theta_{12} \sin 2\theta_{23} \sin^3\Delta \\
&- \quad \alpha \sin 2\theta_{13} \cos\delta \cos\theta_{13} \sin 2\theta_{12} \sin 2\theta_{23} \cos\Delta \sin 2\Delta \\
&+ \quad \alpha^2 \cos^2\theta_{23} \sin^2 2\theta_{12} \sin^2\Delta
\end{aligned}
$$

where $\alpha \equiv \Delta m^2_{21}/\Delta m^2_{31}$ and $\Delta = \Delta m^2_{31} L/4E$. The existing limits from joint fits to the solar, KamLAND, and Super-K atmospheric data show that $\alpha \approx 3 \times 10^{-2}$. Chooz + solar neutrino data shows that $\sin^2 2\theta_{13} <\sim 0.2$, and of course the value of $\delta$ is completely unknown. For the values which will be used in the T2K experiment all the other terms in this expansion are $\sim 1$. It should also be noted that this expansion sets the matter terms to zero, however for T2K that is an excellent approximation. Looking at the approximate formula, the only term that doesn't depend on $\theta_{13}$ is the last one (which is in fact the approximate form for the oscillations that KamLAND sees), but this depends on $\alpha^2$ and is therefore unobservable in T2K. For values of $\sin 2\theta_{13}$ within an order of magnitude of its current upper limit, the first term dominates, which describes a relatively simple oscillatory appearance of $\nu_e$ in $\nu_\mu$ beam.

That then suggests the proper target for future experiments. Firstly, we need to improve our sensitivity to $\theta_{13}$ by at least an order of magnitude, and hopefully more. The MINOS and the CNGS experiments should produce some improvement in our sensitivity, but certainly not an order of magnitude. At the same time measuring $\theta_{23}$ and $\Delta m^2_{23}$ with greater precision is interesting in its own right (in particular, the deviation of $\theta_{23}$ from $\pi/4$ is a matter of great interest to model builders) as well as being a necessary for extracting the values of the so-far unmeasured parameters from oscillation measurements. Experiments at longer baselines will also be needed to look for matter effects in order to determine the sign of $\Delta m^2_{23}$, and more precise measurements of these, then, are the targets of the proposed "superbeam"experiments, of which T2K is the first approved example. We will then need to do further experiments (using either advanced superbeams, beta beams, or a neutrino factory) to look for $\delta$ by taking advantage of the $\pm$ in the above formula, which indicates that the sign of that term switches for neutrinos and anti-neutrinos.

## 1.3 The T2K Long Baseline Experiment

The first phase of the T2K experiment is therefore aimed at two main goals — the more accurate determination of the "atmospheric" parameters $\theta_{23}$ and $\Delta m^2_{23}$, and a measurement of $\theta_{13}$ with more than an order of magnitude sensitivity than any previous experiment. The project is based on adding a beamline (described in more detail below) to redirect the proton beam from the 50 GeV synchrotron currently under construction at the new JPARC facility (Figure 1.3) in Tokai, Japan [19] to produce an intense neutrino beam. The high power of the JPARC proton beam, 0.75 MW in Phase I, rising to 4 MW in Phase II, expected in about 2015, will produce the most intense neutrino beam ever built. A set of detectors are located 280 m from the pion production target to characterize the neutrino beam. This beam then propagates underground for 295 km to the Super Kamiokande detector [20] in western Japan, which is well suited for distinguishing $\nu_e$ and $\nu_\mu$ in the neutrino beam by looking at Cherenkov radiation from $\mu$'s and e's produced by charged-current interactions in its 50 kton water target. A key element of the design of the T2K facility (see Figure 1.4) is that the neutrino beam is directed so that the beam axis actually misses Super-Kamiokande. This, rather surprisingly, actually results in a considerable improvement in the quality of the beam for the $\nu_e$ appearance experiment. This arises from the kinematics of $\pi$ decay, which result in an enhancement in the neutrino flux produced over a very narrow range of energies which depend on the exact off-axis angle (see Figure 1.5). By selecting the correct

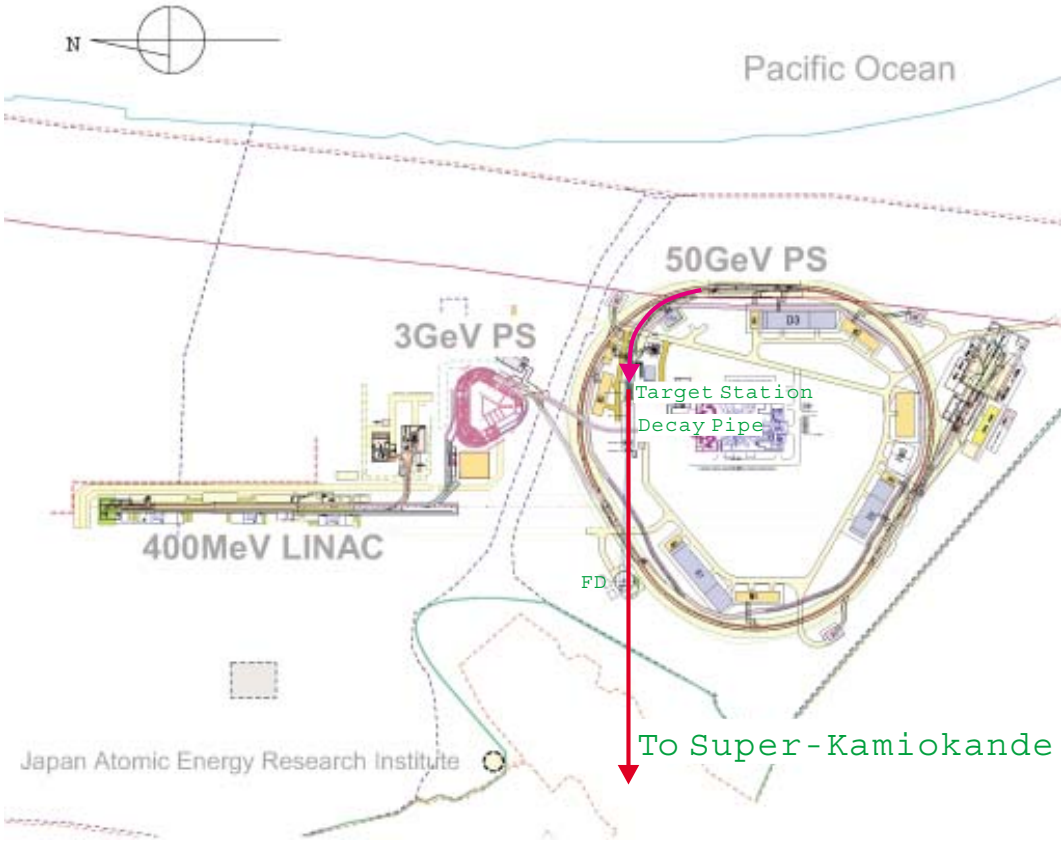


Figure 1.3: Overview of the JPARC facility.

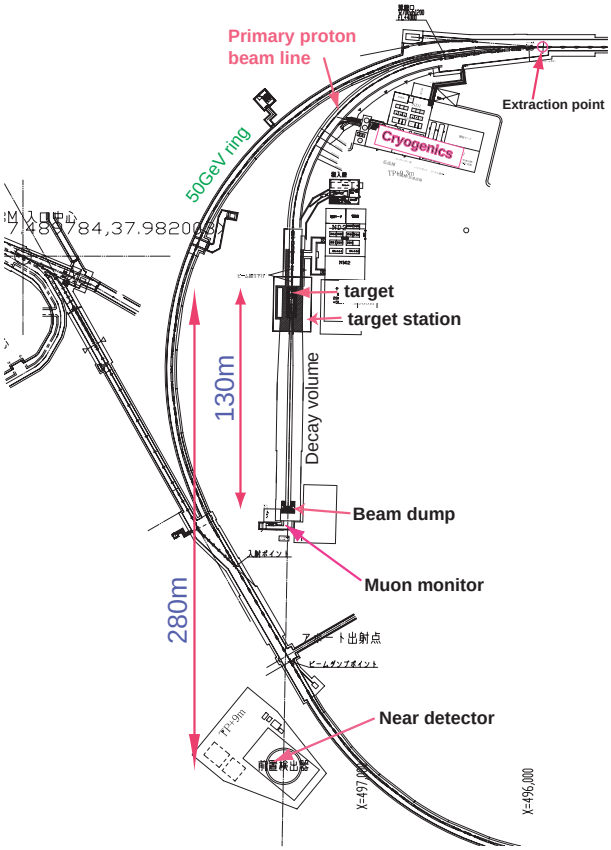


Figure 1.4: T2K beamline.

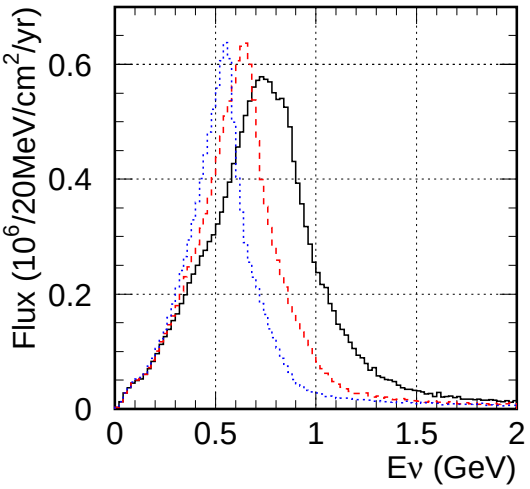


Figure 1.5: Energy spectra from off-axis beams: black-solid line (2 degree), red-dashed line (2.5 degree), and blue-dotted line (3 degree). As the off-axis angle increases, the energy peak narrows and moves lower in energy.

angle, this narrow peak can be near on the oscillation maximum at the far detector. This has three major advantages over a conventional on-axis beam. Firstly, the off-axis neutrino flux at the desired energy (the oscillation maximum) is actually higher than on-axis. Secondly, there are fewer high-energy neutrinos, which do not contribute to the appearance signal but do contribute to its backgrounds, in particular through the neutral-current production of $\pi^0$'s (which decay to produce two $\gamma$'s, which can sometimes be mistaken for the single electron characteristic of a charged-current interaction with a $\nu_e$). Thirdly, the background due to the intrinsic contamination of the beam by $\nu_e$ is actually less at the off-axis position due to the different kinematics of the decays that lead to $\nu_e$.

The very kinematics that give a useful selection in energy, however, mean that the characteristics of the beam change rapidly with angle. Detailed measurement of the beam properties will therefore be required to minimize the systematic uncertainties in any neutrino oscillation measurement. These detailed measurements will be made with two complexes of detectors downstream of the target, a set of near detectors at 280 m, and eventually a set of intermediate detectors at 2 km. The purpose of this CDR is to describe in some detail the 280 m detector complex and the physics measurements to be made with its detectors.

## 1.4 The T2K neutrino beam

The main synchrotron is designed to accelerate protons up to 50 GeV, however the initial proton energy of is limited to 40 GeV. Therefore, the beam energy is set to 40 GeV in the following flux calculations and event rate estimations. The design intensity of the proton beam is $3.3 \times 10^{14}$ protons/pulse at a repetition rate of $\sim$0.3Hz. The fast extracted beam width is 5.6 $\mu$sec and there are 8 (or possibly 15) bunches in a spill. The width of each bunch is 58 ns.

The extracted proton beam hits a target to generate pions. This production target will be a graphite cylincer 30 mm in diameter and 900 mm in length. Three electro-magnetic horns will be used to focus the charged pions generated in the target to the forward direction. The target will be put inside of the inner conductor of the first horn to collect and focus the pions as much as possible. These horns are driven by a pulsed current of 320 kA synchronized with the beam. The focused pions decay into neutrinos in a 130m decay tunnel which follows the horns. The decay tunnel is filled with 1 atm Helium gas to reduce pion absorption and reduce tritium production.

The neutrino beamline for T2K at J-PARC adopts an off axis beam (OAB) configuration [21] as described in Section 1.3. The T2K off axis angle can be changed from $2.0^\circ$ to $3.0^\circ$. This corresponds to the mean neutrino energies from 0.5 to 0.9 GeV. In the following discussions, we fix the off-axis angle to $2.5^\circ$.

A full neutrino beam simulation using Geant3 package has been performed to obtain the neutrino flux at six potential locations for near detectors as shown in Figure 1.6. ND2 is a traditional on axis location, and ND5 is the proposed location for the off-axis near detector. The ND3 and ND4 areas are used to study the on-axis neutrino monitor in the following sections. The neutrino energy spectra at the on-axis (ND2) and the off-axis (ND5) detectors are shown in Figure 1.7. The predicted $\nu_e$ spectrum is also shown in Figure 1.7. The fraction of $\nu_e$ around the peak is of the order 0.5% for both ND2 and ND5 locations.

The expected event rates at each of the near detectors are calculated with the neutrino interaction Monte Carlo NEUT and the results are summarized in Table 1.1.

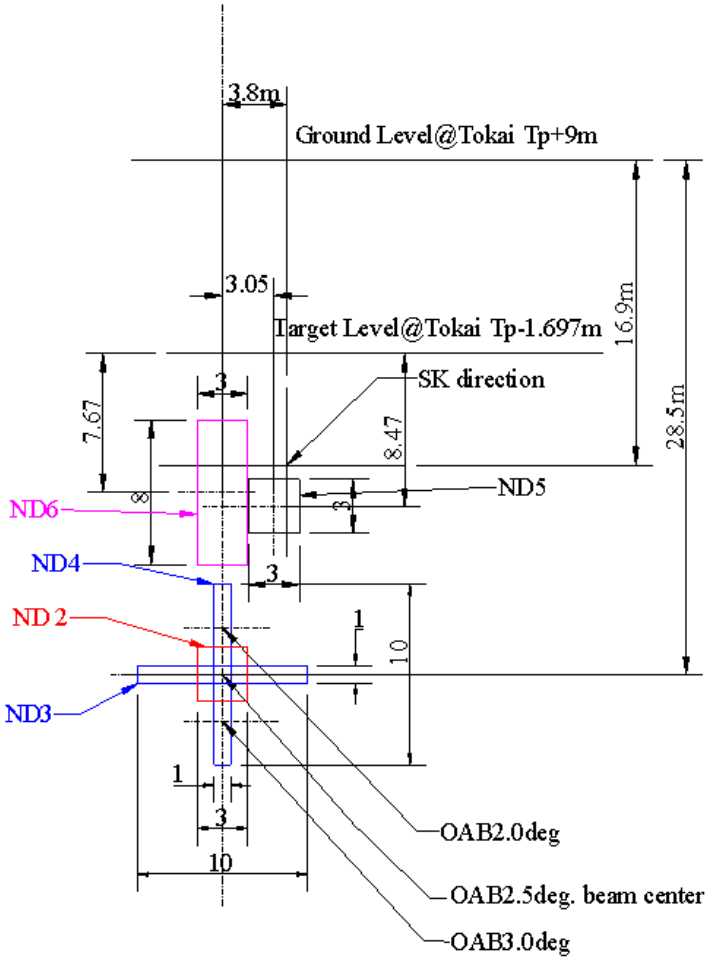


Figure 1.6: Locations of the sampling areas for neutrino simulations. The plane represents the center of the ND280 experimental hall, the squares are the different areas where neutrino fluxes have been calculated.

| detector position | $\nu_\mu$ $(events/ton/10^{21} POT)$ | $\nu_e$ $(events/ton/10^{21} POT)$ |
|---|---|---|
| ND2 | $1.08 \times 10^6$ | $9.32 \times 10^3$ |
| ND3 | $8.83 \times 10^5$ | $8.38 \times 10^3$ |
| ND4 | $9.00 \times 10^5$ | $8.44 \times 10^3$ |
| ND5 | $1.70 \times 10^5$ | $3.34 \times 10^3$ |
| ND6 | $1.82 \times 10^5$ | $3.31 \times 10^3$ |

Table 1.1: The expected number of interactions in each detector. Each value corresponds to one year of operation($10^{21}$ protons on target). The numbers are computed using the T2K neutrino beam simulation and the neutrino interaction Monte Carlo (NEUT).

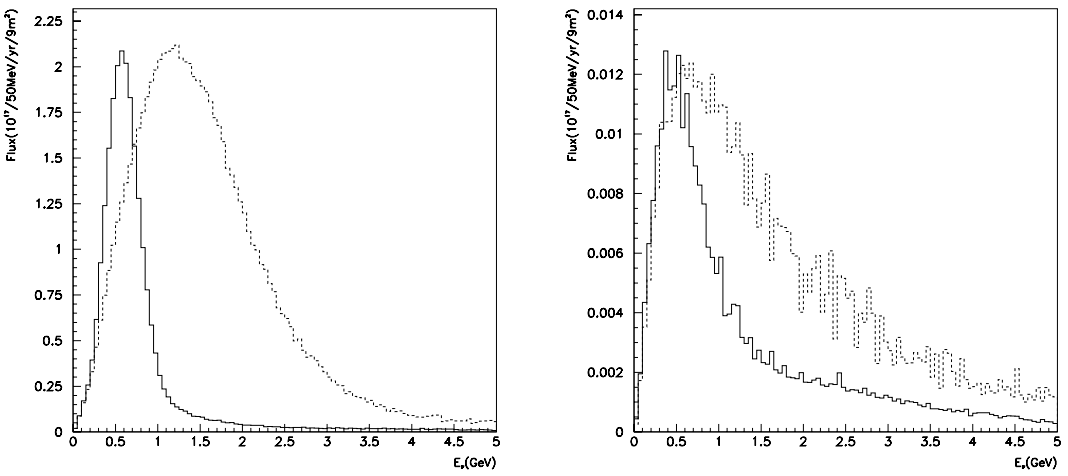


Figure 1.7: (Left) Spectra of muon neutrinos at the on-axis (ND2) and the off-axis (ND5) detectors. (Right) Spectra of electron neutrinos at the on-axis (ND2) and the off-axis (ND5) detectors. The solid histograms show the flux at ND5 and the dashed histograms show the flux at ND2.

## 1.5 T2K physics goals

The main physics goals of the T2K experiment are:

- A precision measurement of the neutrino oscillation parameters, $(\sin^2 2\theta_{23}, \Delta m^2_{23})$, by $\nu_\mu \to \nu_x$ disappearance.
- The determination of $\sin^2 2\theta_{13}$ by the measurement of the $\nu_\mu \to \nu_e$ appearance signal.
- Confirmation of $\nu_\mu \to \nu_\tau$ oscillation by the measurement of neutral current events.

### 1.5.1 $\nu_\mu$ disappearance

The neutrino oscillation parameters, $(\sin^2 2\theta_{23}, \Delta m^2)$, will be determined by measuring the survival probability of $\nu_\mu$ after traveling 295 km. Neutrino events in SK are selected as fully-contained events with visible energy ($E_{vis.}$) greater than 30 MeV in the fiducial volume of $22.5$ kton. The events are further selected by requiring the presence of a single muon-like ring. The expected number of events without oscillation for an off-axis angle of $2.5^\circ$ and $5 \times 10^{21}$ protons on target (POT) are summarized in Table 1.2. The numbers of events after oscillation as a function of $\Delta m^2_{23}$ are shown in Table 1.3 for the values of oscillation parameters $\sin^2 2\theta_{23} = 1.0$ and $\sin^2 2\theta_{13} = 0.0$.

In order to measure the oscillation parameters, the neutrino energy distribution of the fully-contained single ring $\mu$-like events is reconstructed using an extended-maximum likelihood method. The reconstructed neutrino energy distribution and the ratio of the prediction with the best-fit oscillation parameters (from existing experiments) to the prediction without oscillations is shown in Figure 1.8. The expected statistical uncertainty on the measurements is 0.009 for $\sin^2 2\theta_{23}$ and $5 \times 10^{-5}\mathrm{eV}^2$ for $\Delta m^2_{23}$, and is shown as a function of the true $\Delta m^2_{23}$ in Figure 1.9.

| | CC-QE | CC-nonQE | NC | All $\nu_\mu$ |
|---|---|---|---|---|
| Generated in FV | 4,114 | 3,737 | 3,149 | 11,000 |
| (1) FCFV | 3,885 | 3,011 | 1,369 | 8,265 |
| (2) $E_{vis.} \geq 30$ MeV | 3,788 | 2,820 | 945 | 7,553 |
| (3) Single ring $\mu$-like | 3,620 | 1,089 | 96 | 4,805 |

Table 1.2: The expected number of neutrino events for $5 \times 10^{21}$ POT for $\nu_\mu$ disappearance analysis without oscillation. CC-QE refers to charged current quasi-elastic events and CC-nonQE to other charged current events, while NC refers to neutral current events.

| $\Delta m^2$ (eV$^2$) | CC-QE | CC-nonQE | NC | All $\nu_\mu$ |
|---|---|---|---|---|
| No oscillation | 3,620 | 1,089 | 96 | 4,805 |
| $2.0 \times 10^{-3}$ | 933 | 607 | 96 | 1,636 |
| $2.3 \times 10^{-3}$ | 723 | 525 | 96 | 1,344 |
| $2.7 \times 10^{-3}$ | 681 | 446 | 96 | 1,223 |
| $3.0 \times 10^{-3}$ | 800 | 414 | 96 | 1,310 |

Table 1.3: The expected number of neutrino events for $5 \times 10^{21}$ POT for $\nu_\mu$ disappearance analysis with neutrino oscillation for different values of $\Delta m^2_{23}$ with $\sin^2 2\theta_{23} = 1.0$ and $\sin^2 2\theta_{13} = 0.0$.

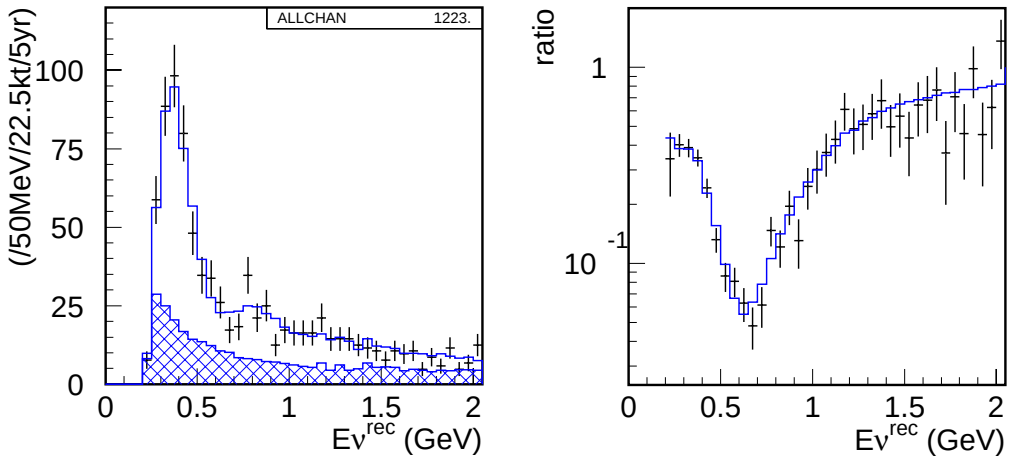


Figure 1.8: (Left) The reconstructed neutrino energy distribution with predicted for the best-fit oscillation parameters $(\sin^2 2\theta_{23}, \Delta m^2) = (1.0, 2.7 \times 10^{-3}\,\mathrm{eV}^2)$. The hatched area shows the non-QE component. (Right) The ratio of the reconstructed neutrino energy distribution with oscillation to one without oscillation.

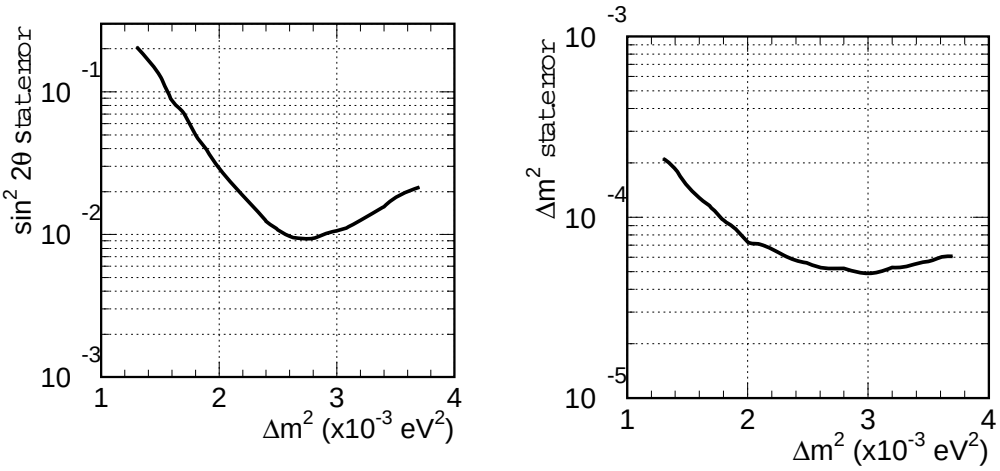


Figure 1.9: The statistical uncertainty of the oscillation parameters as a function of true $\Delta m^2_{23}$. The value of $\sin^2 2\theta_{23}$ is assumed to be one.

We have studied the effects of the following systematic uncertainties. We take two reference values to be compared with the statistical error.

1. The uncertainty in the predicted number of the fully-contained single ring $\mu$-like events. We consider 10 % and 5 % uncertainties.

2. The uncertainty in the energy scale. We consider 4 % and 2 % uncertainties.

3. The uncertainty in the non-QE/QE ratio. We consider 20 % and 5 % uncertainties.

Figure 1.10 shows the effect of the systematic errors. In order to keep the systematic uncertainties below the statistical error, the uncertainties should be less than about 5 % for the predicted number of events, 2 % for the energy scale, and 5-10 % for the non-QE/QE ratio. The near neutrino detector must be designed to provide information for the above requirements.

### 1.5.2 $\nu_e$ appearance

The $\nu_e$ selection cuts are based on the SK-1 atmospheric neutrino analysis. Events are required to be fully contained withint the 22.5kt fiducial volume, have visible energy ($E_{vis}$) greater than 100MeV, a single electron like (e-like) ring, and no decay electrons. The electron identification eliminates the most muon background events, and the decay electron cut further reduces events from inelastic charged current (CC) processes associated with $\pi^0$ production. The dominant source of background events (see Table 1.4) at this stage is single $\pi^0$ production in neutral current (NC) interactions. The backgrounds can be further reduced by requiring the reconstructed neutrino energy to be around the oscillation maximum: 0.35 GeV $\leq E_\nu^{rec.} \leq$ 0.85GeV.

The remaining background from $\pi^0$ is further reduced with specific "e/$\pi^0$ separation" cuts. The $\pi^0$ background has a steep forward peak towards the neutrino direction due to coherent $\pi^0$ production. Thus events in the extreme forward direction ($\cos\theta_{\nu_e} \geq 0.9$) are rejected. Then events with only one high-energy gamma detected in the asymmetric decay of the $\pi^0$ are the dominant

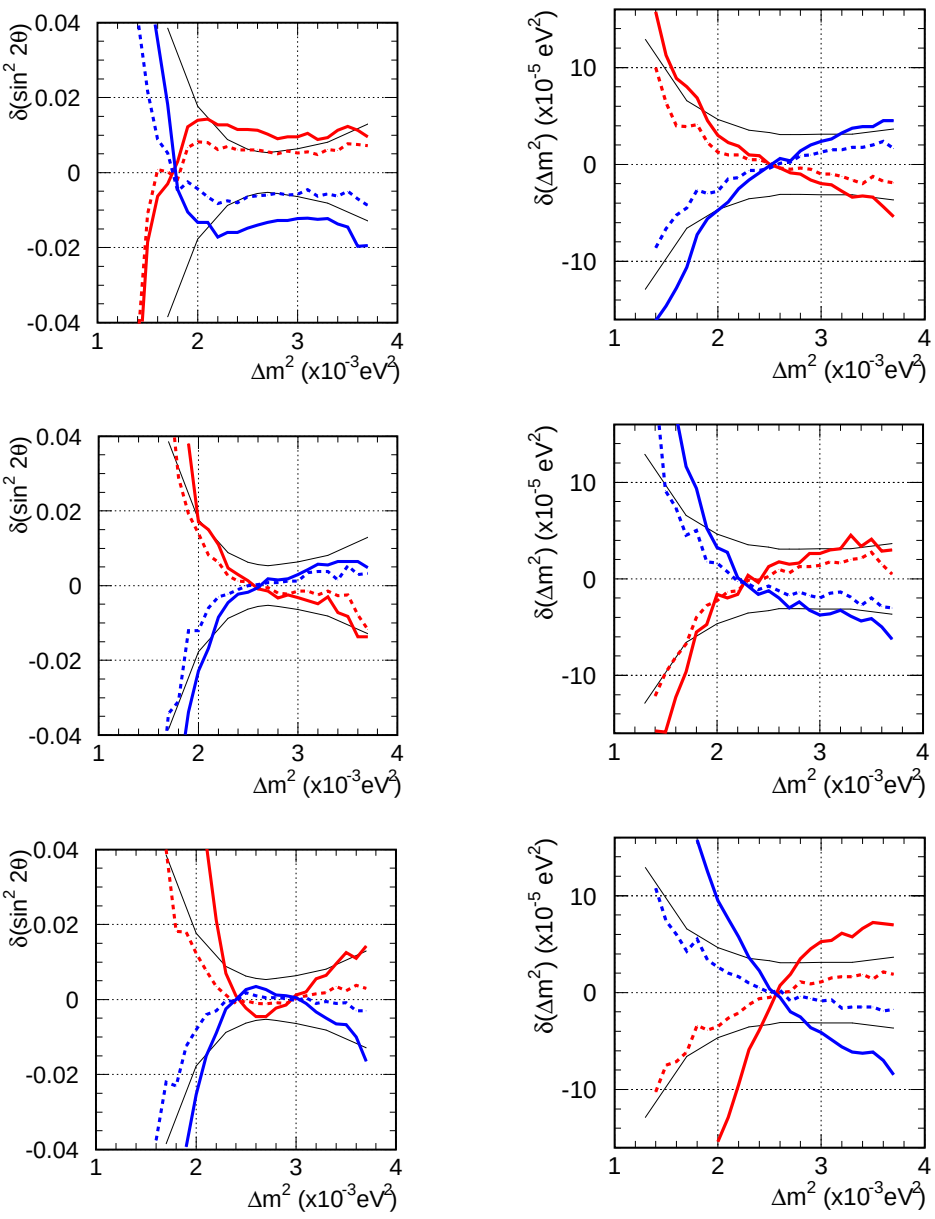


Figure 1.10: The bias of the oscillation parameter estimates as a function of true $\Delta m^2$ as a result of systematic errors. The value of $\sin^2 2\theta$ is assumed to be one. A systematic error in the total number of events by 10 % (solid) and 5 % (dashed) is included in the top two figures, an error in the energy scale by 4 % (solid) and 2 % (dashed) is included in the middle figures, and an error in the non-QE/QE ratio by 20 % (solid) and 5 % (dashed) are indicated in the bottom figures. The error for the positive direction is shown by the blue line, and the negative direction is shown by the red.

| | $\nu_\mu$CC BG | $\nu_\mu$NC BG | beam $\nu_e$ BG | $\nu_e$CC signal |
|---|---|---|---|---|
| Fully-contained, $E_{vis}$ $\geq$100MeV | 2215 | 847 | 184 | 243 |
| 1 ring e-like, no decay-e | 12 | 156 | 71 | 187 |
| 0.35$\leq$ $E_\nu^{rec.}$ $\leq$0.85GeV | 1.8 | 47 | 21 | 146 |
| e/$\pi^0$ separations | 0.7 | 9 | 13 | 103 |

Table 1.4: The number of events selected by the $\nu_e$ appearance analysis, as predicted by NEUT Monte Carlo for $5 \times 10^{21}$ POT exposure. For the calculation of oscillated $\nu_e$, $\Delta m^2 = 2.5 \times 10^{-3}\mathrm{eV}^2$ and $\sin^2 2\theta_{13} = 0.1$ are assumed.

background. In order to find the hidden lower-energy gamma ring, the photomultiplier hit pattern, including scattered light, is fit under the hypothesis of two gamma rings. The energy and direction of each gamma ring are reconstructed, and the invariant mass of two rings is calculated. The $\pi^0$ background is further suppressed by rejecting events with the mass at around the $\pi^0$ mass ($m_{2\gamma}^{rec.} \geq 100\mathrm{MeV/c}^2$). These further "e/$\pi^0$' separation' cuts significantly reduce the $\pi^0$ background until it is comparable to the predicted background from intrinsic $\nu_e$ in the beam.

Table 1.4 summarizes the number of events after the event selections for $5\times10^{21}$ POT exposure at $\Delta m^2 = 2.5 \times 10^{-3}\mathrm{eV}^2$ and $\sin^2 2\theta_{13} = 0.1$.

As a sensitivity, we calculate the 90% upper limit for an experiment that observes the expected background rate. Figure 1.11 shows the 90% C.L. $\nu_e$ sensitivity for $5\times10^{21}$ POT exposure and for $\sin^2 2\theta_{23} = 1$ and $\delta = 0, \pi/2, -\pi/2, \pi$, assuming a 10% systematic uncertainty in the background subtraction. The sensitivity is $\sin^2 2\theta_{13} = 0.008$ at 90% C.L. for $\Delta m^2 \sim 2.5 \times 10^{-3}\mathrm{eV}^2$. This represents an order of magnitude improvement over the CHOOZ limit.

Figure 1.11 shows the 90% C.L. and $3\sigma$ $\nu_e$ sensitivities as a function of the exposure time for $\Delta m^2 = 2.5 \times 10^{-3}\mathrm{eV}^2$ for systematic uncertainties in the background subtraction of 5%, 10%, and 20%. This graph suggests the target for the near detectors of a 10% uncertainty in the background in the first phase ($5 \times 10^{21}$ POT = SK$\times$5years ).

### 1.5.3 $\nu_\tau$ versus $\nu_{sterile}$ analysis

The analysis of $\nu_\tau$ appearance has been performed by the Super-Kamiokande collaboration [22]. This measurement disfavors a pure $\nu_\mu \rightarrow \nu_{sterile}$ solution to the atmospheric neutrino anomaly. The search for $\nu_\mu \rightarrow \nu_{sterile}$ with small mixing angle is still an interesting topic that can be addressed by the T2K experiment. The analysis method is based on the neutral current measurement in the SK detector, a clear signature of which is single $\pi^0$ production. The analysis is performed in a similar way to the previous ones:

- 22.5 KTon fiducial volume cut is applied.
- The visible energy is selected between 100 MeV and 1500 MeV.
- Events are selected for 2 e-like rings.
- Events are selected with no decay electrons to further suppress the CC background.

The event suppression by the cuts is shown in Table 1.5. The purity of the final NC sample is 83%, with 255 total expected events for an exposure of $5 \times 10^{21}$ POT.

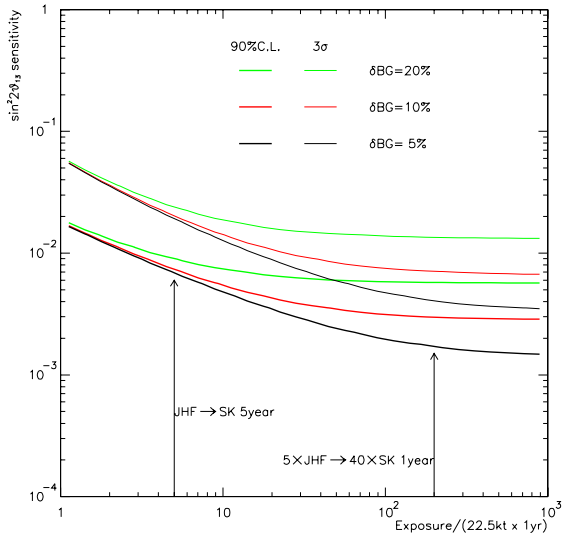


Figure 1.11: (Left) The 90% C.L. sensitivity to $\sin^2 2\theta_{13}$ for an exposure of $5 \times 10^{21}$ POT with the assumption of maximum mixing, $\sin^2 2\theta_{23} = 1.0$, and the CP violation phase $\delta = 0, \pi/2, -\pi/2, \pi$. The 90% excluded region of CHOOZ is overlaid for comparison with $\sin^2 2\theta_{23} = 1.0$. (Right) The expected 90% C.L. and $3\sigma$ sensitivities of $\sin^2 2\theta_{13}$ as a function of exposure time (5 years $\equiv 5 \times 10^{21}$ POT) for three different uncertainties in background subtraction. We assume $\Delta m^2 = 2.5 \times 10^{-3}\mathrm{eV}^2$ and $\delta = 0$.

| | $\nu_\mu$ CC | $\nu_\mu + \nu_\tau$ NC $\nu_\mu -> \nu_\tau$ | $\nu_\mu$ NC $\nu_\mu -> \nu_s$ | $\nu_e$ |
|---|---|---|---|---|
| Generated in Fiducial Volume | 3,173 | 3,239 | 1,165 | 236 |
| (1) 100 MeV $\leq E_{vis.} \leq$ 1500 MeV | 184 | 724 | 429 | 109 |
| (2) Two e-like rings | 31 | 281 | 125 | 19 |
| (3) No decay electron | 9 | 255 | 104 | 14 |

Table 1.5: The expected number of neutrino events in $5 \times 10^{21}$ POT for $\nu_\tau$ appearance analysis without oscillation. The third and fourth columns show the comparison for the two cases where the oscillation is purely to $\nu_\tau$ or to $\nu_s$. The numbers are computed assuming $\sin^2 2\theta_{23} = 1.0$ and $\Delta m^2 = 2.7 \times 10^{-3}\mathrm{eV}^2$.

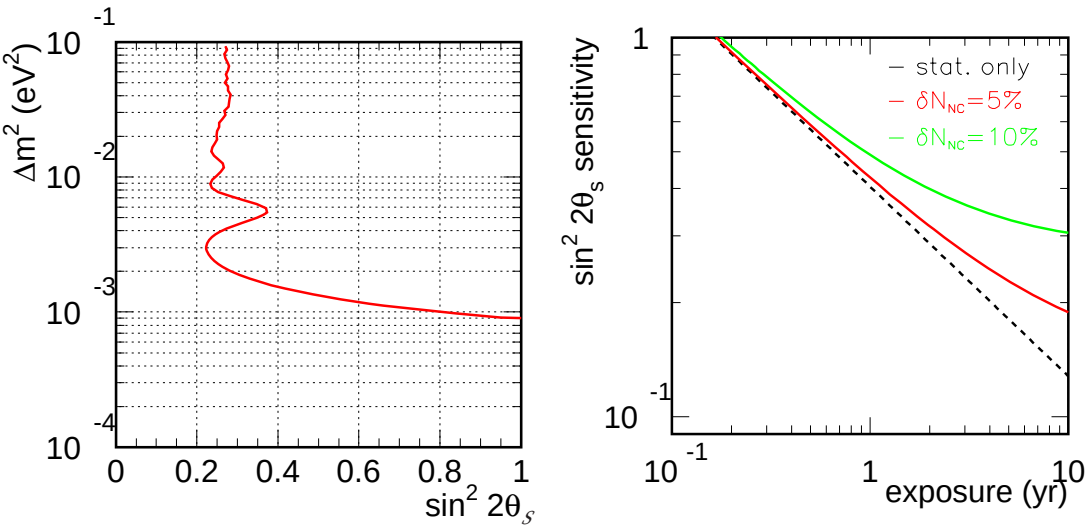


Figure 1.12: (Left) Sensitivity to the $\nu_s$ fraction in the $\sin^2 2\theta_s$ vs. $\Delta m^2$ plane with $5 \times 10^{21}$ POT. (Right) The sensitivity as a function of exposure with different uncertainties in the background estimation.

The sensitivity to the fraction of $\nu_s$ in $\nu_\mu \rightarrow \nu_\tau$ oscillation is shown in Figure 1.12 as a function of $\Delta m^2$ and $\sin^2 2\theta_s$. The best limit, $\sin^2 2\theta_s \leq 0.2$, is obtained for $\Delta m^2 \approx 3 \times 10^{-3} eV^2$. The effect of systematic uncertainties is shown in Figure 1.12, where the sensitivity to $\sin^2 2\theta_s$ is plotted as a function of the exposure time for two values of systematic error on the NC prediction: 5% and 10%. A 10% error already dominates the measurement after the first year ($10^{21}$ POT), and a value of the order of 5% improves the sensitivity by less than a factor of 2 at $5 \times 10^{21}$ POT. The main systematic error for this analysis is knowledge of NC $\pi^0$ production, similar to the $\nu_e$ appearance analysis.

# Chapter 2

# Physics Motivation and Requirements of ND280

To achieve the physics goals set out in the previous chapter, it is essential to have precise measurements of the neutrino beam properties near the target, and measurements of neutrino interaction cross sections and kinematics. For the $\nu_\mu$ disappearance study, it is important to measure the flux of muon neutrinos and their spectrum. In addition, cross sections need to be measured for muon neutrino interactions for which the far detector will misinterpret and assign the wrong neutrino energy. For the $\nu_e$ appearance study, the flux and spectrum of electron neutrinos must be known, as well as the cross sections for interactions that the far detector will misinterpret as coming from $\nu_e$. The extrapolation of the flux and the spectrum measurements near the target to the far detector will be complicated by the extended nature of the neutrino source. To make these measurements to the required precision necessitates a highly segmented large volume detector, capable of charged and neutral particle energy measurements and particle identification.

It is also important to monitor the neutrino beam direction, flux, and profile on a frequent basis, to ensure that the neutrino beam properties are stable. This requires dedicated muon monitors downstream of the beam dump and neutrino monitors on the beam axis.

This chapter introduces the detectors proposed to make these measurements, and the general oscillation analysis strategies that will use these measurements. Subsequent chapters describe the detectors in detail.

## 2.1 Overview of the ND280 Near Detector

The near detector complex at 280 m from the target (ND280) contains a fine-resolution magnetized detector designed to measure the neutrino beam's energy spectrum, flux, flavor content, and interaction cross-sections before the neutrino beam has a chance to oscillate. This detector sits off-axis in the neutrino beam along a line between the average pion decay point in the decay volume and the Super-Kamiokande detector, at a distance of 280 m from the hadron production target.

The ND280 detector consists of the following elements, illustrated in Figure 2.1:

- Magnet: ND280 uses the UA1 magnet operated with a magnetic field of 0.2 T to measure the momenta of penetrating charged particles produced by neutrino interactions in the near detector. The inner dimensions of the magnet are 3.5 m $\times$ 3.6 m $\times$ 7.0 m. The magnet is described in more detail in Section 3.4

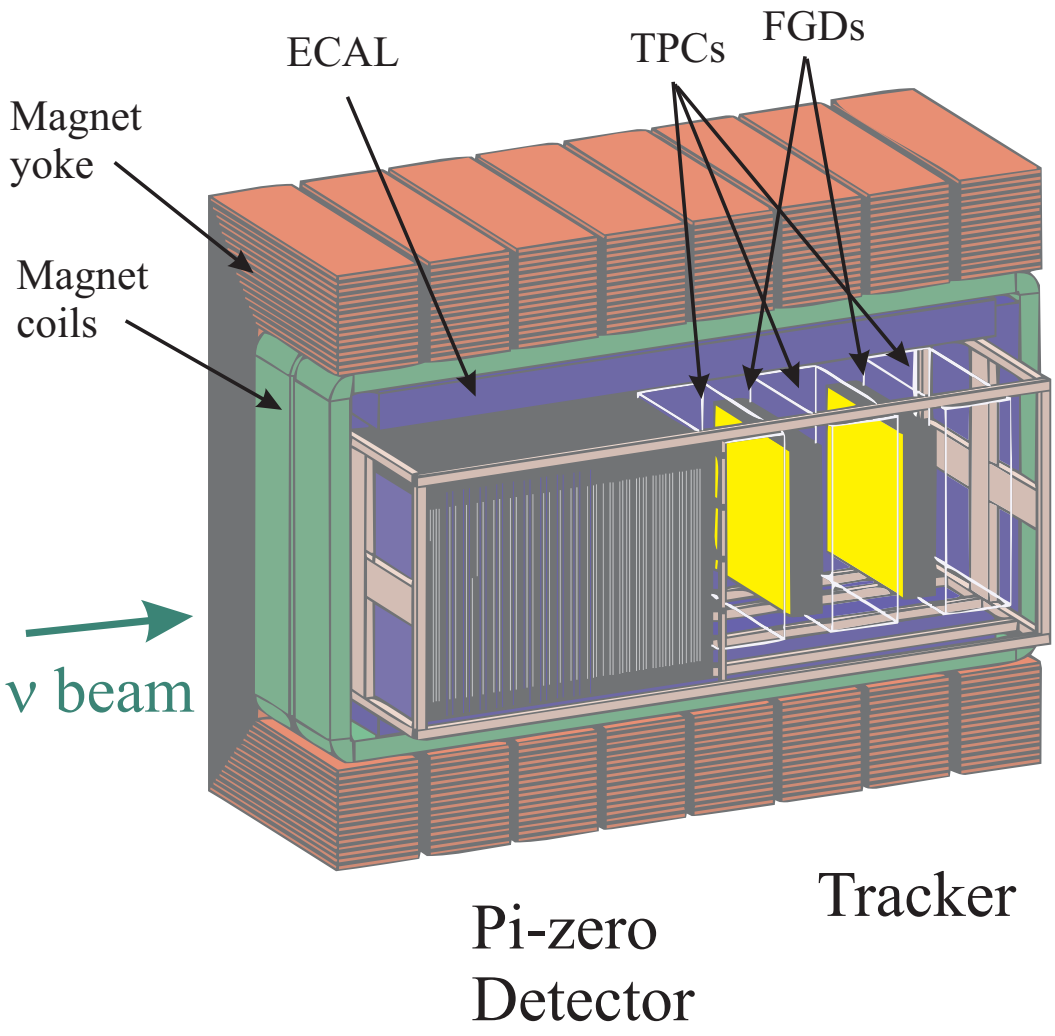


Figure 2.1: Cutaway view of the T2K 280 m near detector. The neutrino beam enters from the left.

- Pi-Zero Detector (P0D): The P0D detector sits at the upstream end of ND280, and is optimized for measuring the rate of neutral current $\pi^0$ production. The P0D consists of tracking planes composed of scintillating bars alternating with lead foil. Inactive layers of passive water in sections of the P0D provide a water target for measuring interactions on oxygen. The P0D is approximately cubical, and is covered on all 6 sides by the electromagnetic calorimeter. The P0D is described in Chapter 6.

- Tracker: Downstream of the P0D is a tracking detector optimized for measuring the momenta of charged particles, particularly muons and pions produced by CC interactions, and for measuring the $\nu_e$ background in the beam. The tracker consists of two detector technologies, fine grained target modules and time projection chambers.

    1. Time Projection Chambers (TPCs): Three time projection chambers will measure the 3-momenta of muons produced by charged current interactions in the detector, and will provide the most accurate measurement of the neutrino energy spectrum. The 3D tracking and dE/dx measurements in the TPC will also determine the sign of charged particles and identify muons, pions, and electrons. The TPC modules are described in Section 5.1.

    2. Fine Grained Detectors (FGDs): Two FGD modules, placed after the first and second TPCs, consist of layers of finely segmented scintillating tracker bars. The FGDs provide the target mass for neutrino interactions that will be measured by the TPCs, and also measure the direction and ranges of recoil protons produced by CC interactions in the FGDs, giving clean identification of CC QE and CC non-QE interactions. One FGD module will consist entirely of plastic scintillator, while the second will consist of plastic scintillator and water to allow the separate determination of exclusive neutrino cross-sections on carbon and on water. The FGD modules are described in Section 5.2.

- Electromagnetic calorimeter (Ecal): Surrounding the P0D and the tracker is an electromagnetic calorimeter. The Ecal is a segmented Pb-scintillator detector whose main purpose is to measure those $\gamma$-rays produced in ND280 that do not convert in the inner detectors and is critical for the reconstruction of $\pi^0$ decays. The Ecal is described in Chapter 7.

- Side Muon Range Detector (SMRD): Air gaps in the sides of the UA1 magnet are instrumented with plastic scintillator to measure the ranges of muons that exit the sides of the ND280. The SMRD also can provide a veto for events entering the detector from the outside and a trigger useful for calibration. The SMRD is described in Chapter 8.

In the document, the z axis is defined as the beam direction, and the x and y axes are defined as horizontal and vertical directions, respectively. Also included in this report are the muon monitor detectors, located downstream of the beam dump, and a grid of on-axis detectors in the 280 m pit for monitoring the neutrino beam direction. The muon monitor detectors include segmented ion chambers and an array of semiconductor detectors, as described in Section 4.1. The muon monitor detectors in the beam dump monitor the intensity, profile, and direction of the beam by detecting high energy muons from pion decay. The on-axis 280 m detectors, called N-GRID, are an array of iron/scintillator blocks that directly monitor the neutrino beam itself, as described in Section 4.2

## 2.2 General strategy of the oscillation measurement

To understand the role of the near detector in predicting the neutrino spectrum and interactions at the far detector it is useful to consider it in three rough sections. The on-axis neutrino monitor measures the profile of the neutrino beam, allowing the accurate determination of the off-axis angle. The tracking section of the off-axis detector (the TPC and the fine grained neutrino target (FGD)) is intended to measured the $\nu_\mu$and $\nu_e$fluxes and various charged current cross sections for signal and background processes. The electromagnetic calorimeter (Ecal) and $\pi^0$ detector (P0D) mainly measure $\pi^0$ production cross sections.

### 2.2.1 The Flux measurement

#### Neutrino spectrum measurement

The neutrino spectrum at the far detector is estimated by correcting the neutrino spectrum measured at the near detector by an extrapolation function obtained from the beam Monte Carlo simulation (far/near ratio). The reconstruction of the neutrino energy at the near detector is based on Charged-Current Quasi-Elastic (CCQE) interactions, where the neutrino energy is reconstructed measuring the muon or electron energy and its angle to the neutrino beam direction.

#### Coupling between cross section and flux

Neutrino cross section measurements and flux measurements are always coupled. To overcome this problem, the CCQE cross-section is used as a reference cross-section in the experiment. Measurements will be made of the flux multiplied by the CCQE cross-section ($\Phi_\nu \times \sigma_{CCQE}$), and for specific neutrino interaction the ratio of the cross section to the CCQE ($\sigma/\sigma_{CCQE}$) will be determined. The CCQE process is used as the reference cross-section because it is theoretically well understood, and reasonably pure samples can be obtained with good efficiency.

Because neutrino oscillations make the $\nu_\mu$ spectrum at the far detector significantly different from that at the near detector, one cannot simply use the ($\Phi_\nu \times \sigma$) at the near detector. Instead, it is necessary to measure all the different reactions as a function of the neutrino energy, normalized to the CCQE cross-section. For the NC case, where the energy of the neutrino is unknown, we have to rely on the fact that the spectrum of the neutrinos is similar in the near and the far detectors under the assumption of no sterile component.

#### Far/near extrapolation

Neutrino spectrum at the far detector is estimated by correcting the neutrino spectrum measured at the near detector by an extrapolation function obtained by the beam Monte Carlo simulation (the far/near ratio). The Monte Carlo simulation of the off-axis beam shows that the result is robust at the 5% level changing the pion production model at the proton target [23]. The pion production model will be checked at the near detector with CCQE neutrino interactions similar to the neutrino flux fit developed at K2K [8]. The radial dependency of the energy spectrum will also help to reduce the systematic error of the far/near extrapolation as it is explained below.

The off-axis near detector covers the area of 14 mrad, assuming that it is located at 280 m and it has a cross-section of $\pm$1.5 m. This large angular coverage complicates the prediction of the flux at the far detector, which covers a solid angle of the order of 0.1 mrad. On the other hand, the near detector has sufficient width to observe the running of the neutrino energy as the function

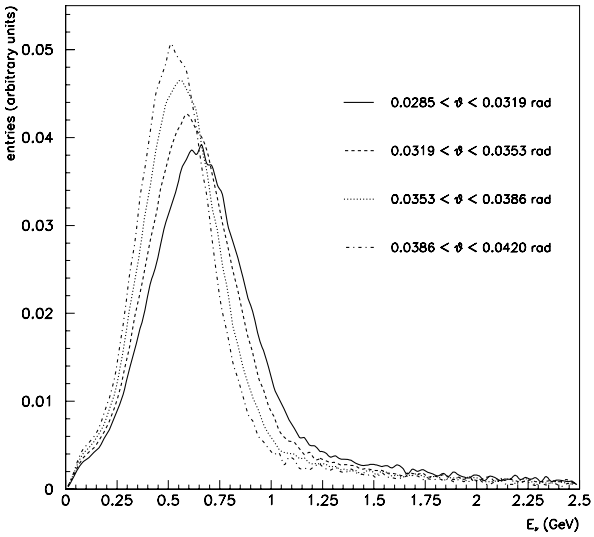


Figure 2.2: Neutrino energy spectra measured at different angular acceptance bands in the off-axis near detector. The spectra are normalized to the same area to show the change in the shape between the different sections.

of the off-axis angle. This can be seen in Figure 2.2, where the neutrino spectrum (normalized to the same integral) is shown for different angular acceptances. By monitoring the neutrino beam spectrum as a function of off-axis angle, one can check the Monte Carlo prediction for the variation of the beam profile with energy which is the main input to calculating the far/near ratio. We expect to detect a total of 130,000 events in each of the four sections assuming a total fiducial mass of 3 Tons in the ND280 with $5 \times 10^{21}$ POT. A useful measurement of the neutrino energy running can be performed even with 20-30% of the full beam intensity.

Any uncorrected difference in energy scale between the near and far detectors would introduce a complicated bi-polar distortion in the neutrino oscillation pattern in the $\nu_\mu$ disappearance spectrum. This is one of the main systematic uncertainties in the $\nu_\mu$ disappearance measurement, and to meet the measurement goal the energy scale must be understood at 2% level for the near detector. The Super-K detector [5] is calibrated within 2% for the muon momentum scale.

### 2.2.2 Neutrino cross section measurement

#### Neutrino backgrounds

The fraction of CCQE events assuming the predicted ND280 $\nu_\mu$flux is shown in Table 2.1. CCQE interactions account for almost 40% of the total charged current sample. The rest of the interactions represent a background in the CCQE sample that could bias the $\nu_\mu$spectrum measurement at the near detector. The dominant background is from $CC - p\pi^+$.

The backgrounds for $\nu_e$ appearance in Super Kamiokande come mainly from NC interactions which produce $\pi^0$ and intrinsic $\nu_e$ beam contamination. Neutrino cross sections are not very well measured yet in the T2K energy region, which affects the precision of the flux and background predictions at the far detector. Measurements of differential cross sections are needed to understand

| Int. Mode | Fraction | Events/$10^{21}$ POT/ton |
|---|---|---|
| $CC-QE$ | 38 % | 65038 |
| $CC-p\pi^+$ | 11 % | 17846 |
| $CC-p\pi^0$ | 3 % | 4887 |
| $CC-n\pi^+$ | 3 % | 5107 |
| $CC-Coherent\,\pi^+$ | 1 % | 2189 |
| $CC-multi\,\pi$ | 7 % | 11943 |
| $CC-DIS$ | 8 % | 13057 |
| $NC-Elastic\,n$ | 9 % | 15671 |
| $NC-Elastic\,p$ | 8 % | 13581 |
| $NC-n\pi^0$ | 2 % | 2837 |
| $NC-p\pi^0$ | 2 % | 3519 |
| $NC-p\pi^-$ | 1 % | 1931 |
| $NC-n\pi^+$ | 1 % | 2300 |
| $NC-Coherent\,\pi^0$ | 1 % | 1099 |
| $NC-multi\,\pi$ | 2 % | 3639 |
| $NC-DIS$ | 2 % | 4022 |

Table 2.1: Total number of events predicted by the NEUT Monte Carlo for the Near Detector, per ton and per $10^{21}POT$. The Fractions of different interaction modes are also shown.

the detector response in the far detector.

**Hadronic uncertainties**

In the energy region of the T2K neutrino beam, neutrino interactions are not very well known. In addition, there is alack of knowledge of the interactions of the hadrons produced by neutrinos within the nucleus. Both the nuclear description and cross-sections for these processes are not known to better than 30%. Both quantities have to be measured in the near detector to be able to subtract the background.

The measurement approach is to decouple the more reliable leptonic measurement from nuclear effects and study them separately. Since the CCQE and CC1$\pi$(via $\Delta$ resonance) reaction are two-body reactions, initial neutrino energies can be reconstructed using out-going lepton momentum without introducing information from the hadrons. The recoil masses of proton and $\Delta$ are assumed from CCQE and CC1$\pi$ models respectively. Monte Carlo parameters, such as the nucleon potential, Fermi motion, and axial mass ($M_A$), will be tuned using lepton energy/angular ($Q^2$) distributions.

We probably cannot reconstruct the initial neutrino energy for multi-pion and neutral current processes. We have to be cautious because the $NC-multi\,\pi$ and $NC-1\pi$ interactions are the second most copious backgrounds for $\nu_\mu$ disappearance, as shown in Table 2.2. The minimal program for $CC-N\pi$, $NC-1\pi$ and $NC-N\pi$ is the measurement of the pion momentum spectra and multiplicities in the near detector (as a function of the muon energy for the $CC$ case).

Hadronic effects, such as re-scattering and absorption, are measured separately using recoil protons and pions in the final states. Comparison between the expected and observed angles of recoil protons in CCQE ($\Delta\theta_P$) can be used to understand the non-QE background contamination. Fine granularity of the FGD is required to have sufficient proton angular resolution.

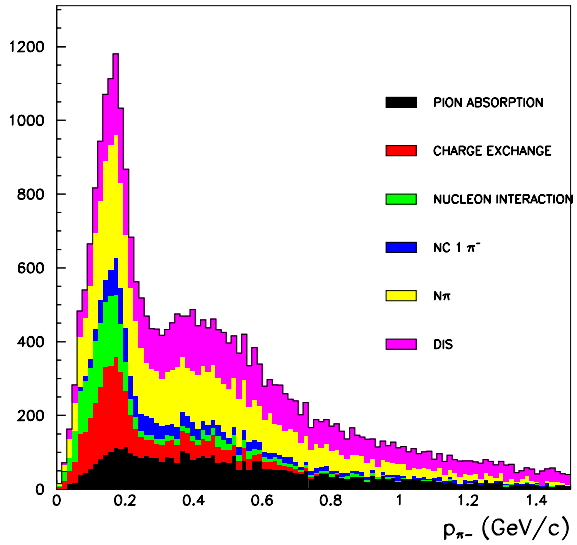


Figure 2.3: Momentum distribution of the final state $\pi^-$ in neutrino interactions at the ND280. The different contributions to the flux are shown.

A systematic study of resonant single pion measurement through $\Delta$ resonance can be performed by detecting pions. Isospin rules relate the production of charged and neutral pions as described in [24]. This relation could help us in over-constraining some of the production channels.

Other possibilities to study hadronic uncertainties are under study. For example, it is possible to measure hadronic interactions within the target nucleus from $\pi^-$ produced in neutrino interactions. There are few reactions that provide $\pi^-$ in the primary neutrino interactions. Almost half of $\pi^-$ below 300 MeV/c are produced in re-interactions of hadrons inside the nucleus. Figure 2.3 shows the momentum distribution of $\pi^-$ produced at the near detector. The measurement of the quantity and the spectrum could help in understanding this mechanism. Good charge, momentum and particle identification (PID) capabilities are required to carry out this kind of study.

## 2.3 The muon and neutrino monitors.

Accurate control of the beam direction is essential to reduction of the systematic uncertainty in long baseline experiments. In the case of T2K, 1 mrad change in the neutrino direction corresponds to about 25 MeV shift in the peak neutrino energy, which contributes to the systematic uncertainty in the measurement of $\Delta m^2_{23}$. In order to achieve the aimed precision of the experiment ($\delta(\Delta m^2) \simeq 10^{-4}$ eV$^2$), the direction of the neutrino beam should be controlled and monitored with precision much better than 1 mrad. This is the principle goal of the muon and neutrino monitors.

The muon monitor measures the direction, profile and intensity of the beam on a spill by spill basis. It will be located downstream of the beam dump and detect high energy ($> 5$ GeV) muons which penetrate the dump. Because the muons are produced from the same parent particles as the neutrinos, the muon properties are directly associated with those of the neutrinos. The spatial

| Int. Mode | Fraction |
|---|---|
| $CC-QE$ | 65 % |
| $CC-1\pi$ | 20 % |
| $CC-coh\pi$ | 1 % |
| $CC-n\pi$ | 3 % |
| $NC-1\pi$ | 7 % |
| $NC-N\pi$ | 7 % |

Table 2.2: Fraction of interaction modes around oscillation maximum ($0.35GeV < E_{\nu}^{rec} < 0.8GeV$) for the 1 ring muon-like event as predicted by the NEUT Monte Carlo.

profile and intensity of the muons are sensitive to the condition of the magnetic horn system and the accuracy of the proton targeting. The muon monitor will also provide information necessary for tuning of the beam in the commissioning of the experiment. It therefore needs to be sensitive to the beam condition, e.g. proton beam position at the target.

The expected muon flux at the position of muon monitor is $\sim 10^8$ muons/cm$^2$/spill at the beam center, which corresponds to $\mathcal{O}(10^{15})$ muons/cm$^2$ for one year of operation. The detectors must survive this high radiation. Because the muon monitor is the only instrument that can assure the quality of the neutrino beam on a spill by spill basis, a failure of the muon monitor would cause deadtime for the whole experiment. Therefore, the detectors should be robust and stable.

The muon monitor observes only the small fraction of muons which have energy greater than 5 GeV. Therefore, it is also important to directly measure the direction of the neutrino beam. The neutrino monitor will be installed in the near detector hall to measure the neutrino beam direction and profile using neutrinos directly. The neutrino monitor is required to measure the neutrino beam direction with precision much better than 1 mrad. The neutrino monitor guarantees the direction of the neutrino beam pointing to the far detector, after this has been tuned by the muon monitor. The neutrino event rate around the beam center is estimated to be $\sim 0.3$ events/ton/spill. In order to monitor the stability of the neutrino event rate (direction) at the 1% (1 mrad) precision within a single day ($\simeq 2.5 \times 10^4$ spills), $\mathcal{O}(1)$ ton fiducial mass is necessary for the detector. In addition, the variation of the efficiency of the detector across the beam profile should be calibrated at a precision of 1% during the experiment.

## 2.4 The T2K tracker

### 2.4.1 Neutrino oscillation backgrounds

The $\nu_\mu$disappearance signal in SK is based on events which display a single muon-like Cherenkov ring. The contribution of the different interaction modes to this channel after neutrino oscillation is shown in Figure 2.4. The proportions of the different reactions in the oscillation region ($0.35GeV < E_\nu < 0.8GeV$) are listed in Table 2.2. The main background comes from $CC1\pi$ interactions, followed by the $NC1\pi$ and $NC-multi\,\pi$ channels. The $CC1\pi$ background appears when the pions in the final state are not visible, the $NC1\pi$ and $NC-multi\,\pi$ are produced by single pions misidentified as single mu-like rings in SK. The dominant backgrounds therefore all produce pions in the final states, and thus understanding pion production and absorption mechanisms via nuclear re-interactions is fundamental to understand backgrounds at Super-Kamiokande.

The background sources for the $\nu_e$ appearance study are mainly from NC $\pi^0$ production and

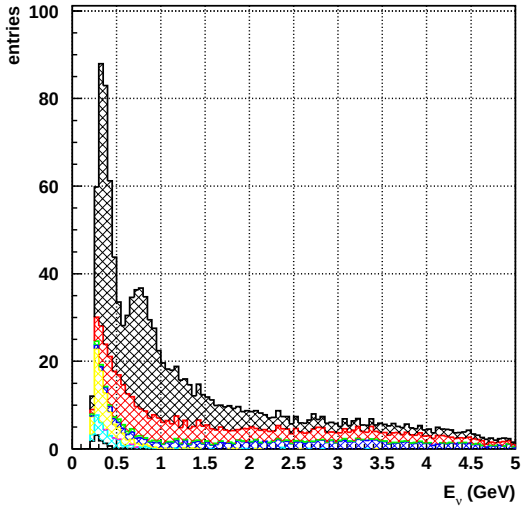


Figure 2.4: The reconstructed neutrino energy distribution of single muon-like ring events at Super-Kamiokande after neutrino oscillations. Contribution of the different $\nu_\mu$interaction modes are shown from top to bottom: black histogram stands for CCQE, red for $CC1\pi$, and yellow for $NC1\pi$.

intrinsic $\nu_e$beam contamination. Both backgrounds have to be measured with a precision better than 10% in the energy region of the oscillations.

### 2.4.2 Requirements on the tracking detectors

**Muon measurement**

As outlined above, CCQE events are used to measure the neutrino flux and spectrum. The measurement of the muons is therefore fundamental to the experiment. These muons are soft and are typically produced with large angles with respect to the neutrino beam (see Figure 2.5).

The energy spectrum of neutrinos at the far detector is also provided via the measurement of CCQE interactions. The estimated neutrino energy is very sensitive to the momentum scale of the reconstructed muons, however momentum scale systematics are different in the near and far detectors. This fact makes the systematic uncertainty in the energy scale one of the main systematic uncertainties. The muon momentum scale is required to be understood at 2% level as discussed in previous sections. On the other hand, the muon momentum is only required to be measured with a moderate resolution since the neutrino energy reconstruction is affected by the relatively large smearing due to the Fermi motion of the nucleon target. Monte Carlo studies suggest that the momentum resolution should be better than 10%, which is the value induced by Fermi motion in a Carbon target.

High momentum muons can also be used to estimate the $\nu_e$ production rate. The high energy tail of the $\nu_\mu$ spectrum is produced in Kaon decays at the decay volume, which are also involved in $\nu_e$ production via $K_{e3}$ decays. This measurement could help to understand the hadron production model in the beam Monte Carlo simulations, and, what is more relevant, to help the predict of $\nu_e$ flux.

The neutrino flux needs to be monitored by the FGD and TPC system with better than 5% accuracy, which is limited by the far/near extrapolation error.

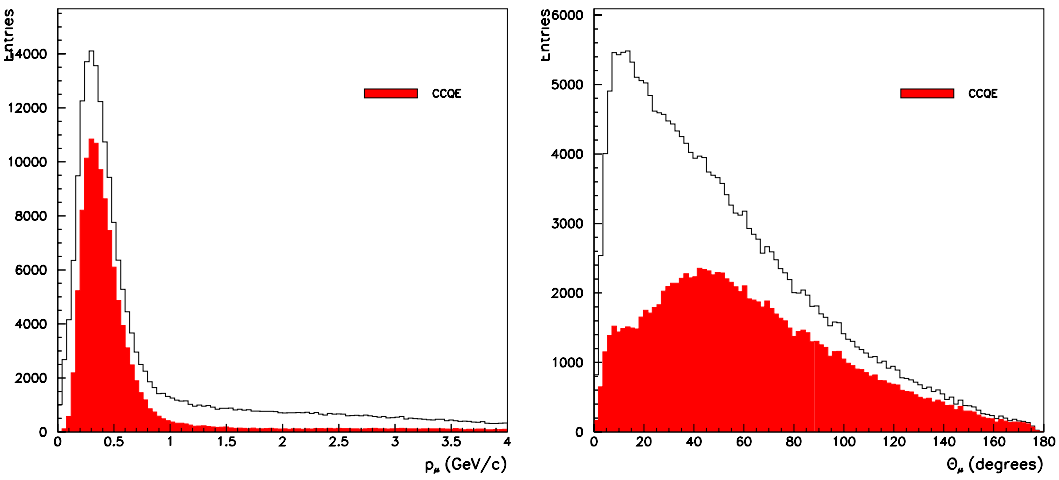


Figure 2.5: Momentum (left) and angular (right) distributions of the final state $\mu$ in the neutrino interactions at the T2K near detector.

The magnet spectrometer provides momentum measurement with a resolution of better than 10%. Special care has to be taken to calibrate the energy deposited in the target sections. The time projection chamber (TPC) is chosen as a near detector tracker because its performance is rather uniform for a wide range of angles (from 0 to almost 90 degrees) and it also reduces the multiple scattering for tracks reaching its active volume. The last property is very useful in measuring low momentum tracks with rather low magnetic field (0.2 T). The number and width of the TPC volumes are chosen so that it can also provide reasonably good momentum resolution even for relatively high momentum muons. High momentum muons are also measured in several TPC's at the time, increasing the effective resolution for those tracks.

**Proton measurement**

Detecting the recoil protons allows a high purity CCQE reaction sample to be selected. The method, similar to the one used in K2K, consists of calculating the angle, $\Delta\theta_{proton}$, between the measured proton direction and the one predicted from the muon momentum under the CCQE assumption. The proton momentum distribution, as shown in Figure 2.6, is soft and the typical proton range in the detector is short. The main problem is to reconstruct protons isolated from the main muon track. An important component to be optimized is the segmentation of the active target section (FGD). A fine FGD granularity is needed to increase the efficiency of CCQE tagging. Since the neutrino interaction Monte Carlo predicts a weak dependency of the proton momentum with the neutrino energy, the threshold for protons can be kept relatively large. The fact that low momentum protons are produced in nuclear reinteractions makes this region less interesting for CCQE tagging, but more important for the description of nuclear interactions.

**Charged pion measurement**

The pion measurement is important to understand backgrounds at SK and to identify exclusive neutrino interactions. Pions are difficult to measure in a high density environment, due to hadronic interactions of the pions with the neutrino target. The interaction cross section of charged pions is

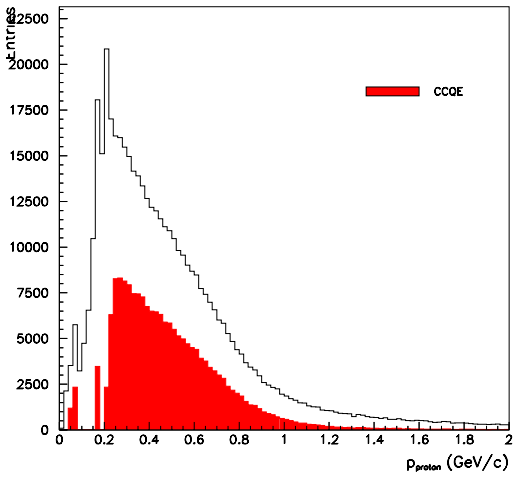


Figure 2.6: Momentum distribution of the final state $proton$ in the neutrino interactions at the ND280.

as large as 200 mb and the interaction length only 10 cm at the $\Delta$ resonance, where many of the pions are produced. Once a pion interacts, information on its energy is lost and it is difficult to predict the response of the far detector.

The differential cross section for the production of $CC-1\pi$ background, which is the dominant non-QE background in the $\nu_\mu$ disappearance measurement, will be measured precisely by the spectrometer system. This $CC-1\pi$ measurement, a measurement of the sub-leading NC $\pi^+$ channel, and a measurement of the $\Delta\theta_{proton}$ channel are required to achieve the goal of less than 10% in systematics in the non-QE/QE ratio.

**Electron detection and the $\nu_e$**

The tracking section of ND280 is the best place to measure the $\nu_e$ beam contamination. In addition to the measurement of the Kaon contribution to the beam from high energy $\nu_\mu$, the tracking section provides a momentum measurement and three independent methods to identify electrons:

- ionization in the TPC volumes.
- pattern of energy deposition in the FGD scintillator targets.
- $\frac{E}{p}$ using the Ecal.

it is also convenient because the normalization to $\nu_\mu$ is done with the same detector geometry, and also because the tracker section is optimized for high purity CCQE identification.

The comparison between the predicted fluxes at the near detector are shown in Figure 1.7, the fraction of $\nu_e$ varies from 0.5% in the oscillation region to 6% at high energies. If the TPC provides better than $3\sigma$ $e/\mu$ separation by dE/dx (see Section 5.1.8), it will be sufficient to achieve a good $\nu_e$ purity. From figure 1.7, the estimation of the number of events per ton per $10^{21}$ POT at the near detector inside the signal region is of the order of 1300. Including the CCQE fraction (40%) and a conservative inefficiencies (from K2K experiences) in the CCQE selection (50%) the

total number of events is around 270, enough to achieve the 10% error needed by the $\nu_e$appearance analysis with $10^{21}$ POT and one ton of exposure. Assuming a signal to background ratio of 0.5 (from 1% muon misidentification) and a systematic uncertainty of 10% in the misidentification value we estimate a total error in the $\nu_e$selection of approximately 14% at $10^{21}$ POT and 10% at $5 \times 10^{21}$ POT. A muon-electron separation better than 1% or a systematic uncertainty in this number to better than 10% is needed..

**Electromagnetic shower measurement**

The electromagnetic calorimeter surrounding the tracking region (ECAL) should provide excellent particle identification of the electron signal from the beam $\nu_e$ contamination. Cutting on the ratio E/P should provide the required $\mu$/e separation factor of 10000. The ECAL is also useful for a systematic study of the production cross sections, in particular the single pion production through $\Delta$ resonance for both charged and neutral pions.

The electromagnetic calorimeter in the tracking section can also be used for studying neutral current $\pi^0$ background. The idea is to surround the tracker section with a calorimeter with some tracking capabilities. From constraining the $\pi^0$ vertex in the FGD target regions, which are almost 1 m apart, using the pointing capabilities of the calorimeter, a decent $\pi^0$ detection capability is achieved, detail description can be seen in Appendix A.

**Water target**

It is desirable to measure the neutrino cross section on water to reduce the systematic uncertainties arising from nuclear effects. On the other hand, it is also important (see proton section) to lower the proton threshold to improve the purity for CCQE selection. One possibility being considered is to use water soluble scintillator, which is fully active, and the other is to insert a water layer in between active scintillator layers. The former is better from physics point of view, but technically challenging. The latter is technically easier, but raises the momentum threshold of recoil protons.

There are two important nuclear effects that cause the neutrino interactions between carbon (scintillator) and oxygen (water) to differ. First, the out-going lepton momenta are affected by differences in the nuclear potentials, Pauli blocking, and Fermi motion. In principle, these are understood from electron scattering data. Another effect is the nuclear absorption and re-scattering of protons and pions. In the Fermi gas model, the difference in nuclear effect between carbon and oxygen is $(16/12)^{1/3}$=1.10, or 10%, which is close to the systematic uncertainty we would like to achieve. For example, the CC1$\pi$ background contributes at the same level as the CCQE signal at the oscillation maximum in the far detector. Taking the pion absorption probability of 40% and its systematic uncertainty of 30%, as assumed in K2K analysis, the uncertainty of CC1$\pi$ background contribution due to nuclear effects would become 10%$\times$40%$\times$30%=1.2%, which meets our goal without using water target. On the other hand, the assumption of the Fermi gas model introduces further model-dependent systematic uncertainties which are difficult to quantify. For example, an expected pion absorption process is $\pi^+ d \rightarrow pp$ reaction in the nucleus, but this process explains only fraction of the pion absorption and the rest is not well understood. Significant structure-dependent nuclear uncertainty exists. Therefore, it is prudent to measure the background on a water target and bound this systematic uncertainty. Water and scintillator (CH) are also different in their neutron to proton ratio. For the $\nu_\mu$ disappearance measurement, the main background of CC1$\pi^+$ is produced from neutrino interactions on protons, whereas the CCQE signal is produced on neutrons. Therefore, the signal-to-noise ratio changes with the neutron/proton ratio. Similarly,

for the $\nu_e$ appearance measurement, half of the NC$\pi^0$ background is produced from neutrino interactions on proton targets, whereas the CCQE signal is produced on neutron targets, and thus the signal-to-noise ratio depends on the neutron/proton ratio.

One way to resolve this is to do a subtraction. Consider mixing two materials in the FGD's: 100% polystyrene scintillator (CH) and 50% water and 50% polystyrene scintillator. By subtracting the former from the latter, one could extract the cross section on water. Statistically, this would require 5 times more statistics compared to the pure water case. By having the two FGD's, it is expected that the systematic uncertainty due to nuclear effects in the CCQE rate and nQE/QE ratio of $\nu_\mu$disappearance will be constrained to less than the 10% level as required.

## 2.5 The T2K P0D

One of the main limitations facing the T2K electron neutrino appearance search will be the understanding of backgrounds which are dominated by two distinct sources with roughly equal contributions. The first crucial source of background is the result of $\nu_e$ in the primary beam which cannot be distinguished from the oscillated $\nu_\mu \rightarrow \nu_e$. Fortunately, the electron neutrino flux is suppressed relative to the $\nu_\mu$ flux and has an energy spectrum which differs from that of the expected $\nu_e$ appearance signal. The other significant source of background results from neutral current $\pi^0$ production by muon neutrinos where the $\pi^0$ is not fully reconstructed in Super-Kamiokande. It is expected that the statistical uncertainty on these backgrounds will approach 10% during the first phase of T2K. The $\pi^0$-detector (P0D) has been optimized to address these backgrounds.

### 2.5.1 Motivation, requirements, and technique

The P0D is primarily intended to measure events that contain electrons and gamma-rays. The particular goals of the P0D are to measure the inclusive $\pi^0$ production rate by $\nu_\mu$ on oxygen, as well as partially inclusive neutral and charged current production rates. In addition to an accurate determination of the inclusive rate, it will be important to measure rates for various exclusive $\pi^0$ production channels, such as $\nu_\mu n \rightarrow \mu^- p \pi^0$ and $\nu_\mu N \rightarrow \nu_\mu N \pi^0$. The P0D will provide new data for these and other relatively poorly known partial cross sections in the energy range below $1\ \mathrm{GeV}$. Finally, the P0D will provide a measurement of the intensity and energy spectrum of the beam-associated electron neutrino flux by directly searching for $\nu_e$ quasi-elastic events.

These goals require that the P0D meets several criteria in terms of mass and event reconstruction ability. First, the P0D is intended to study processes with relatively small partial cross sections compared to the total neutrino cross section so it must have relatively large mass as well as high reconstruction efficiencies (see section 2.5.2). Further, since the expected $\pi^0$ momentum distribution peaks near 300 $\mathrm{MeV/c}$, the P0D must have a threshold to reconstruct gamma-rays that is below 100 $\mathrm{MeV}$. Finally, the total P0D target mass will be significantly smaller than the total mass of the surrounding Ecal and magnet so it must have adequate vertex resolution to eliminate background events from outside of its fiducial volume.

### 2.5.2 Neutral current $\pi^0$ sample: Statistics and background

In $10^{21}$ protons on target, the T2K neutrino beam is expected to produce approximately 100,000 events/ton at the ND280 off-axis detector site. Approximately 88% of the recorded events will result from charged current interactions with about 43% of the events being from QE interactions. Single pion interactions will contribute approximately 21% of the charged current rate, and an

| | |
|---|---|
| 76% | 1 $\pi^0$/ protons, neutrons, and/or nuclear gamma rays |
| 13% | 2 $\pi^0$s w/ protons, neutrons, and/or nuclear gamma rays |
| 4% | multiple $\pi^0$s w/ protons, neutrons, and/or nuclear gamma rays |
| 6% | 1 $\pi^0$ 1 $\mu$ w/ protons, neutrons and/or nuclear gamma rays |

Table 2.3: Interactions in a sample of event kinematics selected to study the background for single $\pi^0$ events. The selection criteria are discussed in the text.

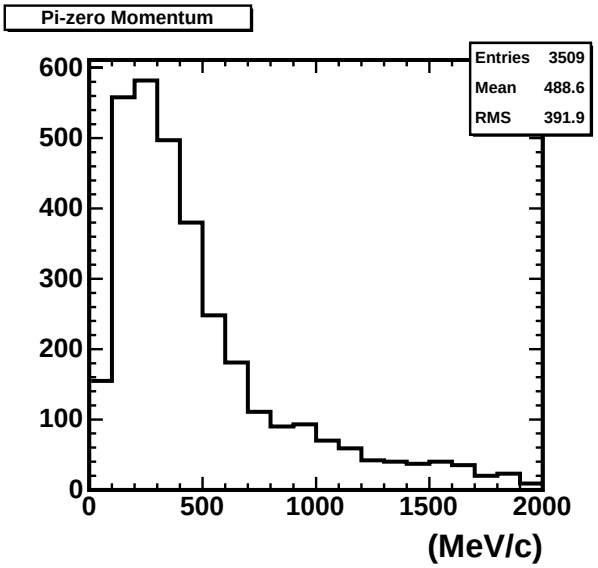


Figure 2.7: The momentum distribution of $\pi^0$s produced in NC events at the ND280 off-axis detector, as predicted by the NEUT Monte Carlo generator. The vertical scale is arbitrary.

additional 15% of events will result from multi-pion production. Neutral current interactions contribute about 30% of the total interaction rate, however the majority do not produce a signal in our detectors. Only 12% of the events are expected to be from neutral current interactions. Most of these events (7%) will be from single $\pi^0$ production as seen in Table 2.3.

Particles produced in neutrino interactions are expected to have a mean momentum of approximately 500 $\mathrm{MeV/c}$ (see Figure 2.7). It can be seen that while the majority of particles will have relatively low momentum, a significant number will have momenta of more than 1 $\mathrm{GeV/c}$. The $\pi^0$s which create background at Super-Kamiokande have momentum between 250 and 700 $\mathrm{MeV/c}$.

### 2.5.3 Predicting the $\pi^0$ background at Super-Kamiokande

Predicting the number of $\pi^0$ inclusive events at Super-Kamiokande as a function of $\pi^0$ momentum is one of most important roles of P0D. The prediction may be done in two ways. First, one may attempt to directly predict the rate of $\pi^0$ production at Super-Kamiokande as a function of momentum and with or without the presence of other final state particles above Cerenkov theshold. Then a Monte Carlo simulation is used to predict the background from the predicted $\pi^0$ containing events. A second approach is to compare the prediction of $\pi^0$ from the 280 $\mathrm{m}$ detector to the fully reconstructed 2-ring $\pi^0$ at Super-Kamiokande. The second approach is crucial because it provides a benchmark against which to test the Super-Kamiokande simulation of response to $\pi^0$s. Then, the reconstructed $\pi^0$ events at Super-Kamiokande can be used to predict the background to electron neutrino appearance from the ratio of Monte Carlo signal and background efficiencies.

Either approach requires correcting for the differences in nuclear composition and neutrino spectrum at the near detector and at Super-Kamiokande, as described below.

#### Nuclear Correction

In the P0D, the nuclear correction is deduced by simply subtracting events from the water-containing portion of the detector from the non-water portion of the detector. Because the water is a relatively small fraction of the total fiducial mass of the P0D ($1.3$ of $4.8$ tons total), the effective statistical power after this subtraction is equivalent that of a pure water target of $0.39$ tons (the equivalent of 480 $\pi^0$ background candidate events per $10^{21}$ protons on target in the relevant $\pi^0$ momentum range).

#### Near to Far Correction

Because the neutrino spectrum at 280 $\mathrm{m}$ is different from that at Super-Kamiokande, the $\pi^0$ momentum distribution and number at the at 280 $\mathrm{m}$ and at Super-Kamiokande may be different. The primary difference comes from the much smaller number of high energy neutrinos at Super-Kamoikande. Monte Carlo generators, which predict exclusive $\pi^0$ production rates and momenta are based primarily on models only weakly verified by data. Consequently, one finds that NEUT and NEUGEN find significantly different predictions for this far to near ratio; therefore, we chose to measure this from the data.

The far to near ratio prediction is determined by convoluting the flux ratios at the two detectors from the beam Monte Carlo with $d^2\sigma/dE_\nu dp_\pi$ from the data. The latter can only be measured from charged-current events, and we will measure it using $\nu_\mu n \to \mu^- p \pi^0$ (from the P0D with the muon reconstructed TPC tracker) and $\nu_\mu N \to \mu^- N \pi^+$ (from the FGD and TPC tracker). The former will have higher statistics because of the P0D mass, while the latter is a direct isospin rotation of single NC production of $\pi^0$s.

**Systematics on the SK $\pi^0$ background prediction**

Beyond the far-to-near correction, we have considered several sources for systematic error on the prediction of inclusive neutral current $\pi^0$ events produced at Super-Kamiokande using the measurement on the same neutral current inclusive $\pi^0$ events at P0D. These sources come are:

- Uncertainty arising from the statistical errors on the measurement at P0D, including the subtraction to derive the rate on the water target
- Uncertainty arising from the detection efficiency for the neutral current inclusive $\pi^0$ events (signal events).
- Uncertainty arising from the detection efficiency from non neutral current events (background events).

Here the uncertainty in the detection efficiency should be understood in a broader sense than usual. It includes uncertainties in the estimate of the number of target nucleons and in the knowledge of event migration due to $\pi^0$ energy resolution. Further, the detection efficiency uncertainty includes systematic uncertainty associated with the subtraction that is required to obtain the event rate on water. A particularly important component will come from the uncertainty in the relative efficiency of different portions of the P0D.

The systematic error on the number of NC inclusive $\pi^0$ events produced arises from uncertainties in the estimation of the signal and background detection efficiency, and in the estimation of the cross section ratio for background to signal. For simplicity, the neutrino flux is assumed to be known, but will also contribute to the systematic error.

Table 2.4 is a summary of the contribution from each type of uncertainty as a function of $\pi^0$ momentum. The $\pi^0$ flux uncertainty is dominated by the statistical error and the error on signal detection efficiency (in the broad sense as explained above). Note that the total error for the sample of interest for producing background at Super-Kamiokande (250–700 MeV) is estimated to be well below 10% for $10^{21}$ protons on target.

| | Uncertainty vs. $\pi^0$ Momentum (MeV) | | | | |
|---|---|---|---|---|---|
| | 200–300 | 300–400 | 400–600 | 600–800 | 800+ |
| Statistical ($10^{21}$ protons) | 7% | 6% | 8% | 17% | 23% |
| "Signal" Efficiency | | | | | |
| 10% | 8% | 8% | 8% | 9% | 9% |
| 7% | 6% | 6% | 6% | 6% | 7% |
| 5% | 4% | 4 % | 4% | 5% | 5% |
| 4% | 3% | 3% | 2% | 3% | 3% |
| "Background" Efficiency | | | | | |
| 10% | 2% | 2% | 2% | 1% | 1% |
| 7% | 1% | 1% | 1% | 1% | $<$1% |
| Background/Signal Rate | | | | | |
| 20% | 4% | 4% | 4% | 3% | 2% |
| 10% | 2% | 2% | 2% | 1% | 1% |
| Near to Far | | | | | |
| Scenario above | 1% | 5% | 6% | 12% | 12% |

Table 2.4: Summary of contributions to the systematic error on the number of $\pi^0$ events in a particular energy band at the 280 $\mathrm{m}$ detector from different sources. The first column gives the achieved systematic uncertainty on the parameter. The remaining columns give the effect of that systematic error on the number of $\pi^0$ events.

# Chapter 3

# Neutrino Experimental Facility

## 3.1 Introduction

The neutrino experimental facility at the near location consists of the muon monitor pit, immediately following the beam dump, and of the neutrino experimental hall, designed to host the on-axis and off-axis neutrino detectors. In this chapter we give a description of the two experimental areas, and of the magnet. We recall that at the off-axis position, we propose to measure the neutrino interactions, and hence the energy spectrum and composition of the neutrino beam, with a fine-grained detector placed inside a uniform magnetic field. For this purpose we plan to use the magnet built at CERN for the UA1 experiment, and subsequently used by the NOMAD neutrino experiment. The 850 tons iron yoke of the magnet will also act as a supporting structure for the inner detectors, and also because of this, we have chosen to include the magnet description in this chapter on the neutrino facility.

## 3.2 Muon Monitor Pit

Figure 3.1 shows conceptual drawings around the muon monitor pit. It is a room with a size of $6.6(x) \times 8.2(y) \times 4.0(z)$ m$^3$, located downstream of a beam dump system. The beam dump system is composed of a water-cooled graphite+copper core, placed in a helium vessel, and iron shield structure surrounding the core. The thickness of these materials are optimized so that the energy threshold of muons to be 5 GeV, as will be discussed later. The beam dump and muon pit is surrounded by $4 \sim 5$m-thick radiation-shielding concrete walls.

During the first phase operation with 0.75 MW beam power, the hadron flux in the muon monitoring pit is expected to be 0.5$\sim$1$\times 10^5$ (1$\sim$2$\times 10^6$)/cm$^2$/s with energy $\geq$ 1 MeV (thermal neutron), respectively, and the radiation level is to be $\sim 200$mSv/hour. The residual dose rate for an iron, with a size of $1\mathrm{m}^2 \times 10\mathrm{cm}$ thick, is to be 20(50) $\mu$Sv/hour for 30 days operation with 1 day cooling (20 years with 1day), respectively.

## 3.3 Neutrino experimental hall

The neutrino experimental hall is called the ND280 hall (the neutrino detector hall at 280m from the target point). The location of the ND280 hall is shown in Figure 3.2. The ND280 hall is being designed as follows, which is drawn in Figure 3.3.

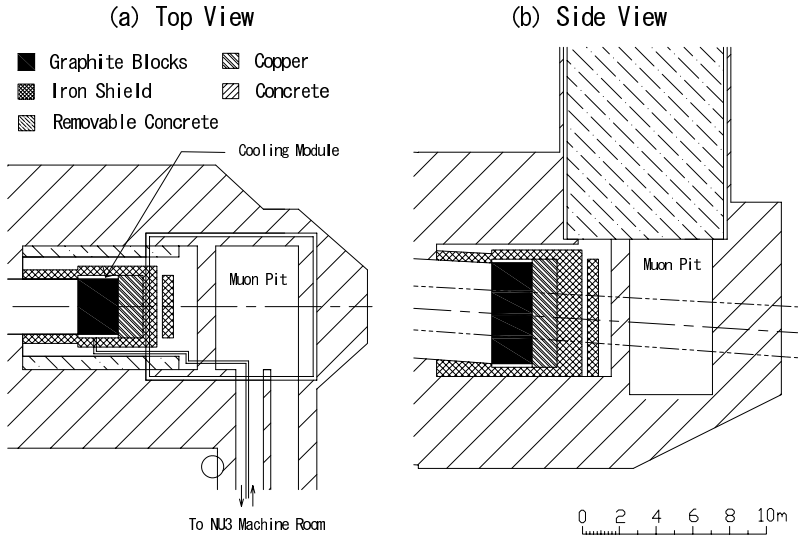


Figure 3.1: Conceptual drawing around the muon monitor pit.

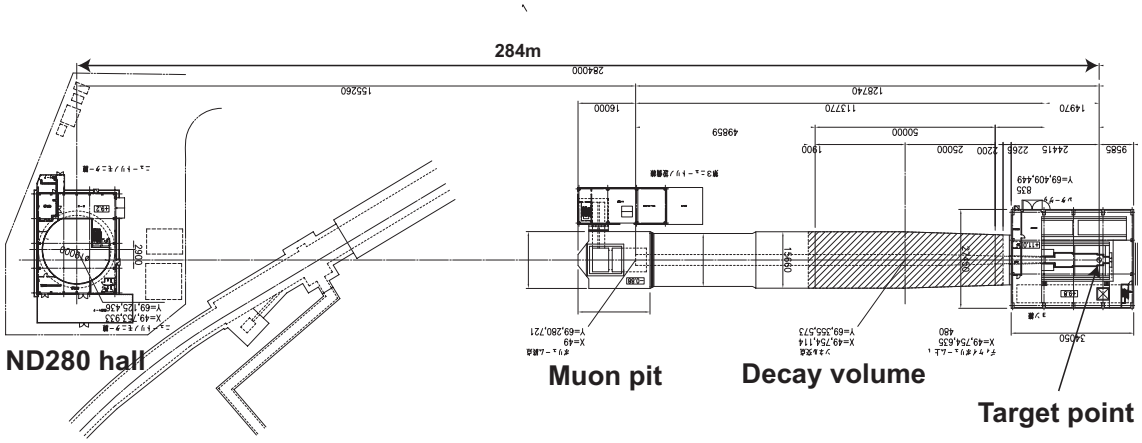


Figure 3.2: Location of the muon pit and the ND280 hall.

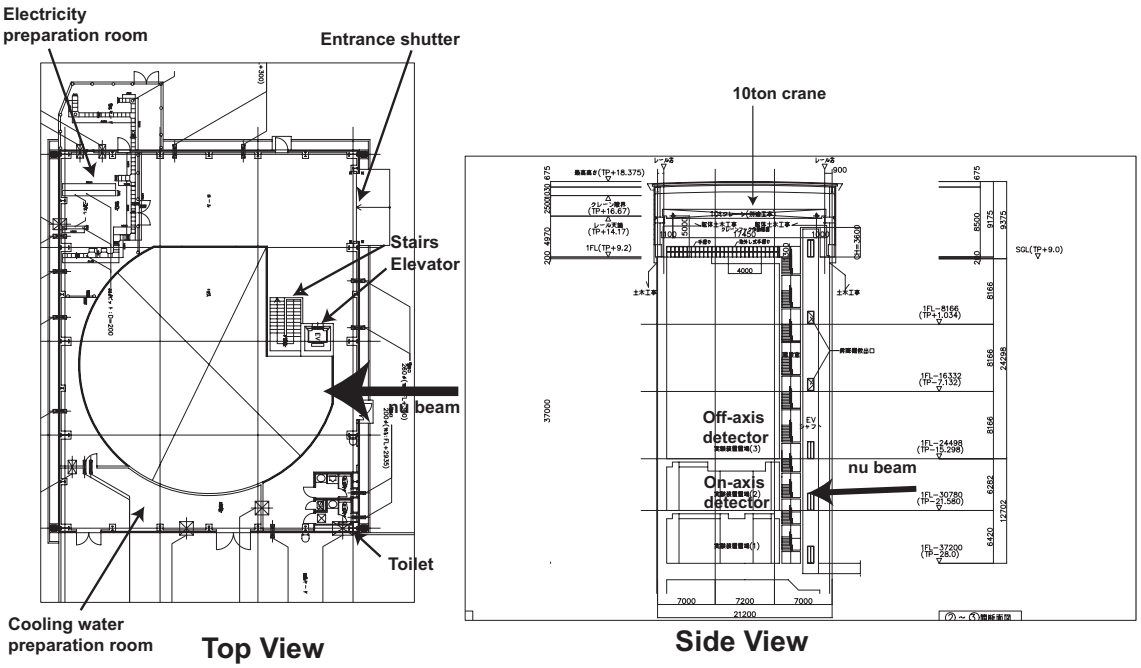


Figure 3.3: Current design of the ND280 hall.

The ND280 hall has a pit with a diameter of 19m and a depth of 37m, which incorporates both the on-axis and off-axis detectors. The B1 floor, which is about 24m deep, is for the off-axis detector. The off-axis detector is nearly located on the line between the target point and the SK position. The B2 floor, which is about 33m deep, is for the horizontal part of the on-axis detector. The B3 floor, which is 37m deep, is for the deepest part of the vertical on-axis detector. The exact location of the on-axis detector will be fixed after the off-axis angle is fixed. The current nominal off-axis angle is 2.5 degrees and the on-axis beam line passes at about 4m above the B2 floor. This facility design can accommodate with the off-axis case of $2.5 \pm 0.5$ degrees with the condition that the on-axis detector covers the $\pm 4$m area.

The hut with a size of 21m $\times$ 28m covers the pit, and has a 10ton crane. The hut is a little bit shifted to the north with respect to the pit center in order to use the north area in the hut for the unloading of detector components and for the detector preparation. The effective height of the crane is 5m and its dead space is about 3m from the north and south walls and 2m from the east and west walls. The hut has an entrance shutter 5m wide and 3.9m high. There are a 6-people elevator and stairs. Some area in the hut at the ground floor is used for the electricity preparation and the cooling water preparation.

The construction of the ND280 hall and the installation of the detectors will be done in the following steps starting in Spring 2007.

1. The excavation of the pit.
2. The construction of the underground floors.
3. The installation of the magnet yokes and coils using external cranes.
4. The construction of the hut including the 10ton crane.

Figure 3.4: The UA1 magnet.

5. The installation of the on-axis detector.

6. The installation of the off-axis detector.

## 3.4 The magnet

### 3.4.1 Description

The UA1 magnet is presently stored at CERN, and the CERN Council has approved its donation to the T2K experiment. The magnet will provide a horizontal uniform field of 0.2 T, perpendicular to the neutrino beam direction over an inner volume of 88 $\mathrm{m}^3$. A schematic drawing of the magnet, placed on its support structure, is shown in Figure 3.4.

The magnet consists of two halves which are mirror symmetric about a vertical plane containing the beam axis. Each half consists of 8 C-shaped flux return yokes, made of low-carbon steel plates. The total weight of the yoke is 850 tons. The external dimensions of the magnet are 7.6m(L)x6.1m(H)x5.6m(W). Figure 3.4 shows the two halves of the magnet apart, to make visible the coils inside the magnet. The magnet will be in that open position when assembling the inner detectors. Normal operation will be with the two halves in contact. The coils consist of aluminum conductors of square cross-section (54.5x54.5$\mathrm{mm}^2$). The peculiar shape of the coils, forming a hole along the magnet axis, was specifically designed to accommodate the beam pipe in the UA1 experiment. The coils will provide a uniform horizontal field, orthogonal to the beam axis. The magnet was originally designed to operate with a current of 10 kA, providing a field of 0.67 Tesla, with a power consumption of 6 MW. We propose to operate the magnet with a current of 3 kA corresponding to a field of 0.2 T and to a reduced power consumption of 0.6 MW. We note that the Nomad experiment provided excellent measurements of neutrino interactions with a field of 0.4 T,

| | |
|---|---|
| Magnetic field | 0.2 T (maximum field 0.67 T) |
| External dimensions | 7.6 m(L), 6.1 m(H), 5.6 m(W) |
| Internal dimensions | 7.0 m(L), 3.6 m(H), 3.5 m(W) |
| | (Inner volume $\sim 88m^3$) |
| Iron yoke weight (16 C) | 850 tons |
| Coils material | Aluminum |
| Number of turns | 208 |
| Number of double pancakes | 26 |
| Total conductor weight | 31 tons |
| Ohmic resistance (at T = $40^0$ C) | 0.0576 $\Omega$ |
| Inductance | 0.36 H |
| Nominal current | 3000 A (for B = 0.2 T) |
| Power dissipation | 0.6 MW (for B= 0.2 T) |
| Cooling water flow in coils ($\Delta T = 10^0 C$) | 15 liter/sec |

Table 3.1: Specification of the magnet.

in a neutrino beam with average energy of 30 GeV, i.e. 40 times higher than for T2K.

The Nomad Collaboration, whose help for the use of the magnet we would like to acknowledge, has also provided us a program to compute the field map. It turns out that the field is quite uniform in intensity and direction. Transverse components larger than $1\%$, as well as variations of intensity exceeding $2\%$, are only present in regions at distances of few tens of centimeter from the coils. A more detailed description of the magnet is given in the following, starting with a list of relevant parameters presented in Table 3.1.

The 16 C's forming the yoke have all a very similar structure. Figure 3.5 shows that the C is segmented in 12 azimuthal sections. Each section is made of 16 iron plates 5 cm thick, with 1.7 cm air gap between plates. Apart from the corners, the plates at different depth have the same size. Their dimensions are $0.88 \times 0.90\mathrm{m}^2$ (vertical plates) or $0.88 \times 0.70\mathrm{m}^2$ (horizontal plates). In the UA1 experiment the gaps between plates were instrumented with scintillators and the iron yoke acted as hadron calorimeter. We plan to put scintillators in the gaps to identify laterally escaping muons and to measure their range (Side Muon Range Detector). This is described in Chapter 8.

The coils are made by aluminum bars with $5.45 \times 5.45\mathrm{cm}^2$ square cross-section, with a central 23 mm diameter bore. Demineralised water is pumped through the inner cavity of the conductor to provide cooling. The coils are composed by individual "pancakes" which will be connected hydraulically in parallel and electrically in series. The total thickness of the coils is 20 cm.

### 3.4.2 Installation

The magnet will be installed in the experimental area onto the original supporting structure, as schematically shown in Figure 3.4. The two halves of the magnet (8 C per side) will be mounted onto iron beams, parallel to the beam direction. Two groups of coils will be fixed inside each half of the yoke. The beams are mounted onto carriages which allow to move apart the two halves along rails orthogonal to the beam direction. The movement will be controlled by separate motors on the two sides. It will be possible to move the two halves apart by 5.5 meters, so to guarantee easy access for the assembling of the inner detector (the maximum transverse dimension of the

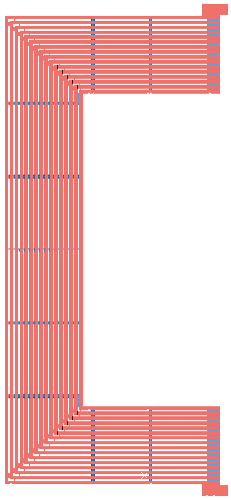

Figure 3.5: Lateral view of one of the 16 C's composing the iron yoke.

inner detector is 3.5 meters).

For the assembling of the inner detector inside the magnet, we plan to adopt a technique similar to that of the NOMAD experiment, but to use a newly designed framework, adapted to our detector. With the possible exception of the electromagnetic calorimeter (which could be divided in two halves and fixed to the iron yokes), all other detectors will be assembled inside a metallic frame ("basket") with approximate dimensions of $6.5 \times 2.6 \times 2.5\mathrm{m}^3$. A preliminary design of the basket with its supporting structure is shown in Figure 3.6. The basket will be completely open at the top, to allow the insertion of the various detectors. Two short beams will be fixed at the center of the two faces of the basket perpendicular to the beam axis. The short beams will be connected outside the magnet to a structure fixed on the floor, which holds the basket. The beams will connect the basket to the external support structure passing through the holes in the coils , originally designed to allow the passage of the beam pipe. When opening the magnet, the C's and the coils move apart, while the basket and the inner detector remain in the position chosen for data taking. The design and construction of the basket and of the supporting structures, can be accomplished in less than one year. Therefore, we shall wait for the final engineering design of the inner detectors before to finalize the design of these structures.

Most of the magnet components are in good conditions and stored at CERN. These are the 16 C of the iron yoke, the coils, support carriages and rails, and manifold for the distribution of the water cooling. We foresee to perform at CERN a complete check and maintenance of these components (including a test of coils insulation). The maintenance will be completed by the end of 2006. The motors for the displacement of the magnet are not available anymore. We will design a new system for movement and buy new motors. The magnet will be shipped to Japan, most likely in the second half of year 2007. The design of the framework allowing the installations of the detectors inside the magnet is now under study. The installation of the magnet in the pit will be performed during spring 2008, before the construction of the roof of the experimental hall. The weight of a single C (53 tons) is in fact larger than the capacity (10 tons) of the crane in the experimental hall. Therefore, the rails, carriages, yoke and coils will be lowered in the pit by using external cranes and the installation of the magnet will be completed. We will then proceed to the

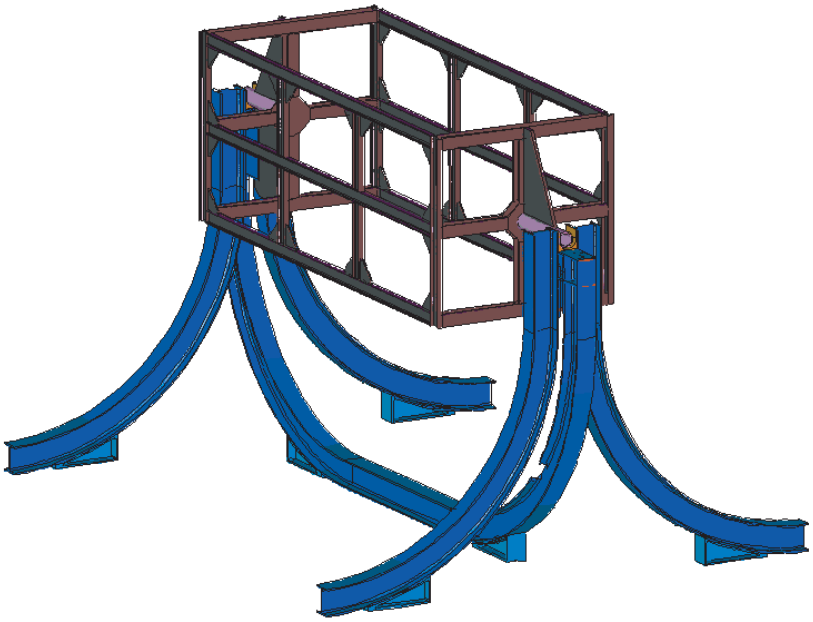

Figure 3.6: Preliminary drawing of the basket.

coverage of the hall with its roof, before starting to install the detectors inside the magnet.

# Chapter 4

# Neutrino Monitors

In the T2K experiment, there are two detector systems designed specifically for online neutrino beam monitoring: One is a muon monitor and the other is an on-axis neutrino detector. The neutrino monitors will be used to measure and monitor the neutrino beam properties: the direction, profile, time structure, intensity, and, if possible, energy spectrum of neutrinos. The muon monitor and the on-axis neutrino detector are complementary to each other as described below.

## 4.1 Muon Monitors

As discussed in Section 2.3, the muon monitor (MUMON) will be placed downstream of the beam dump and will monitor the intensity, profile and direction of the beam by detecting high energy muons. MUMON is sensitive to the proton hit position at the target and the status of the target and horns. Therefore, it is also used as a proton beam monitor, a target monitor, and a horn monitor. The measurements of MUMON will guarantee the quality of the neutrino beam on a spill by spill basis. In addition, MUMON will be an essential equipment to tune the neutrino beam directed to the Super-Kamiokande at the beginning of the experiment. In this section, its requirement and baseline design are described.

### 4.1.1 Specifications

In order to identify the specifications of MUMON, a GEANT-3 based MC simulation is carried out. The sensitivity of the muon profile at MUMON to the proton beam position at the target is studied. Since the magnetic horn system works as a lens to charged particles and magnifies the beam displacements from the target center, the MUMON has a good sensitivity to the proton beam position at the target. The displacement of the proton beam at the target can change the direction of the neutrino beam, which affects the neutrino energy spectrum at Super-Kamiokande, since the off-axis angle changes. From a study of the horn alignment and the proton beam displacement [25], the proton beam position at the target should be monitored and controlled with a precision better than 1 mm in order to guarantee the neutrino energy spectrum at Super-Kamiokande. In addition, the safety of the target and horn avoiding the unforeseen radiation heat load by the displacement also requires the proton beam position to be monitored within 1 mm precision.

The muon momentum dependence of the magnification factor is studied. The muon beam center before the beam dump as a function of the proton beam position is shown at the left plot in Figure 4.1. Ten million protons on target are simulated. Red circle, green rectangle, blue (open) triangle, purple (filled) triangle, black inverted triangle correspond to a muon momentum threshold

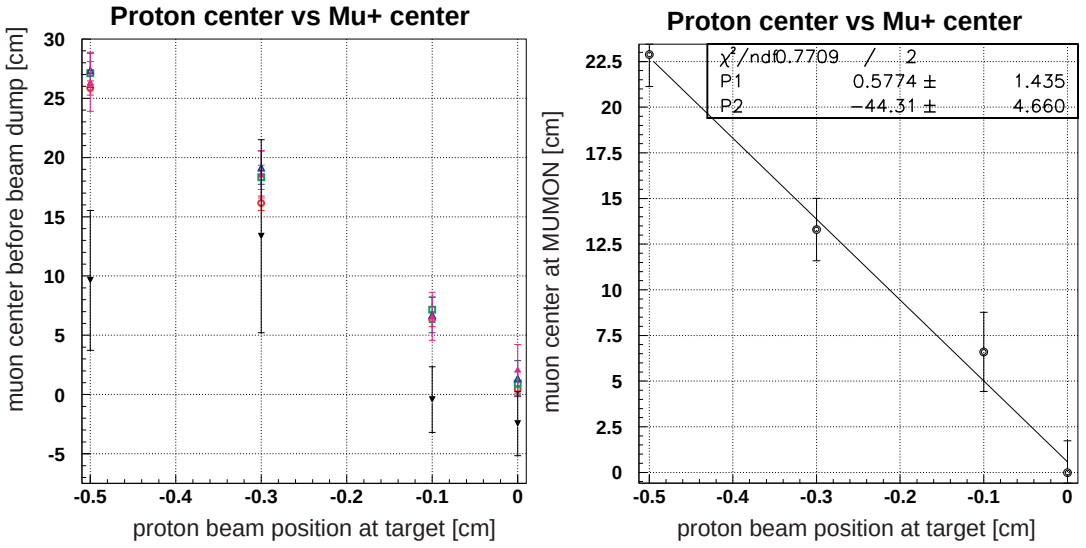


Figure 4.1: Muon beam center as a function of the proton beam position. (Left) Muon beam center before the beam dump with different muon momentum thresholds: Red circle for 3 GeV/c, green rectangle for 4 GeV/c, blue (open) triangle for 4.5 GeV/c, purple (filled) triangle for 5 GeV/c, black inverted triangle for 6 GeV/c. (Right) Muon beam center at the MUMON position with the realistic design of the beam dump.

of 3, 4, 4.5, 5, and 6 GeV/c, respectively. No difference is observed with a threshold of 5 GeV/c or below, while the magnification factor becomes smaller with 6 GeV/c threshold because high momentum muons have less sensitivity to the magnetic field. On the other hand, both the radiation and background levels become higher with the lower muon momentum threshold without gain of the magnification factor. We chose 5 GeV/c as the muon momentum threshold for MUMON.

The MC study is also used to define the transverse dimensions required for MUMON. Figure 4.2 shows the muon profile at MUMON when the proton beam position at the target is displaced in horizontal direction by 1 mm, 3 mm, and 5 mm. In this study, the geometry of the beam dump was implemented as 2.2 m-thick graphite, 1.35 m copper, 1.35 m iron and 1 m of concrete. The thickness of the beam dump corresponds to the muon momentum threshold of 5 $\mathrm{GeV}/c$. The profile in a 2 m $\times$ 2 m area is projected onto the horizontal axis with 5 cm bin. The change in the muon beam direction which is proportional to the proton beam displacement is clearly seen. In order to measure the proton beam position displacement up to 5 mm, the MUMON should cover an area of 1.6 m $\times$ 1.6 m around the designed beam center. The muon center at MUMON as a function of proton beam position is shown at the right plot in Figure 4.1. The center of the muon beam is measured by fitting the muon profile in $\pm 50$ cm around the peak position with a Gaussian. The magnification factor is 44.

### 4.1.2 Baseline design

Based on the experience in K2K, we chose a combination of a segmented ionization chamber and an array of the semiconductor detectors as the baseline design of the T2K muon monitor.

The ionization chamber is a simple and reliable device to monitor the beam for a long run period. It is also suitable to cover the large area of the beam profile with the large number of

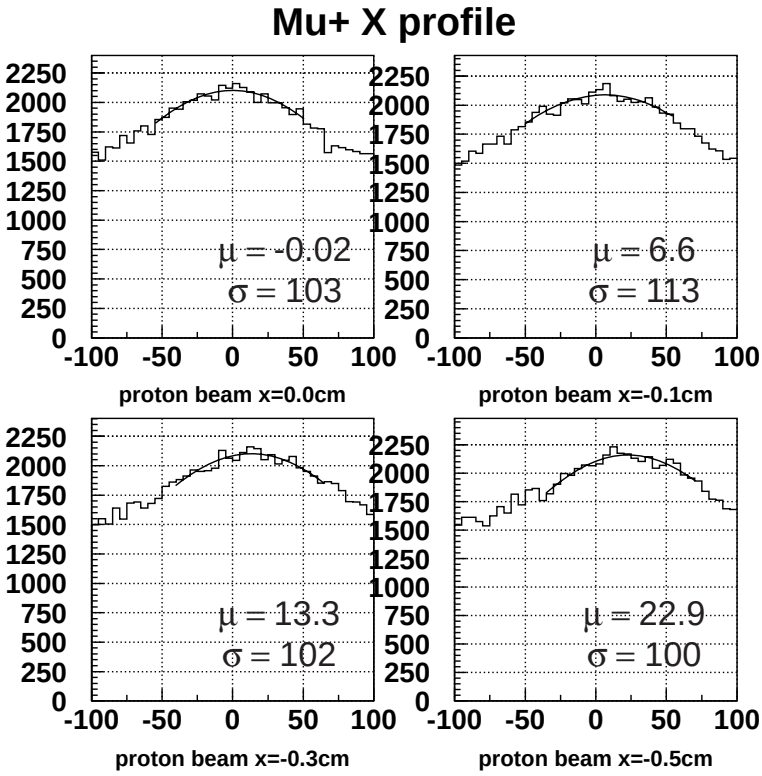


Figure 4.2: Muon profile at the MUMON position when the proton beam position at the target is nominal position (top left), displaced by 1 mm (top right), 3 mm (bottom left) and 5 mm (bottom right).

devices. Some weak points are the slow response and the non-strong signal over the unknown backgrounds after the beam dump. Because of the slow response, it is not adequate to monitor the bunch structure of the beam inside of the spill, which might give useful information for the beam tuning. Some of the expected backgrounds are the signals generated by neutrons and by ionization of charged particles passing through the cables and connectors.

The semiconductor detector has a fast response, and is less sensitive to background because of the large and fast signal. Since the semiconductor detector is not inexpensive, the number of device to cover the area of the beam profile will be limited. In addition, a concern for the semiconductor detector is the long term stability due to the radiation damage.

We design to construct two detector planes with different sampling intervals: one consisting of the ionization chambers and the other of the semiconductor detectors. Two independent and complementary detectors provide reliable monitor information that is mandatory for the experiment. The MUMON signals will be recorded by the FADC modules commonly used for the T2K beam-line monitor developed at KEK. The MUMON data will be also processed by the beam-line DAQ.

The design and status of detector R&D for each detector system are described in the following.

**Segmented ion chamber**

Ionization chambers are widely used for measurements in high radiation environment. For example, plate ionization chambers are used to monitor hadron and muon beam properties in NuMI beamline at FNAL [26], where the expected number of particles is similar to T2K beamline. The R&D work for the technical design of the detector is going to start in JFY2005, with prototype construction based on the NuMI muon monitor design. The proto-type chamber is $10 \times 10\mathrm{cm}^2$ and 3 mm gap by using He gas. Although the final design of the chamber plane is not fixed yet, we will use roughly $10 \times 10$ chambers to cover the $1.6 \times 1.6\mathrm{m}^2$ area.

A beam test of the proto-type chamber with an electron beam at Kyoto University is under preparation. The simulation study also continues to identify more detailed specifications, such as the optimum segmentation and the estimation of hadronic background.

**Semiconductor detector**

Semiconductor detectors with an active area of order $1 \times 1\mathrm{cm}^2$ will be arranged in an array to cover the MUMON area of $1.6 \times 1.6\mathrm{m}^2$. The arrangement and the necessary number of detectors are a subject of future study, but one possibility is to arrange them along horizontal, vertical and $45^\circ$ slanted axes, as done in the K2K muon monitor.

Based on the MC simulation, the expected muon flux at the center of MUMON is about $10^8$/cm$^2$/spill. This corresponds to $\mathcal{O}(10^{15})$ muons/cm$^2$ for one year of operation with full intensity. The silicon detectors, which were used for K2K muon monitor system, may not work with this amount of particle fluence because of radiation damage. Currently a diamond detector which is an another type of the semiconductor detector with higher radiation tolerance, is studied as a candidate detector for the T2K MUMON. The diamond detector is extensively studied and developed by RD42 collaboration at CERN [27], with a goal of using it for the inner tracker in LHC experiments. Some concerns on the diamond detector is the expensive price ($> \$1,000$ for one detector) and the capability of the mass production, which must be cleared with R&D.

In JFY2003, a diamond detector with $1 \times 1$ cm$^2$ dimension fabricated by RD42 collaboration was installed in the K2K muon monitor to study the basic property. Signal was successfully

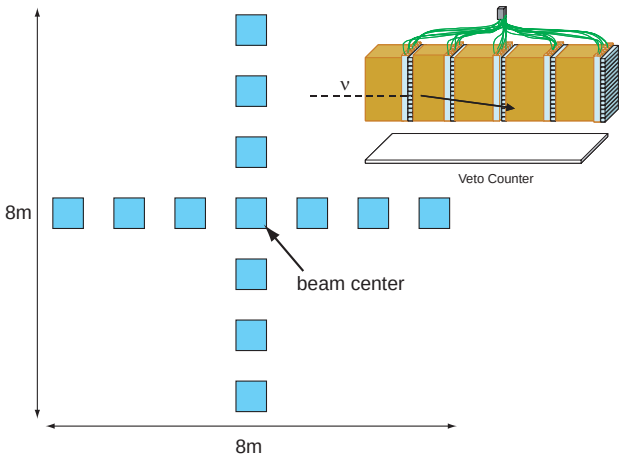


Figure 4.3: The arrangement of N-GRID detectors at the near detector hall.

observed with the K2K beam, but there still exist many issues to be checked before we can use it as MUMON. A beam test is planned in JFY2005 with an electron beam at Kyoto University to study the response of diamond detectors to the expected level of particle flux. Five pieces of diamond detector are available in Japan. We need separate tests to confirm the radiation hardness and stability of the detector. Also, the radiation hardness of silicon detectors in the anticipated environment will be tested.

## 4.2 On-Axis detector (N-GRID)

### 4.2.1 The N-GRID design, performance and proto-type

The neutrino detector at on-axis is one of key elements to monitor the neutrino beam in T2K. The on-axis detector will monitor the neutrino beam directly with neutrinos. It is sensitive to the neutrinos of the whole energy range, although MUMON is only sensitive to the high energy neutrinos because of the high muon momentum threshold. The detector will also guarantee the direction of the neutrinos once the beam is tuned by MUMON. The detector will monitor the beam properties on a day by day basis.

The N-GRID detector is designed to consist of $7 + 7$ (or $5 + 5$) identical units, arranged to form a grid which samples the beam on $8 \times 8\mathrm{m}^2$ ($\pm 4\mathrm{m} \times \pm 4\mathrm{m}$) area, as shown in Figure 4.3. The design of one unit which was made as a proto-type is shown in Figure 4.4. For N-GRID, the target of neutrino interaction is iron, and the scintillators are used to detect a muon from the interaction.

The neutrino beam profiles at the experimental hall are shown in Figure 4.5 for neutrinos with energy below 1 GeV, from 1 to 2 GeV, from 2 to 3 GeV, and above 3 GeV. The neutrino events in N-GRID will be identified by requiring the number of hits of the successive tracker counters greater than two and no hits of the veto counters. The contamination of background by neutrinos interacted outside of N-GRID is expected to be a few percent level. By reconstructing neutrino events, the beam profile is measured as shown in Figure 4.6 with five N-GRID detectors. The beam center is measured with the precision of 5 cm. The direction of the neutrino beam is defined as a vector from the proton target to the center of the neutrino beam profile. With the N-GRID detectors, the pointing accuracy of the neutrino beam is achieved to be $0.18$ mrad, which is satisfied

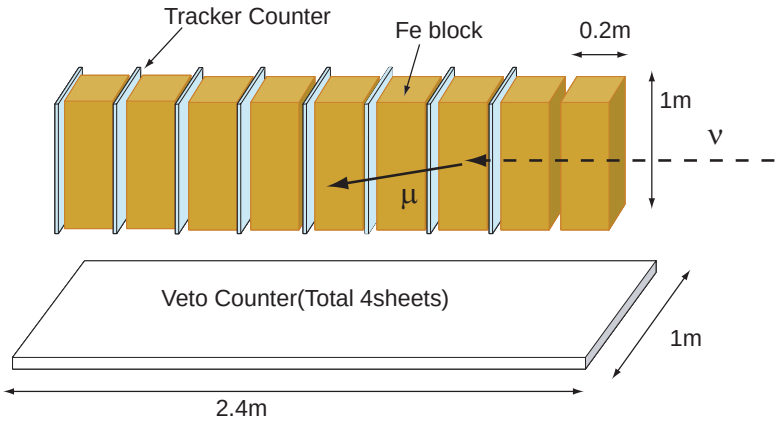


Figure 4.4: The drawing of the N-GRID proto-type detector tested in the K2K experiment. The thickness of the iron block is 20 cm in the proto-type. The thickness of the real detector will be changed and optimized for the T2K beam.

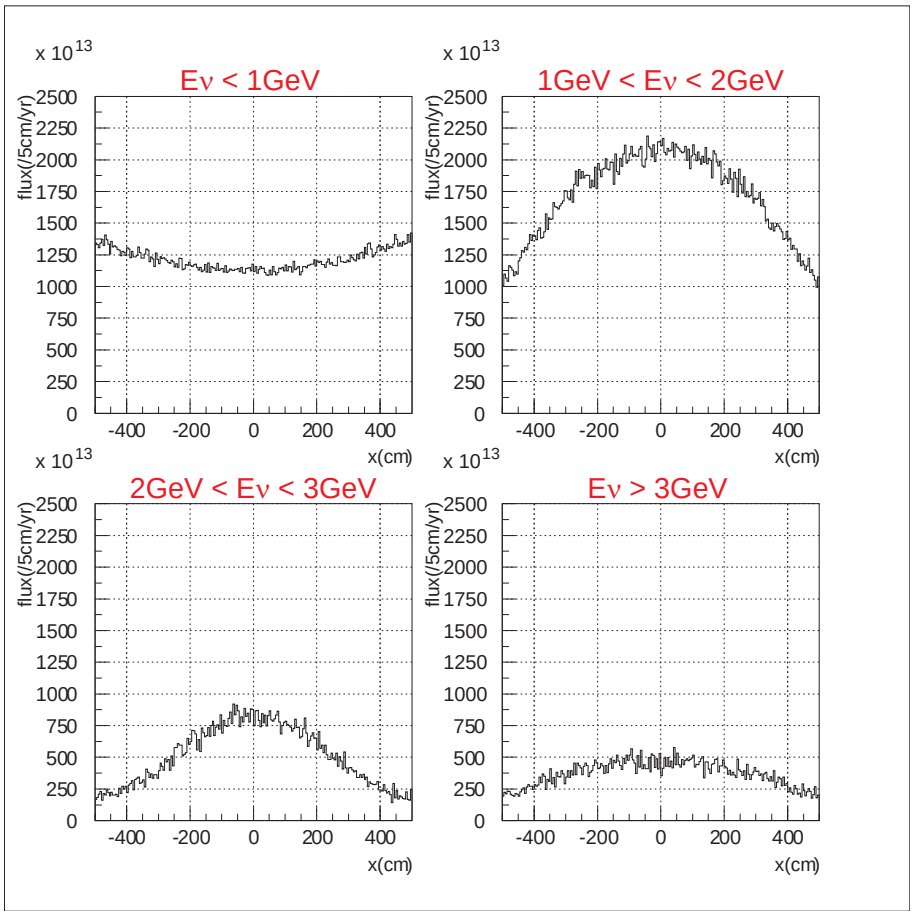


Figure 4.5: The neutrino beam profile at the near detector hall for neutrinos with energy below 1 GeV, from 1 to 2 GeV, from 2 to 3 GeV, and above 3 GeV.

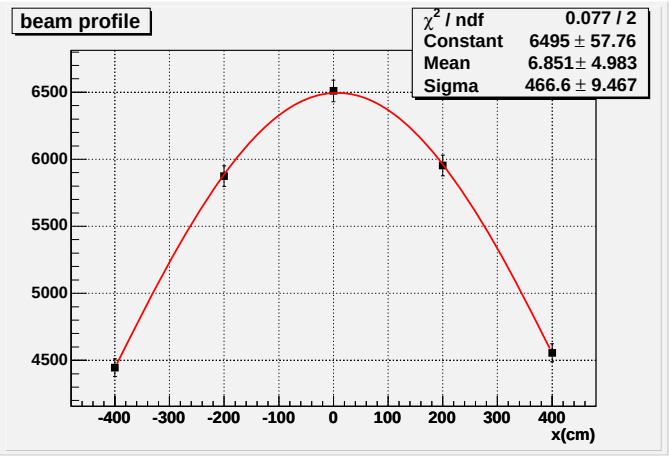


Figure 4.6: The neutrino beam profile measured with the N-GRID detectors.

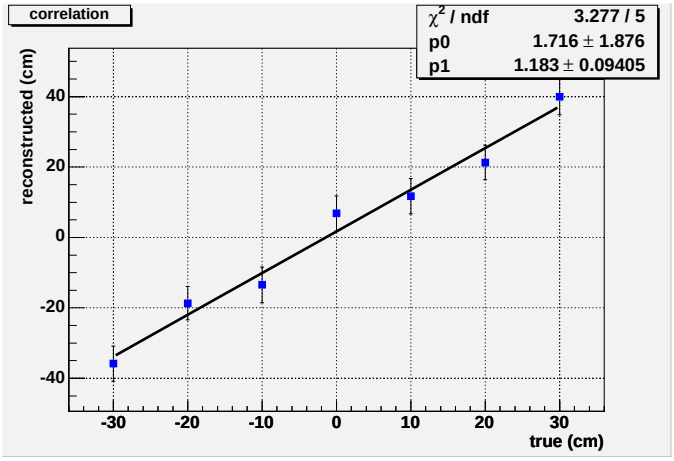


Figure 4.7: The reconstructed beam center as a function of the true beam center.

with the experimental requirement of 1 mrad.

The sensitivity to the change of the beam center is studied by reconstructing the center of the neutrino events where the true beam center is moved. The result is shown in Figure 4.7, and a good linear relation is found.

The total number of neutrino events observed by N-GRID is more than 10,000 $\mathrm{events/day}$ with the $\sim$ 10 tons mass of the N-GRID detector. With this statistics, we monitor the neutrino beam with better than 1 % accuracy day by day.

The concept of N-GRID is satisfied with the experimental requirement in the Monte Carlo simulation. In order to prove the concept under the real condition, the first proto-type detector was built as shown in Figure 4.4 and installed in K2K. However, because of the early termination of K2K due to a broken horn, we could not collect useful data for the analysis. A second proto-type detector is under design with segmented tracker counters to reconstruct the muon track in the neutrino interaction.

For future R&D work, the detector design should be optimized to keep high efficiency for

neutrinos, to suppress the background, and to collect as many events as possible with the moderate size and mass of the detector. Currently the study of the detector design is under way to fix the total depth of iron for the muon momentum threshold and the thickness of each iron block for the tracking capability.

### 4.2.2 Scintillation counter for N-GRID

We plan to use the extruded scintillator read by the wave-length-shifting (WLS) fibers. One type of the extruded scintillator is the K2K-SciBar scintillator produced at Fermilab [47]. This extruded scintillator is described in Section 5.2.1. We will use this scintillator for the tracker planes of N-GRID. One tracking plane will consists of two layers: one for horizontal and the other for vertical segmentations. One tracking plane will consists of twenty $10 \times 10 \times 1000 \mathrm{cm}^3$ scintillator counters. We will have ten or more tracking planes per module. Each counter will be readout by SiPM which is described in the Section 5.2.4. We will record the charge and timing information.

In addition, we also cover the outside of module by the veto counters as shown in Figure 4.4. Another type of the extruded scintillator for this purpose is developed at the Uniplast Factory at Vladimir in Russia. The scintillator provides the 80% light yield of Bicron BC408. Transparency is homogeneous in all directions, and the light attenuation length was measured to be about 30 cm in a 5 mm thick scintillator. As a reflection coating, the scintillator is etched by a chemical agent that produces a micropore deposit over the plastic surface. An advantage of this approach over the commonly used white diffuse papers is an almost ideal contact of the reflector with the scintillator. After etching a scintillator, the grooves are made on the surface. The scintillating light is transported to a photosensor using the wave-length-shifting (WLS) fibers glued in the grooves. The thickness of the extruded slabs can be in the range 5-10 mm. Details can be found in Refs. [28, 29, 30]

Two counters were manufactured for tests as a veto counter of N-GRID . The dimensions of the counter are 10 mm thick, 170 mm wide and 2100 mm long. The width of grooves is 1.15 mm and depth is 2 mm. The Kuraray Y11 double-clad WLS fibers of 1 mm diameter are glued in the grooves. One counter has spacing between groves of 10 mm, and another 20 mm. Both ends of the fibers are collected in a bunch and fixed in a holder to provide good contact with a PMT. The counters are shown in Fig. 4.8.

The two counters were tested with cosmic rays. The light yield is measured as shown in Fig. 4.9. With the light yield, the 99.95% efficiency for a MIP particle ($\epsilon_{MIP}$) is obtained with 10 mm spacing by taking the OR of double side hits, and $\epsilon_{MIP} = 99.89\%$ with 20 mm spacing. These results are preliminary and the measurements are under way.

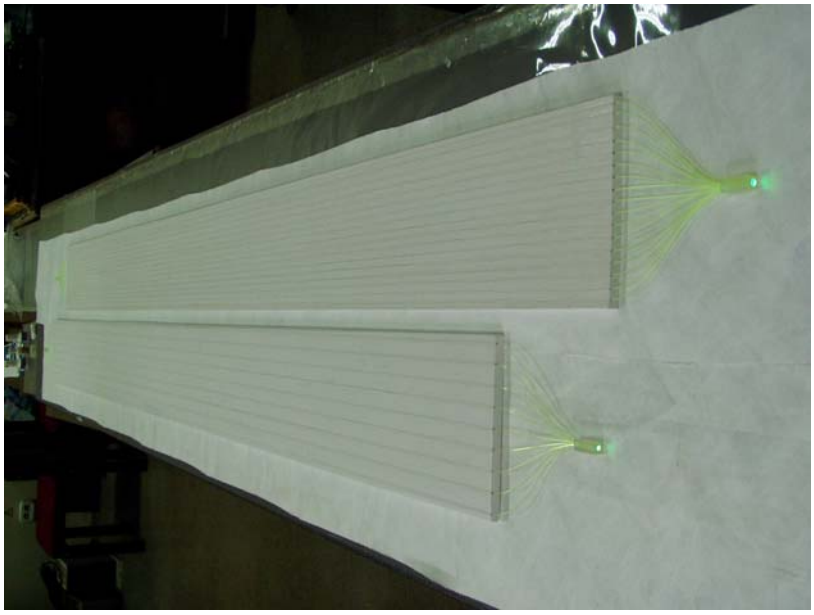

Figure 4.8: Two scintillation counters with embedded fibers covered by the reflector. The bottom detector has 20 mm spacing between fibers, the top is 10 mm spacing.

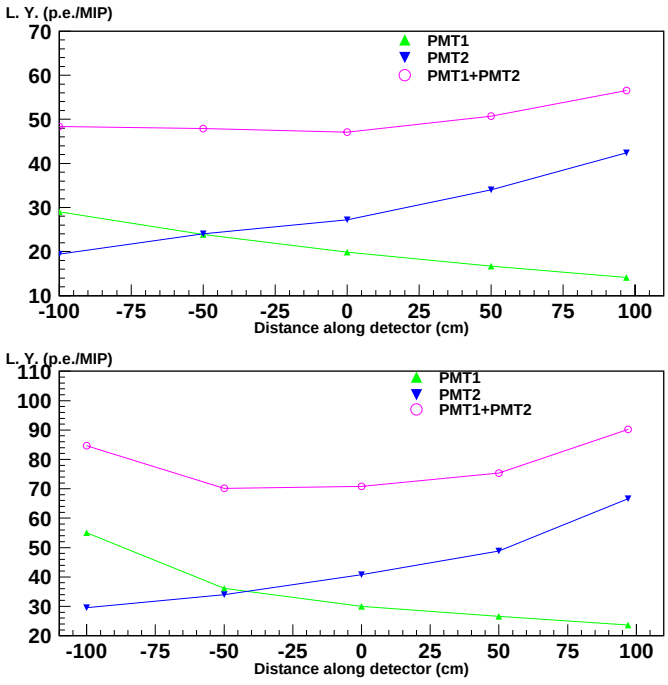


Figure 4.9: Light yield as a function of the hit position along the counter. PMT1 and PMT2 show light yield of the detector with the 20 mm spacing groves, and PMT3 and PMT4 with the 10 mm spacing.

# Chapter 5

# Tracker (FGD+TPC)

## 5.1 TPC

### 5.1.1 Introduction

The primary purpose of the TPC modules is to measure the 3-momenta of muons produced in quasi-elastic charged current neutrino interactions in the FGD, thereby providing the most accurate estimate of the neutrino spectrum. At the peak of the neutrino spectrum in the near detector, approximately 750 MeV, the neutrino energy resolution is limited to about 10% due to Fermi motion within the struck nuclei. In order to reach this fundamental limit in the neutrino energy determination, the momentum resolution of the TPC should be better than 10% for muons with momenta below 1 GeV/c. The charge of the products from neutrino interactions must also be determined unambiguously, in order to distinguish the charge of pions produced in inelastic events and to determine the anti-neutrino component in the beam. This will be the most challenging for high energy neutrinos, primarily arising from kaon decays. Given the limited curvature of tracks in the relatively weak magnetic field in which the TPC will operate (0.2 T), good space point resolution will be needed to meet these goals.

Good measurements of the ionization energy loss will be useful to help distinguish electrons and protons from muons and pions. It will also be important to distinguish the products from neutrino interactions inside the fiducial volume of the near detector from other beam related activity. In particular, neutrino interactions in the magnet iron will produce many charged particles that will enter the fiducial volume. The excellent 3D granularity of TPCs will allow these to be distinguished more easily than in a projective 2D tracker.

A large fraction of low energy neutrino-nucleus interactions involves the production of very low energy hadrons. Monte Carlo simulations of these processes make use of empirical models which have not been well tested, owing to the fact that it is difficult to detect and measure the low energy particles within dense target material. The gas of the TPC will provide additional target nuclei, and neutrino interactions within the gas could provide interesting samples of a few thousand events per year to improve the understanding of neutrino-nucleus interactions, since all of the charged particles produced can be tracked in the TPC.

Several identical TPC modules in the shape of rectangular boxes are to be constructed for the near detector. The remainder of this section describes the conceptual design of these modules which has evolved from earlier documents [31, 32]. The outer dimensions of each module are assumed to be approximately 2.5 m $\times$ 2.5 m in the plane perpendicular to the neutrino beam direction, and 0.9 m along the beam direction. The transverse dimension is chosen to provide

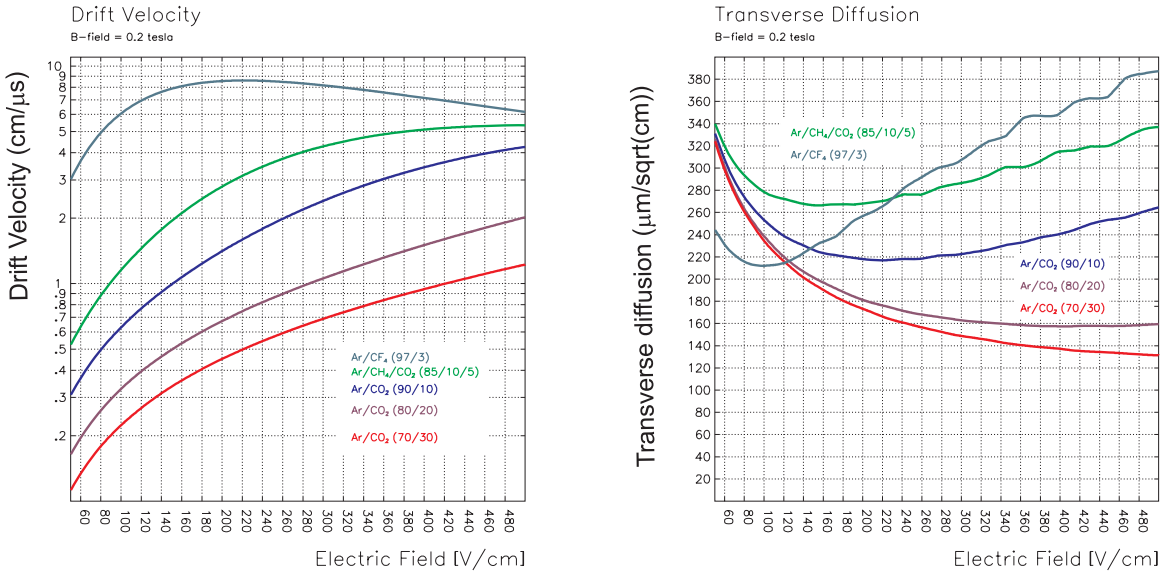


Figure 5.1: Properties of some candidate gas mixtures in a 0.2 T magnetic field. On the left the drift velocity is shown (cm/$\mu$s) vs. drift field. On the right the transverse diffusion ($\mu$m/$\sqrt{\text{cm}}$) is shown vs. drift field. The longitudinal diffusion is similar to the transverse diffusion.

space between the inner wall of the magnet and the TPC modules for electromagnetic calorimeter and for a mechanical support cage. The dimension along the beam direction is chosen to achieve the required momentum resolution, including the necessary inactive elements. The outer skin of TPC module will be at nominal ground potential for safety considerations and for RF shielding.

### 5.1.2 Gas choice

The primary requirement of the TPC is to provide many accurate space points along the length of the tracks. Diffusion of the drifting electrons can be a limiting factor in the intrinsic space point resolution of a TPC. A simple upper bound on the diffusion can be calculated using the standard Gluckstern parameterization, assuming a large number of measurements along the length of the track,

$$D < \frac{\sigma_{p_t}}{p_t}\sqrt{\frac{n_T L}{720}}(L[m])^2\frac{0.3B[T]}{p_t[GeV/c]}\frac{1}{\sqrt{L_{\text{drift}}}} = 260\ \mu\text{m}/\sqrt{\text{cm}}, \tag{5.1}$$

by demanding that the diffusion component of the momentum resolution is less than 5% at $p_t$ = 1 GeV/c, and assuming $n_T = 90$ ionization electrons per cm of gas (argon) for a track measured over $L = 60$ cm after drifting for a distance, $L_{\text{drift}} = 125$ cm. This bound should be taken as a rough guideline as additional effects can further degrade the resolution and it is not common for a TPC to reach the diffusion limit.

Gas components under consideration include Argon, Neon, $CO_2$ methane, iso-butane, and $CF_4$. A candidate for the T2K TPC gas mixture is Ar $CO_2$ (90:10). At a drift field of 200 V/cm, the transverse diffusion is approximately 220 $\mu$m/$\sqrt{\text{cm}}$ and the drift velocity is 14 mm/$\mu$s. The properties of Ar $CO_2$ gas mixtures for other proportions and other mixtures are shown in Figure 5.1.

Higher concentrations of $CO_2$, 20-30%, reduce the diffusion constant further, in the range of 150 $\mu\mathrm{m}/\sqrt{\mathrm{cm}}$ although this requires higher drift fields, up to approximately 400 V/cm. A significant complication associated with $CO_2$ is that it enhances electron attachment by oxygen in the drift volume. For 10% $CO_2$ operated at 200 V/cm, the $O_2$ contamination would need to be kept to below around 10 ppm, which is typically achieved in large drift chambers. Very large concentrations of $CO_2$ are disfavored as they set challenging requirements, typically below 1 ppm, on the $O_2$ contamination.

Ar $CF_4$ (97:3) is another possible gas candidate. It is very fast, but saturates near 200 V/cm, and therefore is more stable against gas density fluctuations.

Neon has the advantages of more closely resembling the oxygen as target nuclei and having a larger radiation length. It is more costly, however, and the ionization statistics are lower. Aging produced by hydrocarbon quenchers should be less of a concern for the T2K environment: therefore the use of these gases can be envisaged.

Given the above considerations, the TPC field cage and gas vessel will be designed to work at a nominal drift field of about 200 V/cm, but also be capable of operation at up to 400 V/cm. Significant attention will be given in the design to reduce atmospheric contamination of the drift gas.

### 5.1.3 Field cage and gas containment

To operate the TPC at drift fields up to 400 V/cm with a maximum drift length of 1.25 m, the central cathode potential will be at most 50 kV, half the design potential of the ALICE TPC cathode. In order to limit the development time for the TPC field cage and gas containment vessel, the designs of existing TPCs were considered in detail, in particular those of ALEPH, NA49, STAR, and ALICE. A preliminary T2K TPC design concept that most resembles the STAR design has been chosen, in order to achieve a very uniform drift field without high surface fields and whose structure is rigid and relatively easy to construct.

Like the ALICE TPC, the T2K TPC field cage volume and endplates are surrounded by a separate $CO_2$ gas envelope, to provide safe insulation between the central cathode and the outer wall of the TPC, and to reduce contamination from $O_2$, $N_2$ and water from the atmosphere into the drift volume. The gas gap is 75 mm thick, one half of the ALICE design. The walls of the inner and outer gas volumes are made of composite material, with a rohacell core and thin copper clad G10 skins. The walls, about 20 mm thick, are constructed as flat panels and then assembled into rectangular box structures, with tongue-in-groove and glue joints. The central cathode will also be constructed by the same technique, and will be positioned and held in grooves cut into the field cage walls. Perforations or gaps around the edge will allow gas to mix on both sides of the cathode.

The inner and outer surfaces of the outer gas containment vessel will be at nominal ground potential. Prior to constructing the field cage box, its walls will have grooves cut along the length on both sides, using a precision router, to form the drift field defining strips. Extensive electrostatic computations of this design as well as the STAR, ALICE, and other TPC designs were performed [34] using the finite element analysis software FEMLAB [35]. Based on these concepts, within engineering constraints and with the goal of optimizing the field uniformity in the drift volume, the principal design, the strip width, the gap between the strips, the alignment of the strips, and the thickness of the inner wall were optimized. The computations were carried out in two dimensions using a full model of a TPC module, including the plates at the ends of the drift volumes, and the inside of the outer containment vessel. The proposed concept, shown in

Figure 5.2, closely follows the STAR field cage. The design parameters are:

- The field forming strips are defined by grooves on both sides of the inner wall. The strips are $10\,\mathrm{mm}$ wide and the grooves are $1.5\,\mathrm{mm}$ wide, giving a pitch of $11.5\,\mathrm{mm}$. The parameters were chosen as small as practical. The narrow gap reduces the field distortions in the drift volume.

- The strips on the outside and inside of the wall are aligned.

- The inside of the outer gas containment vessel is held at ground. The potential of the drift field drops to ground across the gas envelope.

- The drift field is terminated at the endplate by a wire grid. This reduces distortions in the drift volume arising from non-uniformities in the gas-amplification section.

- The central cathode and the wire grids on either side are aligned with the middle of the respective strips. This design was found to minimize field distortions in these corners.

Along the drift direction the field is found to be uniform to better than $10^{-4}$ for distances larger than $2\,\mathrm{cm}$ from the wall. Along the central cathode the drift field becomes uniform to better than $10^{-4}$ for distances larger than $1\,\mathrm{cm}$.

A separate issue is high surface fields that may cause discharges. The fields become largest in the immediate vicinity at ends of the strips on the outside of the inner wall. The fields were found to be smaller than $18\,\mathrm{kV/cm}$ for the proposed concept. Note also, that the present pitch and strip width is identical to the STAR TPC.

The results shown here do not address the accumulation of surface charges on the inner wall between the field forming strips. If large enough, these charges give rise to field distortions. While preliminary studies suggest that the proposed field cage concept is similarly insensitive to surface charge accumulations as a more elaborate design by the TESLA collaboration [36], the impact of surface charges is poorly understood. Note, also, that it is thought that the small gap width and the receded gap surface help reduce their impact [37].

The ALICE voltage divider network uses relatively low resistance (1 MΩ) between strips, because of the large reverse current from positive ions in the gas volume. This is much less of an issue for the T2K TPC, and therefore higher resistances should be used, possibly 10 MΩ, reducing the heating load. Pairs of 20 MΩ good tolerance metal-oxide resistors should be used to reduce the possibility of developing an open circuit in the divider chain. The resistor divider network will be placed in the gas envelope, and a slightly larger gap will be used at that end. Likewise, the same area can be used to carry the HV cable to the central cathode. The end of the resistor divider chain, connected to the final strip and wire grid, should drain through an external resistance to ground and its potential should be defined through an additional supply, in order that it can be matched to the operating voltages of the gas amplification section.

### 5.1.4 Gas system

A recirculation system will need to be put in place to maintain oxygen contamination at the level of 10 ppm or lower. The ALICE TPC expects to flow its inner and outer gas volumes at approximately one volume change every 5 hours. The ALICE outer volume, itself more than twice the volume of a T2K TPC module, has a gas circuit with no recirculation; only fresh gas is injected. The systems for the inner gas volume (drift volume) and the outer gas volume (flush gap) will be separately

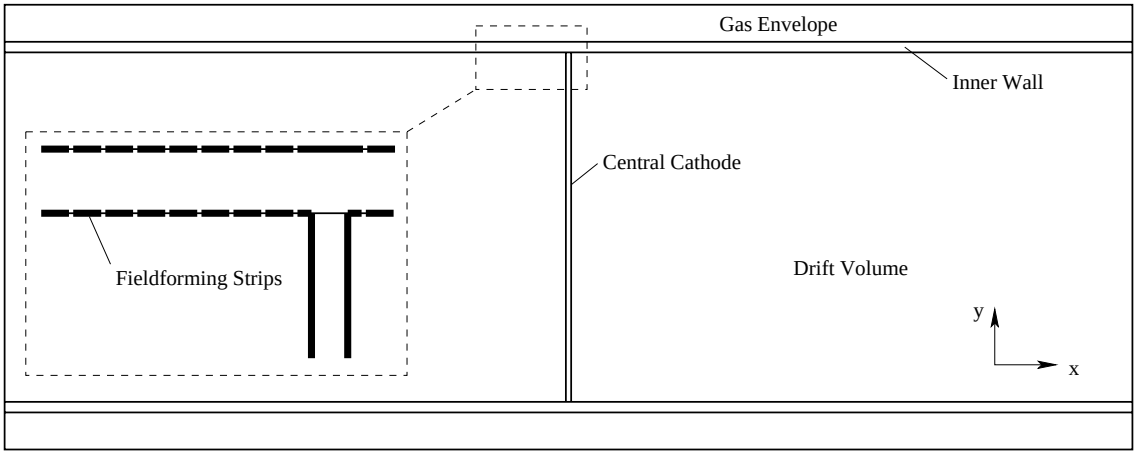


Figure 5.2: The 2-dimensional model used in the finite element analysis. The model is 2129 mm long and 842 mm wide. It ends at the endplates at ground potential (left and right in the figure) and at the inside of the outer wall also at ground. The inset shows a detail illustrating the arrangement of the field forming strips.

operated. Ar and $CO_2$ for the main volume are provided, respectively, from cylinders and from a gas tank both located at ground level. They are mixed and stored in a buffer tank, and go through the gas purifier and filter system to remove contaminant oxygen, water, and particulate. After that it enters each drift volume, gas goes from one side, through holes in the central cathode, and exits the other side of the volume. The exhaust from the chamber is collected in a chamber exhaust manifold and then returned to the buffer tank to be recirculated. The flow rate will be 20 $l$/min for each drift volume, and hence 60 $l$/min in total. $CO_2$ for the outer volume is directly sent from a gas tank to flush the outer volume. Exhaust is collected into a flush gap exhaust manifold and then pumped up to ground level and exhausted to the atmosphere. The flow rate for the outer volume will be 30 $l$/min in total.

The gas flow rate will be controlled and monitored by mass flow controllers installed at several points. The gas pressure in the inner and outer volumes should be the same pressure as atmosphere to avoid chamber wall distortion, and hence drift field distortion. For this purpose, pressure controllers will be installed between the chamber exhaust manifolds and the flush gap exhaust manifold and also between the flush gap exhaust manifold and the atmosphere.

Oxygen contamination level should be monitored in order to maintain $O_2$ level below 10 ppm. An oxygen monitor which can measure amounts of oxygen in presence of $CO_2$ down to at least 1 ppm will be used. We plan to monitor the oxygen level of the outflowing gas from the gas purifier/filter and of the returning gas to the buffer tank. Given the large flow rate of $CO_2$ gas ($\sim$80 kg/day in the case of 30 $l$/min flow rate) through the flush gap volume, $CO_2$ will be stored in liquid state in a large 5 ton capacity tank. The purity of $CO_2$ is very good from such tanks.

### 5.1.5 Gas amplification

Existing TPCs have been designed to use grids of wires to provide gas amplification at the endplates. Wires require significant tensioning and are prone to breakage. Moreover, the granularity is limited by the nature of the signal generation as sampled by the pads on the endplate. In the

past several years an extensive R&D effort has been underway around the world to improve the performance of TPCs, particularly for its application as a Linear Collider tracker. The most important development has been the demonstration of TPCs that use Gas Electron Multipliers or Micromegas devices instead of wires. These studies have shown significant improvements of resolution capabilities of TPCs. Given the particular success that groups have had with these devices, their relative maturity and benefits over wire grids, the proposed baseline design uses either GEMs or Micromegas for the gas amplification. At this stage, the choice of technology is premature and the remainder of the TPC design does not strongly depend on the system chosen.

GEM foils measuring 30 cm $\times$ 30 cm that follow the design used in the Compass experiment [38] can be used to build readout amplification modules that are joined together into sectors and inserted into the field cage endplate. Three GEM foils are used in each readout module, in order to safely achieve good gas gain of a few thousand. Potential suppliers of large GEM foils include the CERN PCB shop and two private companies, 3M and TechEtch. The GEM foils are placed on thin fibreglass frames, with narrow spacer strips to maintain the gap between neighboring GEM foils.

Similarly, large Micromegas foils could be used to build the readout modules. Today, the largest microchannel devices in operation are the 40 $\times$ 40 cm$^2$ Micromegas modules of Compass [39]. Large surface Micromegas detectors can be realized with a woven mesh (produced for instance by Gantois) of 38 $\mu$m thickness. A promising technique to build these modules is "Micromegas in the bulk" [40], where the mesh is sandwiched between two resistive "Vacrel" layers. This leads to mechanically robust detectors and there is no need of an external frame to hold the mesh. Possible furnishers of these detectors are the CERN PCB shop and the SEDI (Dapnia, Saclay) laboratory.

#### HV considerations

The high voltage system should be designed to reduce the consequences of a single readout module failure. For example, if a single GEM readout module has a HV failure across the outermost GEM foil, then it should be possible to adjust the GEM voltages so that the outer surface remain near the nominal potential. This could be achieved by increasing the potential on the other surface. This will allow the remainder of the TPC to operate with little or no field distortions. For the micromegas case, this would require the readout pad plane to be disconnected from ground in this circumstance. Later, during a shutdown period if necessary, the TPC could be opened and the readout sector can be replaced. The wire grid in front of the readout modules will reduce the distortions caused by such failures, but will not eliminate them.

### 5.1.6 Electronics and data acquisition

#### Requirements and constraints

The very large number of channels balanced by a modest event rate require an ingenious and innovative system design for the read-out electronics of the TPC at T2K experiment. The desired spatial resolution dictates a small size of typically 8 mm $\times$ 8 mm for detector pads, leading to 86,000-130,000 channels for the 3 TPC modules (for an instrumented surface $2 \times 0.50\mathrm{m}^2$ up to $2 \times 0.80\mathrm{m}^2$ per TPC readout plane). The information conveyed by the amplitude of detector pad signals covers a dynamic range of 10 bits. Assuming a 1.25 m drift distance, quantization with 512 regularly spaced points seems adequate to meet the desired resolution in the drift direction.

The drift velocity of the gas envisaged lead to a maximum drift time of 50-500 $\mu$s. This translates into a sampling frequency of 2-50 MHz for the signals delivered by the pads.

The neutrino beam has a pulsed structure, the duration of a spill is of the order of 5 $\mu$s with a repetition period of 4 s. Outside of the beam spill time windows laser or cosmic ray calibration events be recorded at a rate of up to 20 Hz. The total uncompressed volume of data per event amounts to 50-80 MB. The maximum data flow is 800 MB/s, well within the capacity of modern networking components and storage devices. Lossless data compression, and possibly zero-suppression, can be used to further reduce event size.

One of the most challenging aspects of the present read-out system lies in the fact that the bulk of event data is generated within the very short 50-500 $\mu$s drift time interval, leading to a peak bandwidth of 100-1500 GB/s.

In order to develop the on-detector electronics independently of the choice of gas-amplification technology (GEM or Micromegas), read-out hardware compatible with both schemes shall be devised. Logical detector segmentation, connector types and board mechanics should be agreed to allow seamless integration of the same read-out cards with both types of detectors. The electronics mounted on the detector should be compact, tolerant to a modest magnetic field (0.2 T) and reliable enough to run during extended periods of time without being accessed. Power dissipation must be minimized; a water-cooling system will be required.

**Overall Design**

The overall design of the readout architecture comprises the following key components:

- 1344 72-channel analog front-end/SCA ASICs,
- 336 analog front-end cards housing the afore mentioned ASICs and ADC devices,
- 84 digital front-end mezzanine cards or local digital concentrator cards,
- 84 optical links to transport data to 6 off-detector concentrator cards,

In the following we will describe in more details the ASIC chip features.

The highly sensitive analog signals delivered by TPC pads must be carefully carried from the planes of the detector to front-end amplifiers and shapers. While integrating front-end electronics directly at the back of the detector itself would conceptually be an elegant approach, the technical risk is very high. A proven solution based on connectors, possibly avoiding the use of flexible cables, is being investigated.

Pre-amplifiers and shapers integrated on multi-channel custom ASICs are the first modular building block of the read-out system.

In order to provide a workable solution for the widest range of operating conditions, buffering all signals in the analog domain using a Switched Capacitor Array (SCA) integrated in the front-end ASIC is proposed. The device would comprise 72 channels, 512-cells deep each. Cells are written at 2-50 MHz to capture a complete event and are digitized at a different speed. Charge retention in capacitors preserve data for about 2 ms. The hypothetical 64 MHz ADC device considered would be able to read-out 190-240 pads, a substantial gain compared to the direct digitization scheme. Assuming that 1 ADC channel is allocated per front-end ASIC, the practical level of multiplexing achieved will be 72. The SCA-based scheme gives more flexibility for the optimal choice of readout speed, and power consumption will be lower.

Spreading over time the burst of data using analog memories lowers the demands for peak bandwidth, but requirements remain particularly high (25-50 GB/s) at the output of the analog to digital converter stage. Current technology puts a much lower limit on the transport bandwidth achievable at a moderate cost with low risk. Data at the output of the ADCs can only be transported over very short distances (typically a few centimeters away via printed circuit board traces or a short cable), and must be buffered in the digital domain to further smooth information flow. Zero suppression could also be envisaged at that level. Spatial multiplexing will be used to aggregate the output of multiples ADCs (e.g. 16) into a single logic device, and time-division multiplexing over multiple optical fiber links is foreseen to transport data off-detector.

The shaping time constant will be selectable among several discrete values (typically 5 to 10) in the range of 100 ns to 4 $\mu$s. Thus the user will be able to adjust the shaping time to the gas properties.

The chip does not include any type of tail cancellation, normally required for a readout system with wire gas amplification.

The preamplifier is a simple charge sensitive preamplifier (CSA) with a rise time faster than 100 ns and a fall time of few tenths of microseconds. It is optimized for an input (detector + stray) capacitor of 10 pF to 15 pF. It includes overvoltage protections that may avoid the need of external diodes.

It is also possible to include in each channel a variable gain (discrete value 1, 2 and 4 for example) and an inverter selectable by slow control to make the chip easily adaptable to different detector configurations.

A test pulse can be sent individually (selectable by slow control) to each channel. It is useful for the test of the chip itself, but also to test the system once mounted on the detector. This feature could also be used for electrical calibration purpose, this has to be defined and specified.

A serial link allows to set the configuration parameters of the chip (e.g. gain, inversion, and time constant). Each chip should have an address set on the Front End Board. The link has to be defined. It can be I2C or SPI compatible. The ASIC contains the minimum intelligence and is mainly driven by external signals coming from the Front-End Board. To minimize digital to analog coupling, all these signals, as the SCA clock signal and the multiplexer clock will be provided in small level differential standard as LVDS.

The expected rms noise level could be as small as,

$$\mathrm{ENC} = 200e^- + 10e^-/pF$$

for a shaping time of $\tau_s = 1$ $\mu$s. For time constants smaller than this value, and as the noise is dominated by series-noise, it scales with $1/\sqrt{\tau_s}$. For longer time constants the noise decreases slower because of the 1/f noise.

A 10 to 12 bit dynamic range with an integral non-linearity of few percents seems feasible [41]. The ADC LSB value has to be defined to match detector characteristics. The target power consumption is $<$3 mW/channel with a single 3.3 V power supply.

Regarding its moderate working frequency, the front end ASIC can be designed in a pure CMOS 0.35 $\mu$m technology. This generation of technologies is now mature and offers good analog performances at an affordable cost. They are easily accessible for prototyping through multiprojects. The ASIC size is evaluated to 60 mm$^2$ for 72 channels, mainly dominated by the capacitor array area.

The analog front-end card holds several front-end ASICs and the associated ADCs. Two options are being studied for mounting these cards: parallel to the plane of the detector, or orthogonal.

To better isolate digital circuitry from sensitive analog signals and because fine pitch packages of modern Field Programmable Gate Arrays (FPGA) require high-class multi-layer printed circuit boards, the logic driving the front-end ASICs and ADCs will be placed on a separate card.

### 5.1.7 Calibration

#### Module alignment and distortion correction

Particle trajectories are reconstructed assuming that ionization electrons drift along straight lines through the TPC. Electric and magnetic field imperfections may distort the electron drift. In T2K, the low magnetic field and low drift velocity (when using a slow gas) strongly suppress the contribution of magnetic field to the distortions. Extensive electric field calculations are being performed to minimize electric field drift distortions at the design stage. In addition, a calibration scheme needs to be established to cope with unforeseen distortions. Furthermore, since most tracks cross more than one readout module, precise module to module alignment needs to be achieved.

Drift distortions can be investigated using known straight line tracks. Distortions introduce an artificial curvature that can be used to quantify their magnitude. In T2K, there are two sources of straight tracks: few GeV/c muons from high energy neutrino and cosmic.

Muons from neutrino interactions have the advantage of being rather parallel to the beam direction. The bulk of these muons will not be produced in the Fine Grain Detectors, but in the more massive material upstream of the TPC (pit walls and magnet, for example).

Cosmic muons cross the TPCs preferentially from top to bottom at a rate of several hundred Hz per TPC. The Muon Range Detector will be used to trigger on cosmic muons passing through the TPCs, in between beam spills. The momentum of cosmic muons will be high enough (after proper selection) that their trajectories are essentially straight lines. Cosmic muons have two drawbacks: their preferred trajectory does not correspond to the trajectory of muons from neutrino interaction, and mapping out the whole TPC volume will require extensive statistics. Such statistics will eventually be acquired but it is desirable to design a system allowing rapid investigation of distortions.

Artificially generated tracks can be used to complement the muon dataset. Straight lines may be produced by extracting electrons from aluminum strips located on the central cathode by using a UV laser. Accurate positioning of the aluminum strips will be achieved using the router to draw grooves into the central cathode. The aluminum strips, or possibly wires will then be forced into the grooves, hence ensuring positioning at the router accuracy of a few hundred microns.

#### Drift velocity calibration

The drift velocity inside the TPCs will vary with atmospheric pressure and hence it needs to be measured frequently. Cosmic muons crossing the central cathode may be used to calibrate the drift velocity. The system used to flash the central cathode could be used for drift velocity calibration, possibly using a photodiode as a trigger in order to avoid the timing jitter associated with pulsed lasers.

A drift chamber, connected to the same gas line than the TPCs could also be used for absolute drift velocity calibration purposes. A simple laser system could then be used to generate two laser beams at the near and far end of the drift volume. Such calibration chamber will be built if it is demonstrated that the cosmic muons and the flashing cathode system do not determine the drift velocity accurately enough.

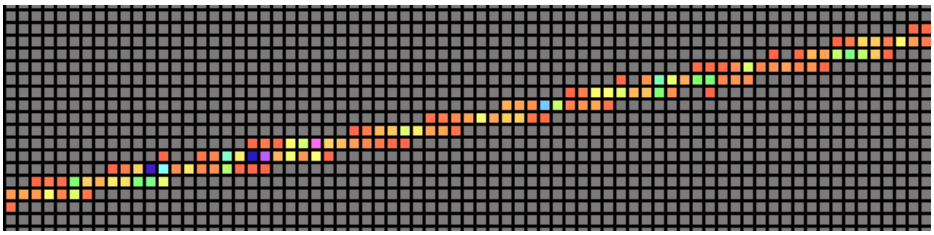

Figure 5.3: An example of a muon track as seen by the T2K TPC with 8 mm $\times$ 8 mm pads as simulated by the Victoria LC TPC simulation package. The different colors correspond to different charge collected by each pad.

#### Gain calibration

Gas gain varies with gas density. Both GEM and Micromegas can introduce gas gain non-uniformity. The electronic gain will also vary with a magnitude that remains to be determined. Requirements on gain are set by the energy loss resolution necessary to separate electrons from muons. Gas gain calibration options include the use of a radioactive gas as was done at CERN by the NA49 experiment, embedding radioactive sources (Fe55) in the chambers, and constructing a small calibration chamber to track the gas gain variation due to pressure. Gas gain non-uniformity may also be calibrated out by averaging over muon tracks, both cosmic and from neutrino interactions.

### 5.1.8 Expected performance

To estimate the momentum and $dE/dx$ resolution of the T2K TPC, software developed for the Linear Collider TPC R&D project has been adapted. This consists of a simulation and data analysis package that has been used successfully in prototype TPC data analysis. [43] The space point resolution estimates from the simulation agree quite well with the values seen in data for a range of diffusion parameters.

For the T2K TPC, about 300 $\mu$m space point resolution is required to achieve the momentum resolution goals. The charged particles traverse the TPC with a broad distribution of angles, and therefore cross many pad boundaries giving sufficient spatial information transverse to the particle direction. It is therefore not necessary in the T2K TPC to spread the charge by other means. Since the tracks are not parallel to pad boundaries, the "track-angle" effect degrades the resolution, but this is a small contribution in the case when the diffusion already contributes approximately 300 $\mu$m to the resolution. The optimal pad design for the T2K TPC is square or nearly square.

A full simulation has been performed to optimize the pad geometry and estimate the expected momentum resolution [44, 45]. In this study, GEANT3 is used to propagate muons, generated by the NEUT simulation of CCQE events, across an 60 cm wide Ar $CO_2$ gas volume in a 0.2 T field. The Linear Collider GEM-TPC simulation program converts the energy losses into electrons and the electrons drift, diffuse, pass through GEM holes, are amplified, diffuse and are collected on pads. The pad signals are generated, digitized, and signals stored in data files. An example track simulated with 8 mm $\times$ 8 mm pads is shown in Figure 5.3. The LC GEM-TPC analysis program reads the digitized data file, converts the signals to charge estimates, and performs likelihood track fits to estimate the track parameters. The likelihood track fitter uses an analytical model to describe the sharing of charges between pads, which accounts for the non-linear pad response function.

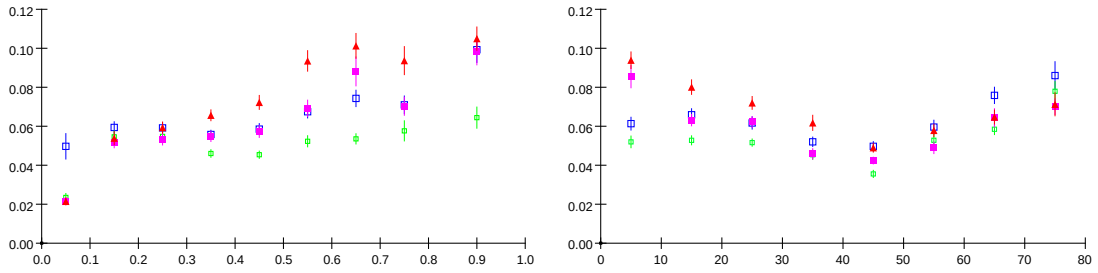


Figure 5.4: The relative transverse momentum resolution ($\sigma p_t/p_t$) vs. $p_t$ (GeV/c) at left and (right) azimuthal angle (degrees) at right are shown for muons in CCQE events. Different pad geometries are shown, blue large open squares: 8 mm $\times$ 8 mm with stagger, green small open squares: 6 mm $\times$ 6 mm with stagger, magenta closed squares: 8 mm $\times$ 8 mm without stagger, red triangles: equilateral triangles (12 mm side length).

The differences between the true and reconstructed transverse momenta are used to characterize the resolution. The residual distributions for different ranges of transverse momenta or azimuthal angle are fit to Gaussians and the standard deviations indicate the resolution. Figure 5.4 show the results for some of the pad geometries considered. The study indicates that the optimal geometry is roughly square pads without stagger. The resolution goal appears to be achievable with 8 mm $\times$ 8 mm pads, and is relatively robust against electronic noise or gain variation. Momentum resolution is improved by reducing the pad size.

Monte Carlo events produced by NEUT indicate that there will be sufficient samples of $K^0_s$ to check the momentum scale to 1% and verify the momentum resolution directly with the data.

A reasonable estimate of $dE/dx$ resolution can be obtained by the empirical formula [46]:

$$\frac{\sigma(dE/dx)}{(dE/dx)} \approx 0.41 n^{-0.43} (xP)^{-0.32}$$

where $n$ is the number of samples, $x$ is the sampling length in cm, and $P$ is the pressure in atmospheres. This formula reproduces the achieved $dE/dx$ for a variety of large drift chambers and TPCs. Cosmic ray data taken with the Victoria TPC prototype at $B = 4$T, with P5 gas and double GEM readout, was found to have resolution of approximately 17%, compared to the result from the empirical formula of 16%. The modest resolution is due to the small sampling length of 8.6 cm.

For the T2K TPC with 8 mm $\times$ 8 mm pads, the formula predicts the $dE/dx$ resolution to be about 7%, for tracks that traverse 60 cm of gas. This would provide better than $3\sigma$ separation for electrons and muons for momenta between 0.3 GeV/c and 1 GeV/c.

## 5.2 FGD: Fine Grained Detector

The bulk of the target mass for the ND280 detector will consist of layers of segmented scintillator bars read out by wavelength-shifting fibers. Fine-grained segmentation allows tracking of all charged particles arising from neutrino interactions with the target nuclei. In particular, for neutrinos near $\sim 700$ MeV, the dominant reaction would be CC-QE: $\nu_\mu\ n \rightarrow \mu^-\ p$, and the ability

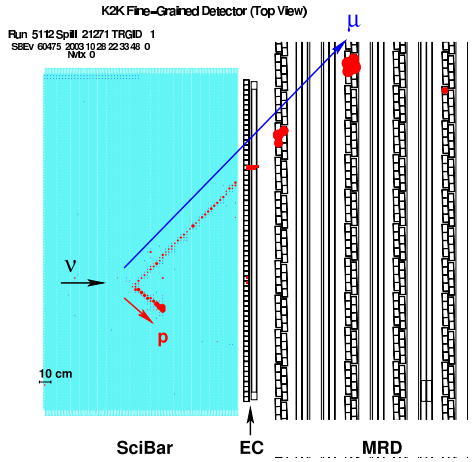


Figure 5.5: A CCQE candidate event observed in the K2K SciBar detector. Both a muon and a proton tracks are clearly observed. The size of circle is proportional to the energy deposit.

to track both outgoing particles gives a strong kinematics constraint to reject backgrounds. Using a scintillator, not a Cherenkov detector, allows the detection of particles below the Cherenkov threshold, such as the recoil protons in the above reaction. The scintillator itself provides the target mass for the neutrino interactions. K2K's SciBar detector has demonstrated the utility of such a fine-grained segmented detector, built from extruded plastic scintillator bars.

The ND280 detector will contain two fine-grained detectors (FGDs), each with dimensions of 200 cm $\times$ 200 cm $\times$ 30 cm (scintillator volume only, not including supports or electronics). One FGD will consist of $x$-$y$ layers of plastic scintillator bars read out with wavelength-shifting fibers, similar to the SciBar detector. The second detector will be a water-rich detector. Initially this detector will consist of $x$-$y$ layers of plastic scintillator alternating with 3 cm thick layers of passive water. R&D work is continuing on a water-soluble liquid scintillator mixture that could be used to produce an all-active water FGD that would replace the passive water FGD as a future upgrade. All three detectors (plastic FGD, active water FGD, and plastic+passive water FGD) will be built with the same geometry, mounting, and readout.

### 5.2.1 Plastic fine-grained scintillator detector

The ND280 plastic fine-grained scintillator detector (plastic FGD) is analogous to the K2K SciBar detector described in [47, 48]. The event display of SciBar for charged-current quasi-elastic (CCQE) events is shown in Figure 5.5 where both a muon and a proton tracks are observed. The particle of a track is identified by the deposited energy at each scintillator bar.

In the T2K experiment, finer segmentation of the scintillator is desirable because the neutrino energy is lower than that of K2K, and because higher precision is required. Accordingly the size of the scintillator bars for the plastic FGD is $1.0 \times 1.0 \times 200\ \mathrm{cm}^3$, and the surface is covered by $TiO_2$ reflective coating. Each scintillator bar has a hole in which a wave-length shifting (WLS) fiber is installed. As an example, the drawing of the scintillator bar used for SciBar is shown in Figure 5.6. The extruded scintillator is planned to be produced in Canada with co-extrusion technique of the reflective coating.

The detector size is $200 \times 200 \times 30\ \mathrm{cm}^3$ resulting in the total mass of 1.2 tonnes, which does

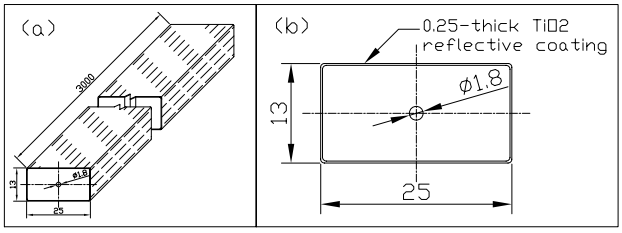


Figure 5.6: A drawing of the scintillator strip used for the K2K SciBar detector. The scintillator has a hole in the middle, and the surface is covered by $TiO_2$ reflective coating.

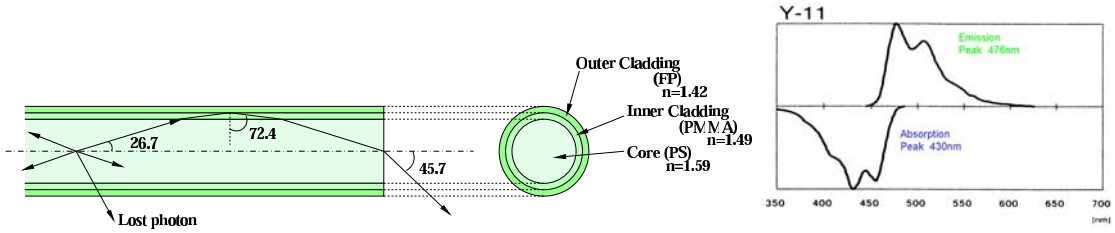


Figure 5.7: (Left) Drawing of the Y11 double-clad WLS fiber. (Right) Absorption and emission spectra of the Kuraray Y11 WLS fiber.

not include supports or electronics. One layer consists of 200 scintillator bars, and thirty layers are arranged in alternating vertical and horizontal layers perpendicular to the beam direction. The tracking threshold is expected to be $\sim 4$ cm, which corresponds to 350 $MeV/c$ for a proton.

Kuraray Y11 wave-length shifting (WLS) fibers are used for light collection and light propagation. The absorption and emission spectra of Y11 are shown in Figure 5.7. The absorption spectrum of WLS fiber is well matched with the emission spectrum of the extruded scintillator ($\sim 420$ nm).

Double-clad WLS fiber is adopted to increase the light collection efficiency. The drawing of the double-clad fiber is shown in Figure 5.7 The WLS fiber diameter is 1.5 mm, chosen to match the diameter planned for the active water scintillator detector. A typical attenuation length of the fiber is 350 cm. Double-ended readout is highly desirable in order to reduce non-uniformities in response across the detector (which will correlate with off-axis angle), and to allow low threshold settings on individual channels through the use of a coincidence requirement between the two ends of each fiber. The preferred photosensors are silicon PMTs because of their small size, high efficiency, and immunity to magnetic fields. Based on the performance of SciBar, we would expect to measure 18 (9) photo-electrons/cm for a minimum ionization particle passing the near (far) side of the scintillator from the PMT with a Hamamatsu H8804 multi-anode PMT. A silicon PMT would increase this light yield by $\sim 30\%$.

### 5.2.2 Plastic FGD with passive water target

The simplest way to produce a water-rich FGD with high oxygen content is to replace scintillator layers with layers of passive water. The "passive water FGD" consists of $x$-$y$ layers of scintillator bars alternating with 3 cm thick layers of passive water (no readout). These water layers will be constructed from sheets of corrugated polyproplyene, of dimension 1.0 m x 2.0 m, and an outer

thickness 1.0 cm. These are commercially available and inexpensive (about $25 US per panel). Each panel consists of a line of hollow square cross-section cells, of inner dimension 8.5 mm x 8.5 mm. Two such panels mounted side by side will constitute one detector layer of size 2.0 m $\times$ 2.0 m $\times$ 1 cm. The ends of the panels are sealed with a thermal weld to a polypropylene bar, and the interior of the panel is filled through fill and drain ports at the top and bottom. This design can reliably hold water without leaking, while the corrugated plastic panel readily supports the pressure of the water.

The baseline configuration for such a detector is to alternate an $x$-$y$ pair of plastic scintillator layers with three passive water layers. The total water content of this "2+3" configuration is 47% by weight. The FGD then contains 6 pairs of active $x$-$y$ layers, with a total channel count of 4,800 (assuming double-ended readout). Each passive section has a thickness of 3 cm perpendicular to the beam direction.

Neutrino interaction rates on water may be obtained from a subtraction analysis in which the rates on the all-plastic FGD and the passive water FGD are measured, corrected for any differences in efficiency, and then the interaction rates on carbon determined from the plastic FGD are subtracted from the plastic+passive water FGD to get the interaction rate for just water.

The plastic+passive water detector would cost between 33% and 40% of the cost of the plastic FGD. The passive water layers are inexpensive to produce, and add negligible cost to the total. Detailed Monte Carlo simulations are needed to optimize the thickness of the passive water layers in terms of physics performance.

### 5.2.3 Water-based scintillator

#### Motivation & Detector Concept

A serious limitation of the SciBar design is that its target mass is mostly carbon, whereas the Super-Kamiokande far detector is *water*, and we wish to avoid systematic effects arising from the use of different nuclear targets. The effects of nuclear Fermi momentum, Pauli blocking, charge-exchange in the nuclear medium, and nuclear absorption on low energy final state hadrons are poorly understood. As one example, the production of $\pi^0$ mesons, which decay into photons and subsequently produce $e^+e^-$ pairs, is a major background whose signature could resemble electron appearance in the far detector, and it is unknown how this cross section differs between carbon and oxygen.

The passive water FGD described in Section 5.2.2 attempts to overcome this difficulty by alternative plastic scintillator layers with layers of passive (uninstrumented) water. While this approach is simple to implement and probably adequate, a better solution would be to have an all-active detector with no layers of dead material. This could allow greater efficiency for detecting short-ranged final state particles such as recoil protons. Therefore we have been developing a water-based scintillating liquid as an alternative target material to replace plastic scintillator extrusions. This liquid will be contained in commercial thin-walled corrugated polypropylene board with 1 cm x 1 cm x 2.0 m cells, and read out with the 1.5 mm-diameter WLS fibers. This would provide an oxygen-rich, fully active target water target. The mechanical construction of the active water target is very similar to that of the passive water layers of the passive water FGD, with the exception that now the panels will be instrumented with fiber readout.

Because even this water-scintillator target is only 55% water, when the plastic container and wavelength shifting fiber is taken into account, the all-plastic FGD consisting of plastic scintillator only is still required. The active water scintillator FGD would thus replace the passive water FGD, and could be introduced as a detector upgrade once remaining R&D issues are resolved.

Comparison of the yields from the plastic scintillator and water scintillator sections will allow us to unfold the yields from carbon and oxygen separately through a statistical subtraction.

To simplify both construction and comparison of data from the plastic scintillator and water scintillator sections, both will have identical granularity of 1 cm x 1 cm and be read out by 1.5 mm diameter wavelength shifting fibers into SiPM photosensors.

There are still questions regarding the long term compatibility of the water scintillator liquid with the polypropylene container. This question is now being addressed in ongoing long term tests. For this reason the passive water FGD is defined as the baseline design. The active water scinitllator is a potential upgrade/replacement for the passive water FGD.

**Scintillator Mixture**

A suitable water-soluble liquid scintillator is "Quicksafe A" made by Zinsser Analytic [49]. The active ingredient is di-isopropylnaphthalene. It is both biodegradable and has a high flashpoint of $>150^{\circ}$C, and is thus "safe". Beam tests at TRIUMF show that the light yield of water-Quicksafe cocktails is linearly proportional to the concentration of Quicksafe A, and pure Quicksafe A by itself gives 80% the light output of plastic scintillator. A mix of 70% water, 25% Quicksafe A and 5% Triton X-100 surfactant gives a hazy clear scintillating liquid. By adding 0.1 grams of Carbopol EZ-3 to 20 ml of the 70/25/5 mix and partially neutralizing with 0.122 ml of NaOH solution (2% by weight) a clear gel can be formed. Although it was initially thought that a gel would both slow down chemical attack on structural plastics and inhibit leaks, tests have contradicted these expectations, and the difficulty of filling the vessel with gel and replacing it if it degrades lead us now to favour a liquid.

**Mechanical Design**

We propose to construct the scintillator layers from panels of extruded corrugated white polypropylene, of dimension 1.0 m x 2.0 m, and an outer thickness 1.0 cm, as described in Section 5.2.2. Alternating $x$ and $y$ layers will be glued together for strength, and to eliminate net hydrostatic forces on all interior walls. A wavelength shifting fiber of diameter 1.5 mm will run down the centre of each cell to collect the scintillation light and carry it to a photon detector at each end of the fiber.

Polypropylene (PP) is chosen as the structural material because of the easy availability of extruded panels of the correct dimensions. It is moderately resistant to chemical attack by the Quicksafe, but not completely so. It is much more resistant than Polyvinyl Chloride (PVC), but not as good as High Density Polyethylene (PDPE). Unfortunately, it is difficult to extrude HDPE, and the one supplier of HDPE panels that we could find supplied samples of such poor quality that they were judged to be useless for our purpose.

Samples of PP exposed to Quicksafe at various temperatures caused the Quicksafe to turn yellow. Spectrophotometer measurements of the yellowing show that the yellowing is quite rapid at first, but plateaus after about 4 weeks and thereafter does not yellow further. The higher the temperature, the deeper the plateau. This behavior indicates that the reaction of the PP with the Quicksafe reaches a temperature-dependent chemical equilibrium. It is therefore invalid to "speed up" the aging process by elevating the temperature; the effect of 1 year of aging at room temperature is not the same as 1 month of aging at 40C. We are in the process of studying the long-term deterioration of the light output as a function of time by periodically monitoring the behavior of sample cells held at room temperature.

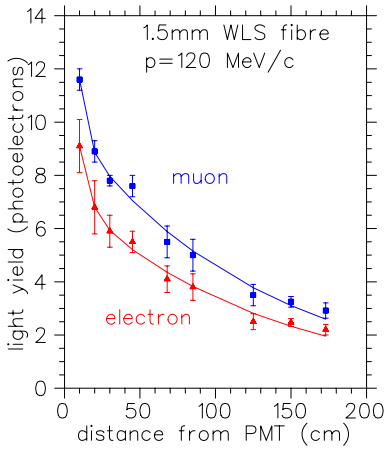


Figure 5.8: Light yield for 120 MeV/c muons (top set of points) and electrons (bottom set of points), for single-cell prototype with 1.5 mm diameter fiber and XP2262 PMT

The PP surface can be protected by painting the interior walls with Eljen-520 reflective paint, which resists chemical attack by liquid scintillators. The adhesion to bare PP is not strong, but can be improved with the use of primers design expressly for PP, such as Krylon Fusion, Rust-Oleum Plastic Primer, and Dr. A. Schoch PP Primer. Beam tests have shown that the use of reflective paint improves the light output by about 15%. Tests are underway to ascertain the long term adhesion and reflectivity of reflective paint in the presence of Quicksafe A.

**Beam Test of Prototypes**

The M11 beamline at TRIUMF provides low-intensity beams of electrons, pions, muons and protons of variable momentum. At 120 MeV/c, the different particle types are easily identified by time of flight. We have conducted beam tests of a detector composed of one single cell of a corrugated plastic panel, about 170 cm long, with a single 1.5 mm WLS fiber running along the length of the cell. One end is coupled to a Phillips XP2262 photomultiplier, and the other end is cut at a 45 degree angle and blackened to minimize reflections. This gives a good indication of the light yield that we could expect from a detector constructed as proposed above. The light yield as a function of the distance of the beam from the photomultiplier is shown in Figure 5.8. At a distance of 1.2 m from the PMT, the light yield is about 2.5 photoelectrons for a minimum ionizing particle. This is small, but with the superior quantum efficiency of a SiPM as a photon detector, and double-ended readout, we may expect a total of perhaps 6 or 7 photoelectrons per channel for a minimum ionizing particle. By contrast, protons of momentum 270 MeV/c produce 33 photoelectrons in our one-ended test setup with the XP2262 PMT, about twice what we would expect by scaling the light yield observed for muons and electrons by dE/dx. This shows that for the foremost purpose of the water scintillator, namely, as a tracker for the recoil proton from CC quasielastic events, there is adequate light.

### 5.2.4 FGD Photo-sensor: SiPM's

The candidate photo-sensor for the FGD is Silicon PM (SiPM), because it allows photon counting inside magnetic field. Unlike VLPC, its operation is very simple without a need of cryogenic

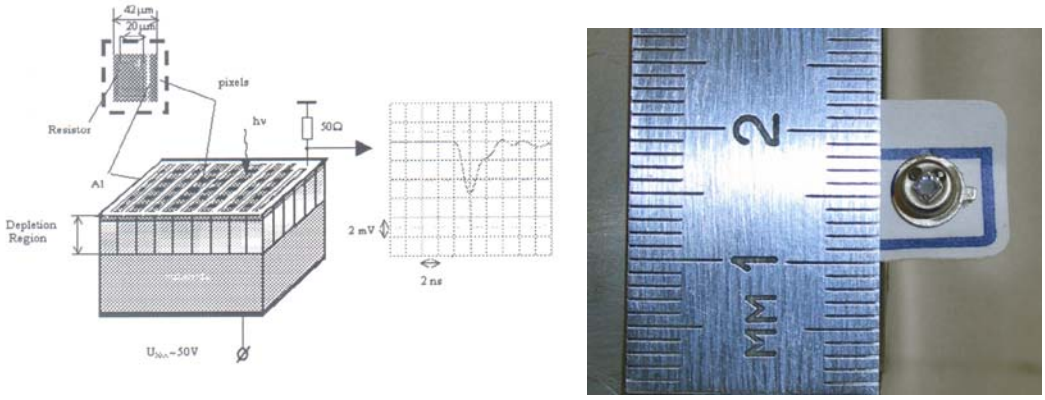


Figure 5.9: (Left) SiPM view. (Right) Photo of a SiPM. Diameter of the cylindrical container is about 3 mm.

system. The technology is becoming matured for experimental use.

**Introduction**

Detailed description of the avalanche photo-diodes with metal-resistor-semiconductor layer-like structure operating in the Geiger mode [50] technique can be found in [51, 52, 53, 54]. This detector (hereinafter SiPM) is a multi-pixel semiconductor photodiode which consists of pixels on common substrate. The detector view is shown in Figure 5.9. Each pixel operates as an independent Geiger micro-counter with a gain of the same order as a vacuum photomultiplier. Geiger discharge is initiated by a photoelectron, thermally or by high electric field. Gain is determined by the charge accumulated in pixel capacitance: $Q_{pixel} = C_{pixel} \cdot \Delta V$, where $\Delta V$ is the difference between the bias voltage and the breakdown voltage of the diode (overvoltage). Since $\Delta V$ is about a few volts, $C_{pixel} \simeq 50$ fF, then $Q_{pixel} \sim 150$ fC that corresponds $10^6$ electrons.

A single pixel signal does not depend on a triggered number of carriers in a single pixel. In such a way, the SiPM signal is a sum of fired pixels. Each pixel operates as a binary device, but SiPM on the whole is an analogue detector with the dynamic range limited by a finite number of pixels. Therefore, the nuclear counter effect for SiPM is negligible small.

The pixel size can be of 15 to 70 $\mu$m, and the total number of pixels is 100-4000 per mm$^2$. The tested SiPM's of 1x1 mm$^2$ sensitive area with $\leq 1000$ pixels were developed and produced by PULSAR (Moscow), CPTA Company (Moscow) and at Dubna. The detector photos are shown in Figure 5.9.

**Main parameters of SiPM**

**Gain**

Typical bias voltage is in the range of 25–50 V. SiPM has excellent single photoelectron resolution determined mainly by electronics noise even at room temperature. It means that there is only a small pixel to pixel gain variation as well as small fluctuations in Geiger discharge development. The absolute gain depends on the SiPM topology and bias voltage and typical values are in the range $(0.5 - 1.0) \times 10^6$. Gain between different SiPM's of the same type varies within $\pm$25% at fixed bias voltage.

**Photon detection efficiency**

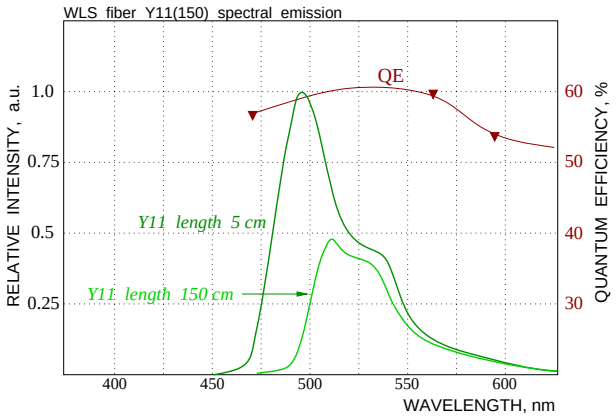


Figure 5.10: Light emission spectrum of Y11(150) fiber and the quantum efficiency of the SiPM.

The SiPM photon detection efficiency consists of 3 components: $\varepsilon = QE \cdot \varepsilon_{Geiger} \cdot \varepsilon_{pixel}$, where $QE$ is the wavelength dependent quantum efficiency,
$\varepsilon_{Geiger}$ is the probability for a photoelectron to initiate the Geiger discharge,
$\varepsilon_{pixel}$ is a fraction of total active SiPM area occupied by sensitive pixels.
Measured SiPM $QE$ is shown in Fig. 5.10 as well as the emission spectrum of the WLS fiber Y11(150). Peak emission of the fiber depends on its length due to light absorption while the SiPM sensitivity is almost flat for green light. $\varepsilon_{Geiger}$ depends on applied bias voltage and comparable with $QE$, $\varepsilon_{pixel}$ is determined by topology of SiPM, its typical value is about 40-60%.

**Dynamic range**

The SiPM dynamic range is limited by the finite pixel number $m$. The finite number of pixels results in the saturation of the SiPM signal with increased light intensity. For practical estimation the following assumption can be made: the response of SiPM becomes non-linear at signal value $N_{p.e.} > 0.2 \cdot m$.

**Timing**

The development of the Geiger discharge in a short depth ($\sim 0.8\ \mu m$) of depletion region takes a few hundred picoseconds. The typical rise time is 1 ns, the decay time determined by the pixel capacitance. The intrinsic time resolution measured with a very fast red-laser diode follows the Poisson law: $\sigma_t = 120ps/\sqrt{N_{p.e.}}$.

**Noise**

The limiting factor of the SiPM performance is dark current rate, which originates from the carriers created thermally and also due to the effect of high electric fields. The dark rate decreases with temperature from about 1–2 MHz/mm$^2$ typical value at room temperature to $\sim$1 kHz/mm$^2$ at 100°K.

### Test results

There is good progress in development of SiPM's by CPTA and INR provide intensive R&D work with this Company. Here, we mainly presented the test results of new SiPM's with 600 pixels on 1x1 mm$^2$ sensitive area developed and manufactured by CPTA.

Single photoelectron resolution of SiPM was checked with a blue LED. The light from this LED was directed to a SiPM through the short Y11 fiber. Figure 5.11 shows the spectrum of the LED flash. Resolution here is determined by electronic noise of fast amplifier and pick-up noise

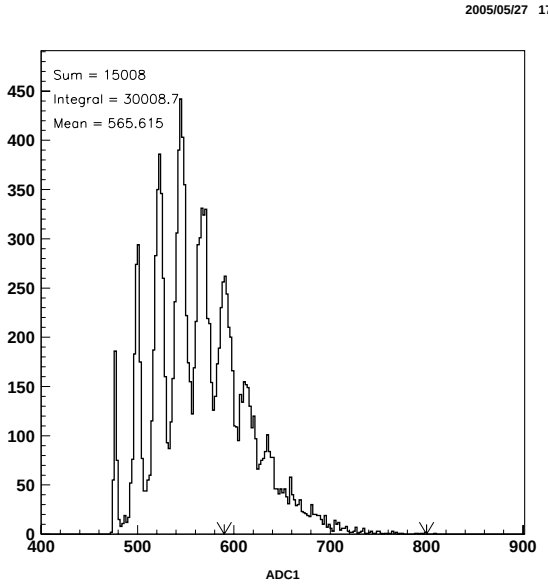


Figure 5.11: SiPM spectrum of LED flash of low amplitude.

produced by cabling, ground loops, etc. Intrinsic gain stability of SiPM allows us to see the ADC signal with separated peaks which correspond 1, 2, 3... pixels.

The SiPM read out the cosmic MIP signals produced by a scintillator tile with WLS fiber. Cosmic test configuration is shown in Figure 5.12. WLS fiber Y11 Kuraray of 1 mm diameter embedded in the scintillation tile groove. One end is attached to the SiPM with air contact, another end is covered by a reflector. Total fiber length is 120 cm, thickness of plastic scintillator is 0.5 cm. SiPM signal was sent to the fast amplifier (gain 10) through 5 m long coaxial cable. Cosmic MIPs were selected by a couple of trigger counters. Then SiPM has been replaced with a phototube FEU-115M with the green-extended photocathode. The amplifier was off for a PMT. Both readout devices were calibrated by a blue LED which light passed through a hole filled with a Y11 fiber.

The SiPM and PMT cosmic spectra are shown in Figure 5.13. SiPM provides 20% higher light yield than the PMT. However, there is a wide pedestal peak in SiPM spectrum. This spread is caused by accidental coincidences of dark SiPM pulses with the 150 ns ADC gate. The advantage of SiPM over PMT becomes more visible at longer light wavelength. The fiber was replaced with a longer one with length of 3.3 m. The obtained spectra are also shown in Figure 5.13. After light travels 3 m along the fiber its peak wavelength is shifted to the longer range (see Figure 5.10), where PMT sensitivity drops. Therefore, SiPM provides 1.5 times more light than the phototube at long fiber length.

The efficiency of SiPM and correspondingly the light output depend on the bias voltage (see Figure 5.14). The higher bias voltage increases the probability of the Geiger discharge. However the dark rate raises also.

Accidental dark pulses widen the pedestal as it can be seen in the inset in Figure 5.13. A single photoelectron peak is clearly visible. Dark pulses of higher amplitude extend the pedestal longer. Dark pulses degrades the low energy spectrum part affecting the rare signals of small amplitude. However it seems that the threshold of 3-4 p.e. suppress completely the dark noise. It is seen from the Figure 5.15, where dark rate dependence on the threshold is demonstrated. These measurements were done for the bias voltage values which provided similar to a green extended

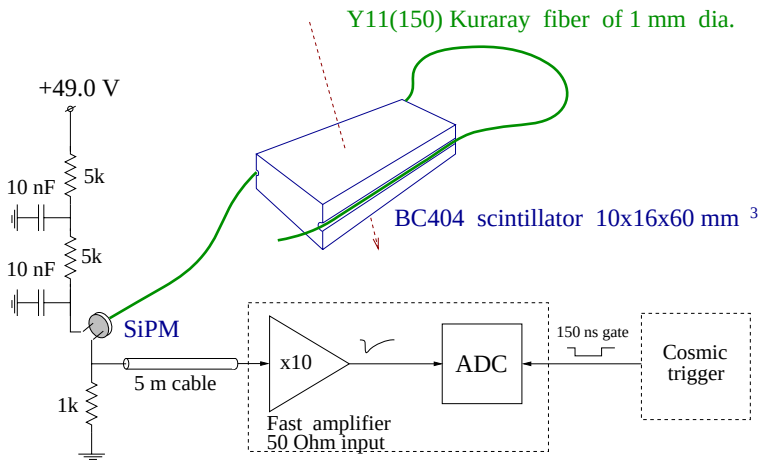


Figure 5.12: Cosmic test bench.

PMT sensitivity to the scintillation signal for a detector with WLS readout. These measurements show very fast reduction of the dark rate for higher threshold. The dark rate drops by about 30 times when thresholds was increased from 0.5 p.e. to 1.5 p.e. and almost 1000 times for the threshold of 2.5 p.e. This clearly shows low cross talk between micropixels. If for example, a detector has rather high l.y. to keep the threshold at the level of 2.5 p.e. the dark rate will be only at the level of a few kHz.

Temperature dependence of the signal was also measured. The result is shown in Figure 5.16. The signal has a negative temperature gradient of about 4.3%/degree. Therefore, it is very desirable to keep temperature stable or measure it with good accuracy. The long time stability of SiPM was tested using a LED signal. The result is shown in Figure 5.17. As seen from this figure, the tested SiPM did not show any drop of the signal for rather long time of about 900 hrs. Another important test which provides some information about life time of these devices is the high temperature test. First test was done for fifteen 25V SiPM's. They were kept at the temperature 77°C for 91 hrs. Dark current, dark rate and QE of all 15 devices measured before and after temperature test did not show any degradation within 5% accuracy of measurements. All devices were alive after this test. Then, we kept nine devices at working bias voltage and temperature of about 80°C for 10 days. The difference between LED signals of these SiPM's before and after temperature test is shown in Figure 5.18 There are no dead devices after such heating test and there is no essential degradation of the signal. Difference $\pm 10\%$ can be explained not very precise measurement of the temperature. This corresponds the life time of more than 2 years at room temperature. These tests will continue to provide more information about life time of SiPM's.

It was expected that these devices are not sensitive to magnetic field. The results of such measurements are presented in Ref. [55] and shown in Figure 5.19.

### FGD electronics

Because FGD has intrinsic timing resolution of nanosecond, it would be desirable to have electronics that keeps up with it. The good timing would help in measuring time of flight of the particles for particle identification. The end-to-end timing would help reducing the accidental noise and identifying the coordinate along the fiber direction.

One candidate front-end electronics is a system based on Trip-t ASIC developed at Fermilab

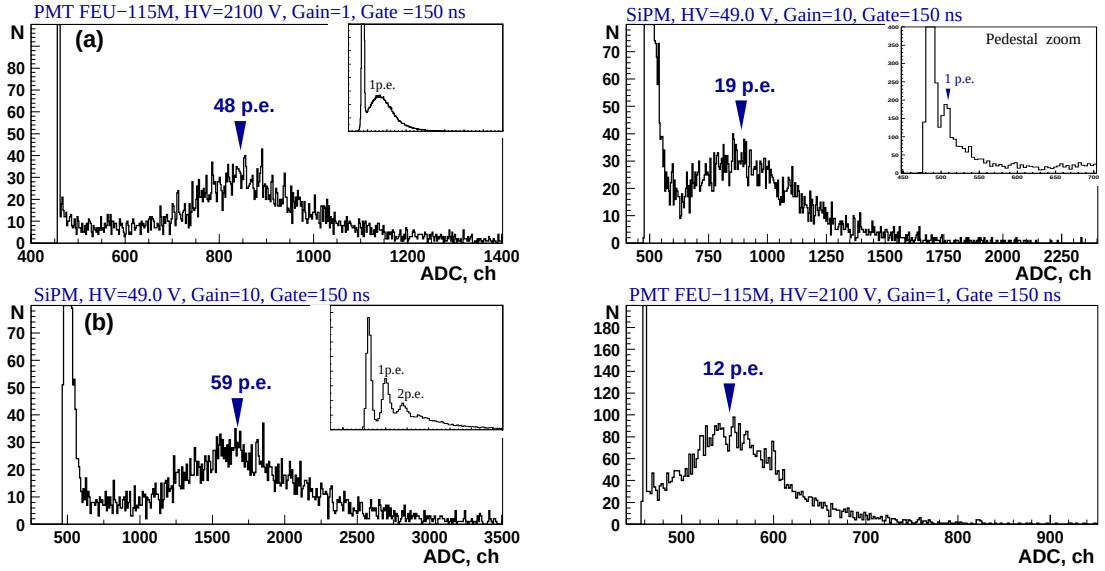


Figure 5.13: Cosmic spectra of reference green-extended PMT (Left-top), and SiPM at 49.0 V bias voltage (Left-bottom) with the shorter fiber length of 50 cm. Insets show the calibration single photoelectron spectra obtained with a LED. In comparison with the longer fiber length of 3.3 m, the cosmic spectra of SiPM (Right-top) and PMT (Right-bottom) are also shown with an inserted zooms for the SiPM pedestal.

for D0 experiment. Both charge and timing information is stored in the switching capacitor array (SCA) with a depth of 40 hits. The hits stored in SCA during the fast extracted beam period of 5$\mu$sec is stored in SCA, are readout in between spills by ADC controlled and zero-suppressed by FPGA.

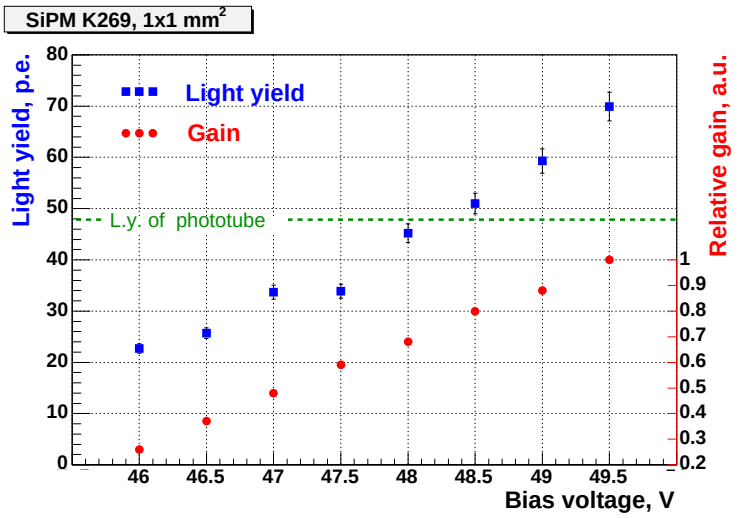


Figure 5.14: Light yield and relative gain of SiPM versus applied bias voltage. Above 48 V the SiPM efficiency exceeds the one achieved with a green-extended phototube. Relative gain of 1.0 corresponds to the absolute gain of $1.6 \times 10^6$. Threshold = 0.5 p.e.

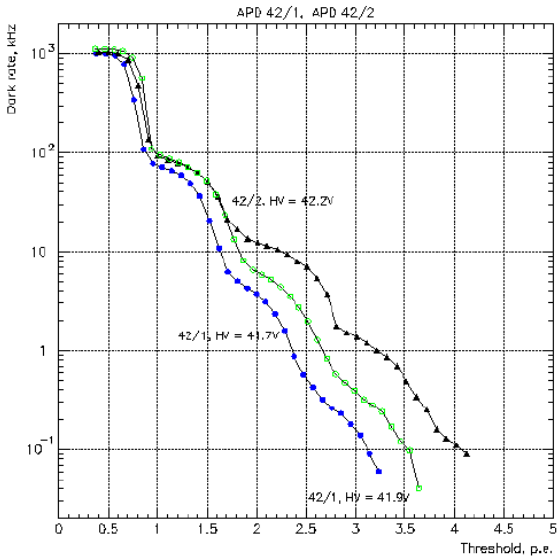


Figure 5.15: Dark rate versus the threshold (in p.e.). The bias voltages shown here provided the light yield of tested SiPM close to the light yield of a green extended PMT.

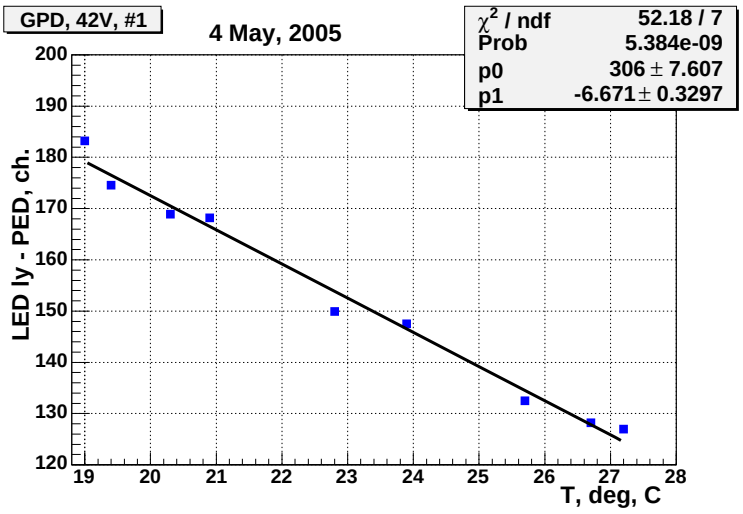


Figure 5.16: Temperature dependence of the SiPM signal from a LED.

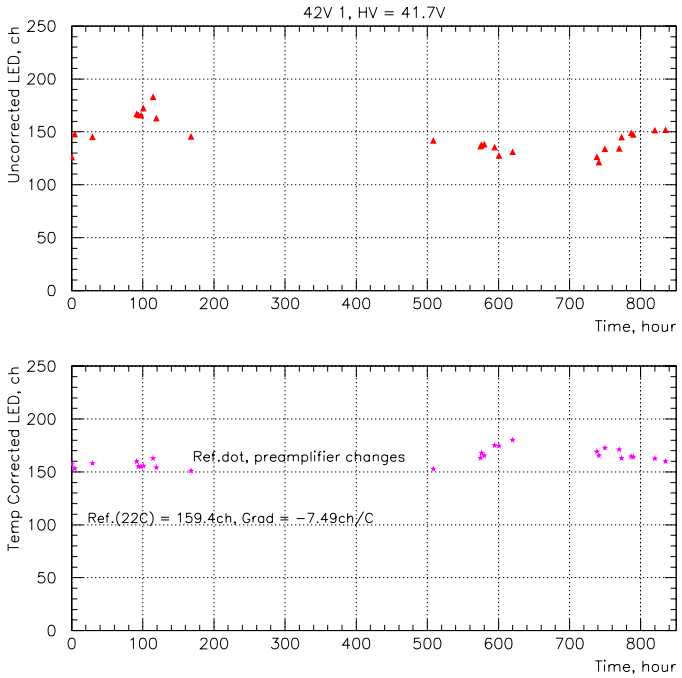


Figure 5.17: Test of stability of the SiPM signal. Top figure – no temperature correction is applied, bottom – with temperature correction.

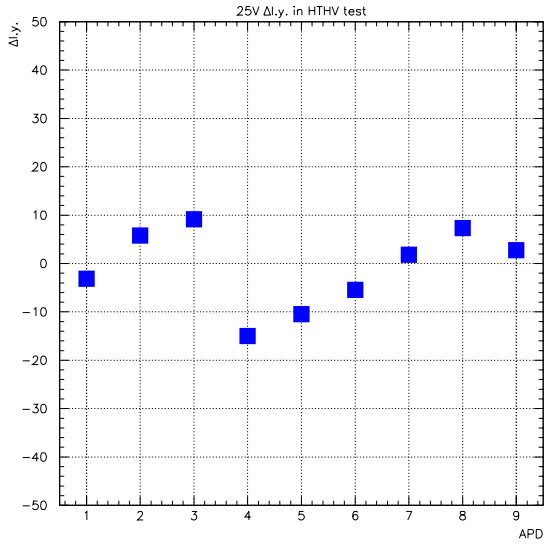


Figure 5.18: Difference (%) between signals before and after heating.

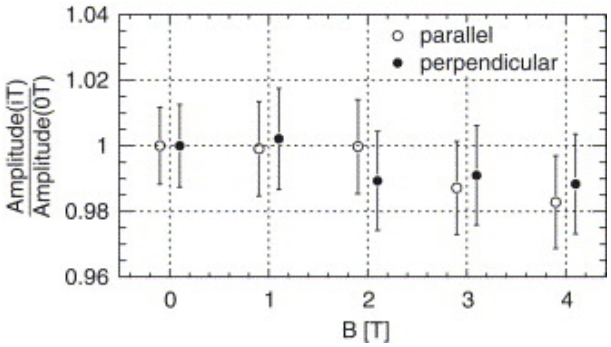


Figure 5.19: Dependence of the SiPM signal for two directions of the magnetic field [55].

# Chapter 6

# The P0D Detector

## Technical Overview

The Pi-Zero Detector (P0D) which sits at the upstream end of the ND280 off axis detector has been designed to make a high precision measurement of neutrino interactions which contain electromagnetically showering particles using a water target, and the tracking detector which sits downstream of the P0D (see Figure 6.1). The P0D detector consists of an instrumented target region surrounded by an electro-magnetic calorimeter. The calorimeter is shared with the down stream tracking detector and is discussed elsewhere. This section will primarily describe the instrumented target region (which will be referred to as the P0D for convenience). The P0D is a scintillating bar detector that is similar to the successful K2K SciBar [47] and the approved MINER$\nu$A detectors. A diagram of the detector is shown in Figure 6.1.

Scintillating bar tracking planes are the primary component of the P0D. The baseline design has 76 tracking planes position perpendicular to the beam direction. The design is centered around a simple modular component that can be constructed away from the T2K site and later assembled in the detector hall. Remote construction will also allow quality control and survey to be done during the tracking module assembly phase.

The tracking planes are constructed of polystyrene triangular scintillating bars that are fabricated by co-extruding with a reflective layer $TiO_2$ and a central hole for a WLS fiber. The nominal bar has a 3 cm base and a 1.5 cm height and has a length of 180 cm or 210 cm. Tracking planes have thin layer of lead (nominally 0.06 cm) sandwiched between X and Y layer of interlocked scintillating bars to increase the efficiency to detect gamma rays from $\pi^0$ decay. The light seal for the tracking plane is maintained by light manifolds which collect the WLS fibers into optical connectors. Light will be transported to the photo-sensors using clear optical fibers.

Because of the large number of scintillating bars ($\sim$20,000) and available space limitations, it is impractical to route the fibers to photo-sensors outside of the magnetic volume. For this reason, the photo-sensors will be located within the inner detector basket.

One of the constraints facing the P0D is that the neutrino interactions must be measured on a oxygen target. In the baseline design, this is achieved by interleaving water target planes between the 30 upstream scintillating bar tracking planes. Oxygen cross section measurements will be made by comparing the interaction rate for events vertices in the upstream and downstream portions of the detector. This introduces a certain level of complexity into the design not present in either the SciBar or MINER$\nu$A detector, and affects track reconstruction efficiency. Care is taken to assure that the composition and detection efficiencies in the upstream and downstream

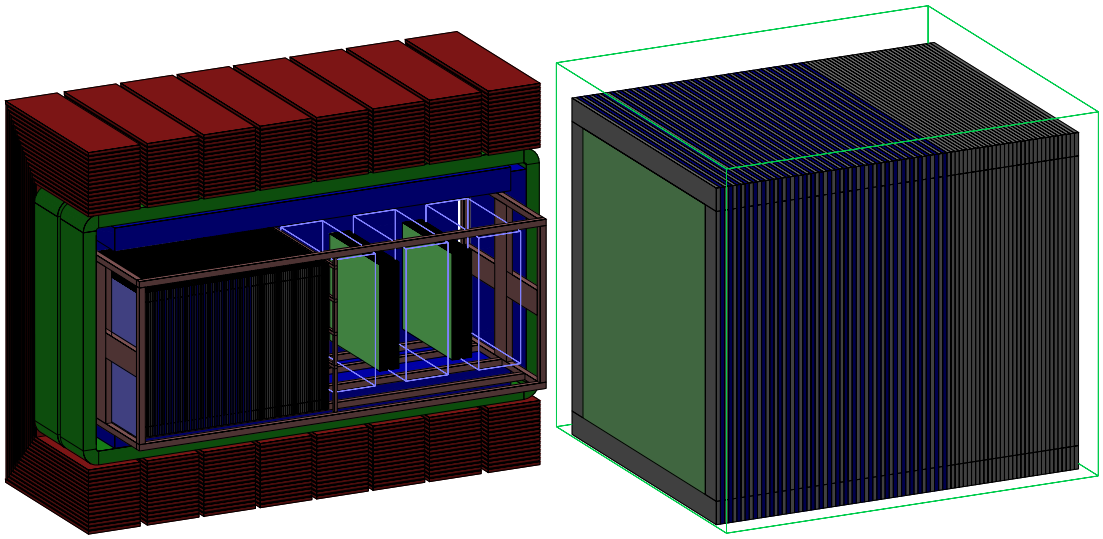

Figure 6.1: Left Panel: The location of the P0D in the ND280 off-axis detector baseline design. The neutrino beam is coming from the left with the P0D situated on the upstream side of the inner detector volume, followed by the tracking detector. Right Panel: A detail of the P0D target region. The green represents the scintillating bar tracking planes. The water target region is located in the first two thirds of the detector and is indicated by blue.

detector regions are well controlled. The oxygen target is provided by a $\sim$3 cm thick water target. Candidate containers have been identified and are expected to introduce an additional 0.06 $g/cm^2$ of material.

The baseline detector design has a total mass of approximately 12 tons with a fiducial mass of 1.7 tons of water, 3.6 tons of plastic scintillator, and 0.8 tons of lead. Based on the expected event rates, we expect to collect a total sample of approximately 60,000 neutral current single-$\pi^0$ events for an exposure of $10^{21}$ POT (approximately one year), of which approximately 17,000 occur in the water target. This number will be reduced by the reconstruction efficiency. As discussed below, this large sample of $\pi^0$ events is required to predict the $\pi^0$ production rate at Super-Kamiokande as a function of momentum and direction.

## 6.1 Capabilities

The capabilities of the P0D have been studied using a detailed detector simulation and track pattern recognition. Where the results depend on the behavior of the photo-sensor, the light collection has been tuned to match the MINER$\nu$A vertical slice test and corresponds to approximately 22 photo-electrons per layer per MIP.

### 6.1.1 Photon reconstruction capability

The P0D has been designed to have the largest possible target mass, while maintaining a large efficiency to reconstruct low energy gamma rays. The baseline active target described in this proposal has not been fully optimized, but we believe it sufficiently demonstrates the potential for this detector.

| Energy | Overall Efficiency |
|---|---|
| 50 MeV | 68% |
| 100 MeV | 81% |
| 200 MeV | 85% |
| 400 MeV | 85% |

Table 6.1: The efficiency to reconstruct a gamma ray as a function of the true gamma ray energy.

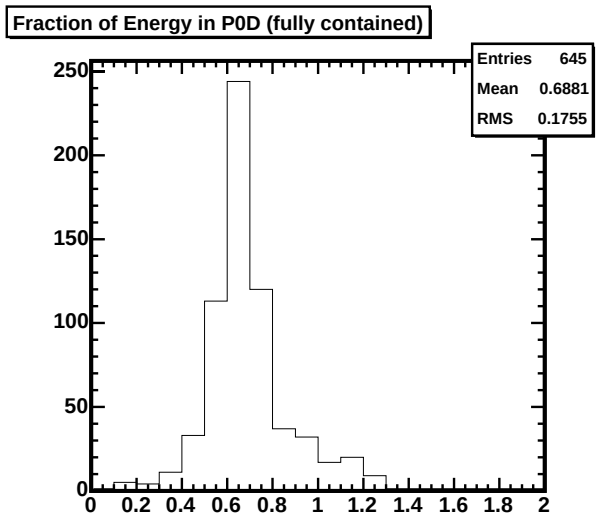


Figure 6.2: The figure shows the fraction of the fully contained 200 MeV gamma ray energy measured in the scintillator after applying corrections for the P0D energy response.

The primary goal for the P0D active target is to measure neutral current single $\pi^0$ production where in the typical case, all particles traveling further than a few centimeters from the interaction vertex without a hit will be neutral. For this reason, it is quite important that the P0D have high efficiency to detect gamma rays leaving the fiducial volume. By requiring a localized cluster of energy deposition in either the X or Y projection, the active target will detect 85% of gamma rays with $E_\gamma > 100$ MeV that originate more than 30 cm from the edge of the detector. The detection efficiency drops to 68% for $E_\gamma = 50$ MeV. The efficiency as a function of energy is shown in Table 6.1. Gamma rays which leave the target without depositing energy are likely to be detected in the P0D EM calorimeter which is discussed elsewhere.

Without accounting for photon-counting statistics of the light collected from the scintillating bars, the energy resolution for events fully contained in the active target is approximately $\sigma_E = 10\% + 3.5\%/\sqrt{\mathrm{GeV}}$. Including the effect of real light detectors worsens the statistical component of the energy resolution to approximately 5%. Figure 6.2 shows the fraction of energy detected in the scintillator for fully contained 200 MeV gamma rays after correcting for the effects of light attenuation in the WLS fiber and inactive material in the P0D.

Figure 6.3 shows the efficiency to reconstruct photons as a function of the Z position in the P0D (top plots), and direction (bottom plots). In these figures, the water target is located between

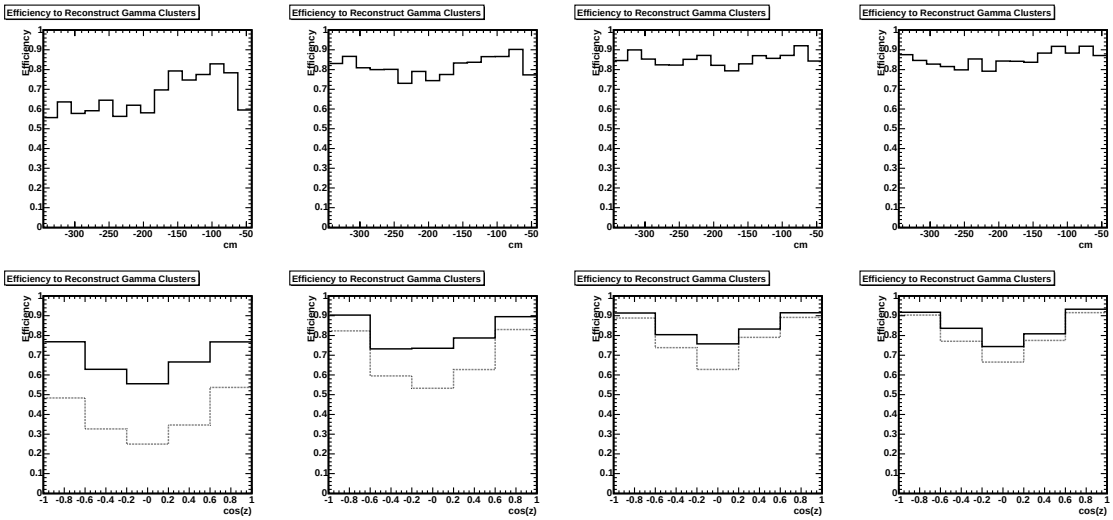


Figure 6.3: The top figures show the efficiency as a function of the Z position to reconstruct photons with 50 MeV, 100 MeV, 200 MeV and 400 MeV of energy inside the P0D. The bottom figures show the efficiency to reconstruct photons as a function of the photon direction. The solid histograms show the efficiency to reconstruct photons using a specialized photon tracking program. The dashed line shows efficiency to reconstruct a photon using standard tracking.

-170 cm and -340 cm. For photons with more than approximately 100 MeV the efficiency as a function of position is quite uniform, but the efficiency for 50 MeV photons drops to approximately 60% in the water target region while remaining above 75% in the carbon target region. The efficiency is also relatively uniform as a function of the photon angle, although the planar nature of the P0D give a moderate reduction perpendicular to the neutrino beam direction.

### 6.1.2 $\pi^0$ reconstruction

Figure 6.4 shows two examples of $\pi^0$ events as simulated in the P0D. The left figure shows an X and Y projection of a neutral current $\nu_\mu + p \rightarrow p + \pi^0$. The proton track, and the $\gamma$-rays from the $\pi^0$ is clearly visible in both projections. The proton can be identified based on the charge deposition as a function of length, while the $\gamma$-ray tracks show a clear E&M shower signature. All tracks can be projected back to a single vertex within the detector which corresponds to the start of the proton track. The right figure shows an X and Y projection of a $\nu_\mu + n \rightarrow n + \pi^0$ event where the $\gamma$-rays from the $\pi^0$ are clearly visible. The $\gamma$-ray tracks can be projected back to a single position along the Z axis, and show a clear E&M shower signature.

Table 6.2 gives the efficiency to reconstruct the neutral current $\pi^0$ production rate which has been estimated using a sample of events preselected by the following criteria: 1) There must be at least one $\pi^0$ produced in the event. 2) There must be no muon or charged pion with more than 250 $\mathrm{MeV/c}$. 3) The event must have originated more than 25 cm from the edge of the P0D. These events are then reconstructed using automated algorithm and considered to contain a $\pi^0$ if: 1) There are at least two reconstructed tracks of any type. 2) At least two tracks start from different points. 3) The reconstructed vertex is inside the P0D. To calculate the final efficiency, the reconstructed vertex was required to be within 30 cm of the true vertex. The efficiency presented

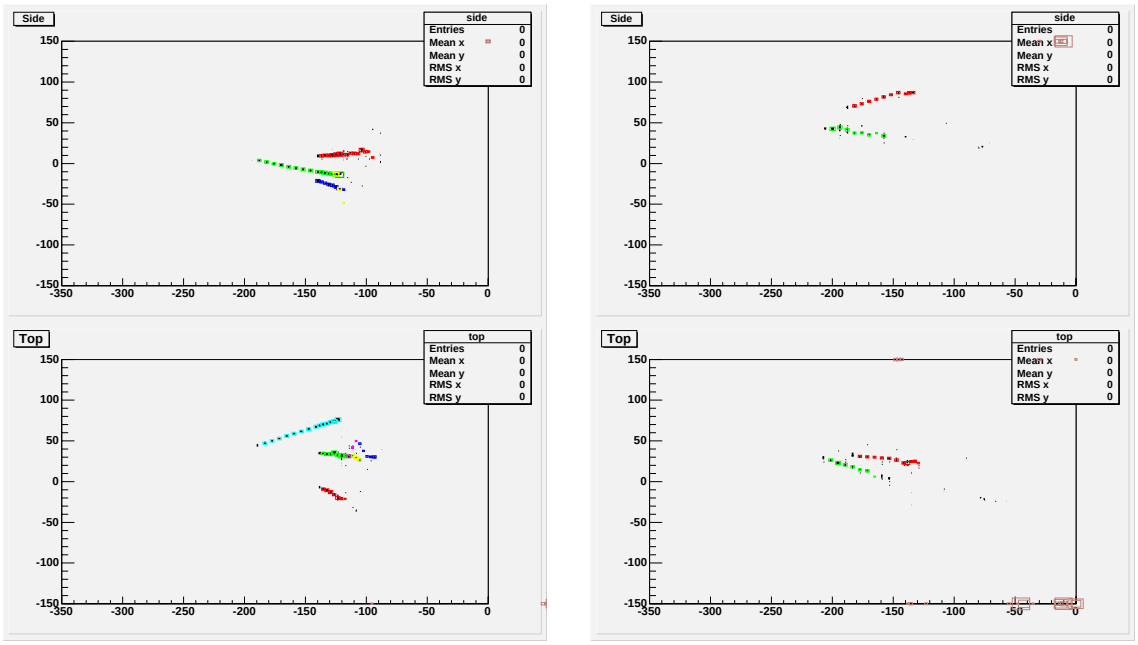


Figure 6.4: Typical neutral current single $\pi^0$ production events. The left panels shows a 983 MeV/c proton and a 495 MeV/c $\pi^0$. The right panels shows a single 473 MeV/c $\pi^0$ that was accompanied by a neutron. The upper (lower) panels show a projection of the Y-Z (X-Z) hits. The various colors (red, green, etc.) show the results of a track reconstruction applied to these events. The axes are labeled in centimeters.

| Momentum | Efficiency | Background |
|---|---|---|
| 200 – 300 $\mathrm{MeV/c}$ | 52% $\pm$ 3% | 18% |
| 300 – 400 $\mathrm{MeV/c}$ | 54% $\pm$ 4% | 19% |
| 400 – 600 $\mathrm{MeV/c}$ | 59% $\pm$ 4% | 22% |
| 600 – 800 $\mathrm{MeV/c}$ | 47% $\pm$ 6% | 8% |
| $>$ 800 $\mathrm{MeV/c}$ | 62% $\pm$ 4% | 7% |

Table 6.2: The efficiency and background to reconstruct neutral current $\pi^0$ events.

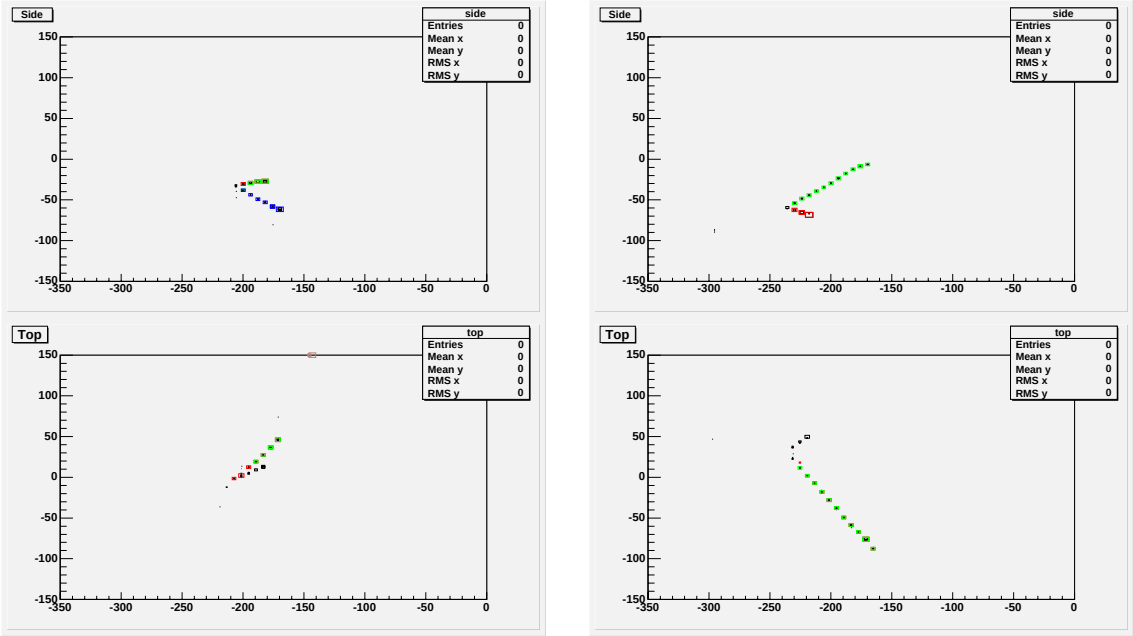


Figure 6.5: The left panel shows a quasi-elastic neutrino interaction with a 275 $\mathrm{MeV/c}$ muon and a 690 $\mathrm{MeV/c}$ proton. The right panel shows a quasi-elastic interaction with a 420 $\mathrm{MeV/c}$ muon and a 696 $\mathrm{MeV/c}$ proton. The colors represent the result of pattern recognition applied to these events. The axis is labeled in centimeters.

in Table 6.2 is consistent with a uniform $\pi^0$ reconstruction efficiency of 55%$\pm$5%.

### 6.1.3 Charged particle reconstruction

Figure 6.5 shows two typical quasi-elastic neutrino events as measured in the P0D. The P0D has not been optimized to measure events containing only heavy charged particles, but contains a large fully active target. In fact, the target mass for the P0D will be significantly larger than that of the FGD detector. For this reason, the P0D will provide an excellent verification of measurements made with the much more precise FGD+TPC combination, and can provide access to processes with small partial cross-sections.

## 6.2 Plastic scintillator and mechanical structure

The P0D is a solid scintillator strip detector using water to provide a large oxygen content and is based on K2K SciBar experience and MINER$\nu$A design. The P0D target is constructed of water layers between X-Y scintillator modules which provide the charged particle tracking. The scintillator modules are constructed with a 22% lead by mass so that $\gamma$s have a high probability of creating an electromagnetic shower. The P0D has a total target mass of approximately 14 tons and a fiducial mass of approximately 6 tons.

Figure 6.6 shows the schematic view of a P0D target. The tracking layers consist of X and Y extruded scintillator planes (white) with a 0.6 mm foil (red) sandwiched between them. The scintillator planes are made light tight with layers of mylar on the large faces (not shown), and end

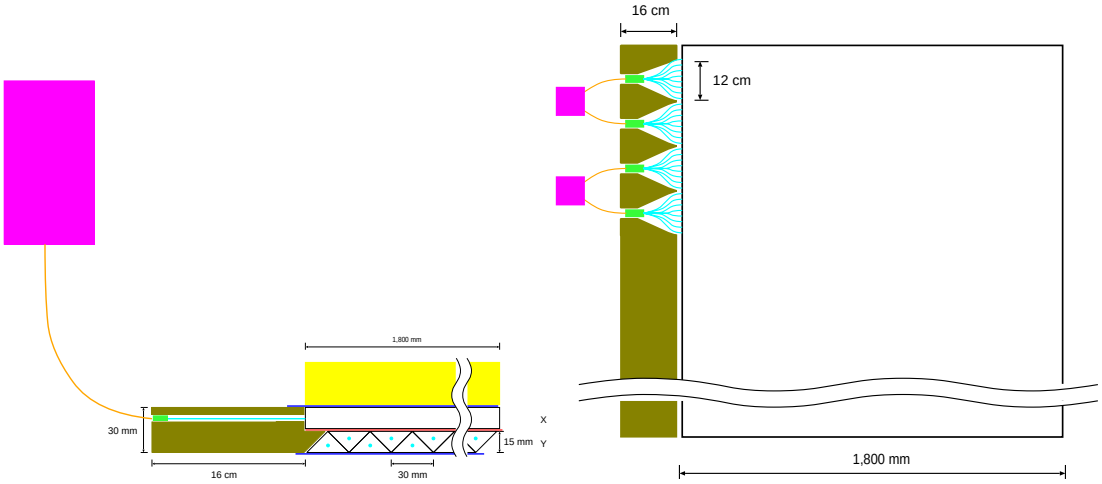


Figure 6.6: The schematic view of a P0D layer. Left and right figures show side and top views, respectively. White shows extruded scintillators; red shows lead foil; yellow shows water cell or polypropylene plate; dark green shows end-cap; light blue shows WLS fibers; green shows optical connector; orange shows clear fibers; magenta shows PMT boxes.

caps (dark green). The end caps serve the dual purposes of providing a manifold to bring WLS fibers (cyan) out of the scintillating bars, and keeping the ends of the scintillator light tight. A water cell is placed between half of the scintillator modules to provide oxygen target. Figure 6.7 shows the schematic view of the assembled P0D layers.

The water cells consist of semi-flexible pillow bladders, nominal dimensions 3 cm $\times$ 1.8 m $\times$ 2.1 m, holding about 100 kg of water each. They are provided with fill tubes at top and drain tubes at bottom. The drain tubes will run through a simple manifold outside the magnet, and thus serve as sight tubes for checking water levels. The bladders are made from rubberized cloth or polyethylene-coated EVAL plastic. Similar in construction to inflatable boats or industrial fluid storage bladders, such bags have a well-established engineering history of toughness and long-term reliability. (Similar bags have been used for decades to waterproof balloon flight packages in Japan, where scientific balloon flights typically land in the sea.) The proposed budget includes prototypes for testing, and spares.

Figure 6.8 shows a plan view of the whole P0D detector. The size of the target volume is 1.8 m $\times$ 2.1 $\times$ 3.3 , which is obtained by minimizing the space needed (35 cm in thickness) for PMT box mounting and clear fiber routing. The PMTs and front-end boards are installed in boxes for optically shielding.

### 6.2.1 Extrusion of the scintillator strips

Particle tracking is done using extruded scintillators similar to that used in the K2K SciBar detector and is in the MINER$\nu$A design. The P0D design calls for triangular scintillator bars that are 1.5 cm in height and 3.0 cm in base that are co-extruded with a $TiO_2$ surface treatment (see Figure 6.9). The bar length is 1.8 m for an X-plane and 2.1 m for a Y-plane. Each scintillator module is constructed from 120 (140) bars oriented in the X (Y) direction and there are a total of 76 scintillator planes in the baseline design. In total we have 19,760 scintillator strips. Each scintillator module is optically shielded by mylar and four end-caps. We expect the scintillator will be

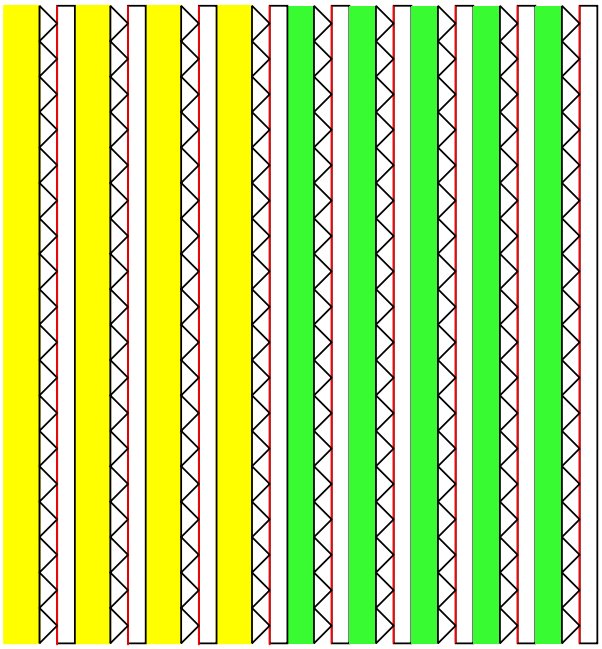

Figure 6.7: The schematic view of assembled P0D layers. White shows extruded scintillators; red shows lead foil; yellow shows water cell; green shows polypropylene plate

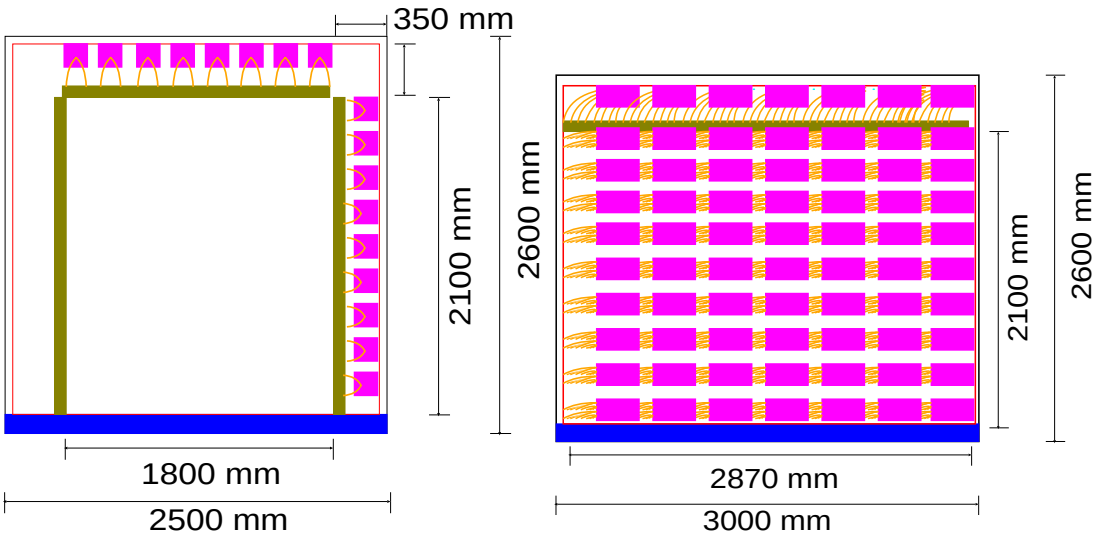


Figure 6.8: The schematic view of the P0D. Right and left figure shows front and side view, respectively. Pink shows PMT box; dark green shows end-cap; blue shows support structure; orange shows clear fiber.

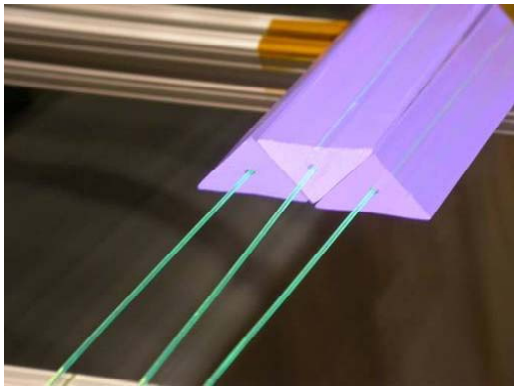

Figure 6.9: Prototype MINER$\nu$A scintillator bars with WLS fibers. The size of each bar is 33 mm in base and 17 mm in height. The P0D will use bars with similar size and shape, but with a co-extruded $TiO_2$ surface treatment.

produced by the northern Illinois Center for Accelerator and Detector Development (NICADD) at Northern Illinois University (NIU). NIU physicists and mechanical engineers have formed a collaboration to support development of the next generation of detectors at the Fermilab Scintillator Detector Development Laboratory (FSDDL). NICADD and Fermilab have significant scintillator extrusion experience and are expected to produce MINER$\nu$A triangular bars, which is similar to our design. The quantity of scintillator required by the P0D is well matched to the FSDDL production capacity. An important point in producing extruded scintillators is the development of the die used to shape the final scintillator cross-section. A triangular die has been developed by MINER$\nu$A similar to that required by the P0D. The scintillator strips are made of polystyrene doped with PPO (1% by weight) and POPOP (0.03% by weight) and co-extruded with a reflective coating of $TiO_2$. The total 7.2 tons of extruded scintillators included in the full P0D design will require a production run of approximately six weeks.

### 6.2.2 Optical readout of the P0D

Wavelength shifting (WLS) fiber (Kuraray Y11) is inserted into the hole of each scintillator strip. The light will be read out from only one end of each fiber. In K2K SciBar and MINER$\nu$A, 1.2 mm and 1.5 mm diameter fibers have been tested. 1.5 mm fibers deliver more light than 1.2 mm fibers; however, we use 1.2 mm fibers which have a smaller bending radius, because the available space for the P0D is limited. To increase the light collection, unread end of each fiber is mirrored. Mirroring consists of polishing the end to be mirrored, depositing a 99.999% chemically pure aluminum reflective surface on the fiber, and with a coat of epoxy.

The WLS fibers are connected to clear fibers using an optical connector from Fujikura/DDK. This connector was originally developed for the CDF Plug Upgrade by DDK, in consultation with Tsukuba University and has been used by several other experiments. Figure 6.10 shows the DDK connector embedded in a boot that was developed by the MINER$\nu$A collaboration. The DDK connector consists of a ferrule, clip, and box. They snap together without screws or pins. Bundles of eight WLS fibers will be connected to a single DKK connector. The remaining light collection system consists of clear fiber bundles which take the light from the scintillator module to the PMT box, and a clear fiber "pigtail" which distributes the light to individual PMT pixels inside of the

Figure 6.10: The DDK optical connector with light-tight boot made for MINER$\nu$A.

PMT box. The clear fiber cables are kept light-tight by an opaque sheath. There is an RTV silicon rubber boot around the end of the sheath and connector to maintain a light-tight seal. This has been proto-typed and tested for MINER$\nu$A. This DDK connector is installed in the end-cap (dark green in Figure 6.6). WLS fibers and scintillators are fully light-shielded. The thickness of the end-cap is 16 cm which is determined by the bending radius of the WLS fibers (10 cm). The other end of the clear fiber cables are inserted into an acrylic cookie for connection to a PMT in the PMT box.

### 6.2.3 Assembly of P0Dules

The P0D modules are assembled from an X and Y plane of scintillator. To assemble an X-plane, we put 70 triangular bars (base down) on a frame-table. After applying glue to the upper faces of these bars, we place a second set of bars (base up) on top of the first. We assemble Y-planes in the same way as X-planes. The X-plane, lead foil, and Y-plane are glued together one by one, and we attach end-caps to the sides of the layer. After the scintillator and end-caps are assembled, WLS fibers with optical connectors are inserted into all the scintillator strips in the layer and the layer is fully light-shielded by closing the end-caps. Assembled layers are tested to assure the quality of the light shield, WLS fibers, and optical connectors.

After the modules have been fully assembled, the energy response as a function of position will be scanned using a $^{137}$Cs source mounted on a movable frame. Approximately 10 measurements will be taken along each fiber so that the attenuation can be accurately determined.

After assembly and quality control, all modules, water cells and polypropylene plates will be shipped to J-PARC for installation into the ND280 off-axis detector. Installation will be done one module at a time by lifting it into a pre-installed support structure inside of the magnetic coil. The PMT boxes are then installed around the outside of the P0D. After all of the modules and PMT boxes are installed, we connect clear fiber bundles to the optical connectors in the end-caps and PMT boxes which are attached at a support frame. This procedure is very similar to that used to install the K2K SciBar detector.

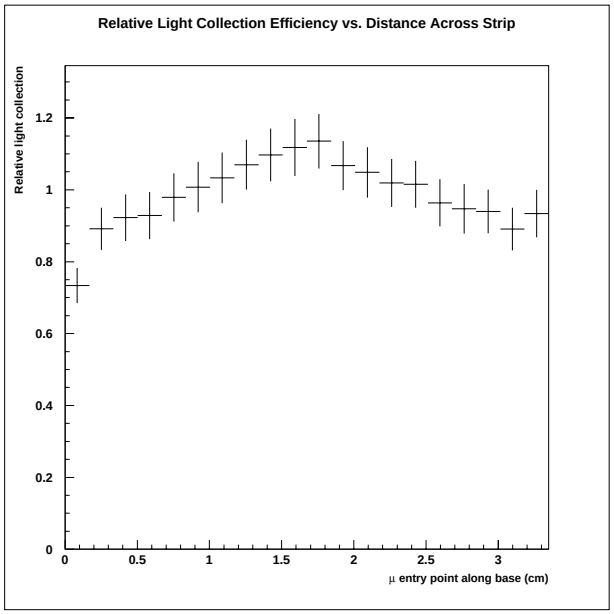


Figure 6.11: The relative light level as a function of muon entry point across the base of 3.3 cm$\times$1.6 cm triangular scintillating bar.

### 6.2.4 Expected Light Yield for a MIP

Since the P0D detector has been designed to be very similar to the K2K SciBar detector and MINER$\nu$A, we use the measured performance of these detectors to estimate the expected P0D light yield. The P0D bars will be instrumented using WLS fiber that is read on one end using a MCP-MAPMT, the uninstrumented end will be mirrored.

The SciBar detector used for the K2K experiment is made of scintillator bars read by a wavelength shifting (WLS) optical fiber. Each scintillator has dimension of 2.5 cm $\times$ 1.3 cm $\times$ 300 cm. Only one end of the fiber is read by a MAPMT, and the opposite end is not mirrored. The observed light yield at the center is 10.8 $\mathrm{pe/MIP/cm}$ with a 1.5 mm Kuraray Y11(200) WLS fiber that is 3.5 m long. Without accounting for mirroring, assuming a linear relationship between fiber diameter and correcting for the relative efficiency of the SciBar MAPMT and the proposed MCP-MAPMT, the light yield in the center of the P0D is estimated to be 8.0 $\mathrm{pe/MIP/cm}$ (this includes corrections for the clear fiber and the optical connectors).

The MINER$\nu$A experiment uses triangular scintillator bars with a similar dimension as proposed for P0D: 3.3 cm (base) $\times$ 1.6 cm (height). The WLS fiber is 1.2 mm in diameter and is made of s-35 multi-clad Kuraray fiber with 175 ppm Y11. The MINER$\nu$A collaboration conducted a light yield test with 3.5 m WLS fiber without aluminum coating on the far end. The average light yield was measured using cosmic ray muons and was found to be 6.3 $\mathrm{pe/MIP/cm}$. The light yield as a function of the muon crossing point across the base of the scintillator was also measured (see Figure 6.11). The yield is found to vary uniformly with the crossing position such that the total light collected by a scintillator layer remains nearly constant.[1] Applying corrections similar to those described above for the SciBar, this corresponds to 5.2 $\mathrm{pe/MIP/cm}$.

[1] A particle crossing a layer of scintillator will intersect two scintillating bars. The variation in the response of the two bars nearly cancel so that the response of the scintillating layer is nearly constant.

Based on the relatively low light yield expected based on the SciBar and MINER$\nu$A measurements, we propose to mirror the P0D WLS fibers. This will increase the light yield at the center by approximately 50%, but also flattens the response over the length of the bar. Using light yield measured in the MINER$\nu$A cosmic ray test, we expect that the P0D light response will vary between 7.3–9.2 $\mathrm{pe/MIP/cm}$. This increases to 11.3–14.1 $\mathrm{pe/MIP/cm}$ for the SciBar measured values. The expected light yield for a P0D layer then is between 11 pe and 21 pe. This is sufficient light yield for our purpose.

## 6.3 Photosensors and electronics

### 6.3.1 MCP MAPMT and alternatives

Since P0D will be placed in a magnetic field of 0.2 T, there are three options to take: (1) a photo-sensor that works in such a magnetic field, (2) a photo-sensor that works in a much weaker magnetic field reduced by a magnetic shield, and (3) a photo-sensor that works only in a very weak magnetic field with longer optical fiber to be placed outside of the magnet.

The last option is not practical as there is not enough space to install optical fibers, photo-sensors and front-end electronics. With this option, because of required longer optical fiber length, the mount of light at the photo-sensor will be much less.

In the following, we will describe our baseline option.

**Baseline photo-sensor** As briefly described in the introduction, our first choice for the photo-sensor is one that works under a magnetic field of 0.2 T. There are more than one candidates for the photo-sensor that can satisfy this condition: Micro-Channel-Plate Multi-Anode Photo-multiplier Tube (MCP-MAPMT), Silicon Photo-Multiplier (SiPM), and Avalanche Photo-Diode (APD), Hybrid Photo-Detector (HPD), and Fine-Mesh Multi-Anode PMT (FM-MAPMT). HPD and APD have too low a gain for our requirement of at least $10^5$. While SiPM technology is maturing rapidly, it has not been proven in mass-production. A commercially available FM-MAPMT has an inconvenient anode structure for us ( 0.8 mm wide and 26.5 mm long). Therefore, we have chosen the MCP-MAPMT as a baseline option.[2]

Burle is a leading company in MCP-MAPMT technology and manufactures 64 channel MPC-PMT. It is proven to work in a magnetic field of 0.2 T, and a typical gain is $6 \times 10^5$. It also has a nice single photo-electron (1 pe) resolution and produces very fast output signal. Figure 6.12 shows the output pulse height distribution for a 1-pe light signal for single anode version Burle 85001 and it provides a good single-pe resolution. Although we need only a modest timing information, this technology gives very fast output signal as in Figure 6.13, which is for 4 anode version Burle 85001-501. This property could be useful for particle identification and find the direction of a track.

Two potential drawbacks are : (1) a long deadtime as long as a few ms for a pore in micro-channel plate, and (2) degradation of the gain after a certain integrated anode charge (about 20% after integrated anode charge of 1-2 mC/cm$^2$). According to preliminary estimates, the both drawbacks do not seem to be a problem for us as, unlike collider experiments, our event rate is small and the singles rate is dominated by noise.

[2]While we have chosen the MCP-MAPMT as our baseline photo-sensor, the P0D has been specifically designed to allow the use of other sensor technologies. In particular, the design is readily adaptable to SiPM should they prove practical.

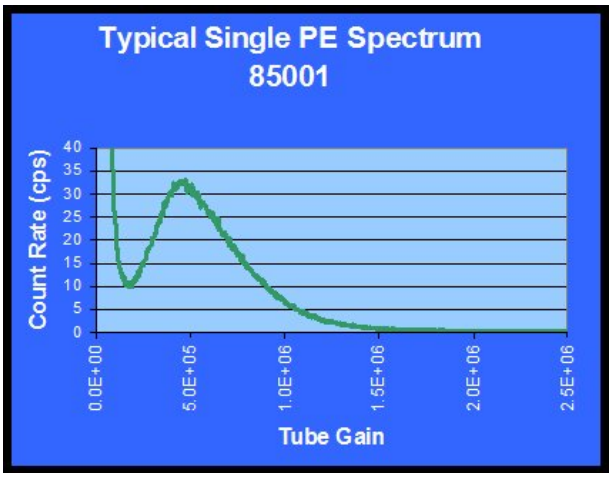


Figure 6.12: The charge distribution of a MPC-MAPMT for incident light at one photo-electron level.

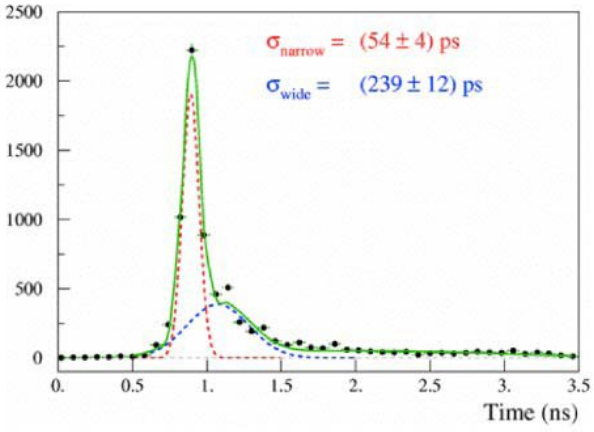


Figure 6.13: Transit time distribution of MPC-MAPMT output.

This technology also has a certain photo-electron collection inefficiency which is typically 60% compared with about 70% for a traditional MAPMT. The photo-electron collection efficiency for MCP-MAPMT is about 20% worse but this inefficiency is for the pore size of 25 $\mu m$ and Burle has been developing a version with the pore size of 10 $\mu m$ which should improve the collection efficiency.

The cathode and anode uniformity are typically 10% and 20% , respectively and these figures are similar to or better than those for traditional MAPMTs. Finally the cross-talk is expected be less than 1%.

We plan to conduct a series of tests of a Burle MCP-MAPMT 85011-501 with and without magnetic field.

### 6.3.2 Front End Electronics and LV distribution

Currently we have a workable design for the P0D detector electronics, mostly based on the MINERvA experiment electronics, assuming that we will use MCP-MAPMTs as the photo-sensors for the P0D. This is also used to cost the electronics budget presented in the budget section. The electronics design, however, cannot be finalized at this time because of the uncertainty in the choice of a photo-sensor that will perform satisfactorily in a 0.2 T magnetic field. Thus, at this time, the T2KUK collaboration and the T2K US B280 collaboration have agreed to collaborate in this project in order to come up with a final electronics design that is appropriate for the choice of photo-sensor and cost-effective. In the following we present the current baseline of the P0D electronics.

The P0D will have a total of 19,760 channels, from 309 MCP-MAPMTs, each with 64 independent anode channels serving individual scintillator bars. The data acquisition (DAQ) system must digitize pulse edge arrival times to within a few nanoseconds, and pulse charge to 0.25 photo-electron (pe) equivalent.

To reduce costs and eliminate the need for lengthy R&D, the P0D could adopt readout electronics components currently under development for MINER$\nu$A if the final choice of the P0D photo-sensor characteristics match the MINER$\nu$A electronics. The key elements of the MINER$\nu$A electronics design have already reached the advanced prototype stage, and successful cosmic-ray tests at Fermilab have demonstrated performance well-matched to the needs of the ND280. Design, fabrication and testing of production prototypes for both custom boards in the system (front-end digitizers, and VME readout modules) is supported as part of MINER$\nu$A's approved FY'05 R&D budget.

The front-end boards mounted outside the light-tight photosensor housings will digitize timing and pulse-height signals, provide high-voltage for the photo-sensors, and communicate with VME-resident readout controller modules over an LVDS token-ring. Pulse-heights and latched times will be read from all channels at the end of each spill. The cost of the proposed readout electronics and data acquisition system, including contingency, is approximately $25 per channel.

The front-end board is designed around the D0 TRiP ASIC, which is a redesign of the readout ASIC for the D0 fiber tracker and preshower. Its analog readout is based on the SVX4 chip design. Each TRiP chip supports 32 channels for digitization, but only half that number of channels for discrimination and timing.

The pre-amplifier gain is controlled by jumper and has two settings which differ by a factor of four. The gain of the second amplifier stage is controlled by three additional jumpers. The amplified analog signal goes into a pipeline 48 cells deep. To gain dynamic range, we will increase the input range of the electronics by passively dividing charge from a single pixel among two TRiP

analog channels with a ratio of a factor of 10. The "high range" channel, then, will allow energy depositions many times greater than minimum ionizing to be recorded without saturation. Each TRiP channel will be digitized by a 12-bit ADC.

Only one of every two input channels to the TRiP chip has a latched discriminator output useful for timing information. The lower range channels will feed the latch whose output is presented to an FPGA. With appropriate firmware, internal logic of the FPGA can be used measure timing with a granularity of 5 ns. To measure the time of the latch firing accurately, a 25 MHz reference clock is multiplied by four in a PLL and phase shifted by 90 deg to form a quadrature clock that is used inside the FPGA to form a digital TDC with least bit resolution of 2.5 ns. This feature has been tested on the prototype board and timing resolution better than 2.5 ns least count has been achieved. The reset time for the latch is only 15 ns, so inside a spill the latch will be in the ready state by default. After the signal exceeds a threshold and the latch fires, it is reset incurring minimal dead-time.

Each board includes its own high-frequency phase-locked oscillator, which provides a local clock signal for the FPGA logic. Global synchronization is provided using an external counter-reset reference signal distributed over the LVDS interface from the VME readout boards once every second, and originating with a timing module which is, in turn, synchronized to the beam.

A resonant mode Cockroft-Walton high-voltage generator, mounted on a daughter card, will provide power to each board's PMT. The daughter-card design will allow a malfunctioning high-voltage supply to be easily replaced without changing the main readout board. A controller based on the Fermilab RMCC chip will allow the PMT voltage to be monitored, adjusted or disabled under computer control, using the LVDS interface to the board.

The internal behavior of the front-end board is supervised by an FPGA operating as a finite-state machine, making the system programmable and highly flexible. The most mission-critical and demanding elements of the firmware (controlling the TRiP chip's buffering and TDC functionality) have already been developed and tested, during commissioning of the first prototype in 2004. Logic to interpret commands and exchange data over the LVDS interface, and control the on-board Cockroft-Walton high-voltage supply has since been written and is now being tested. Persistent storage for the firmware is provided by an onboard flash PROM, which is read by the FPGA on power-up and can be re-written under computer control. As such, it will be possible, if necessary, to reprogram the FPGA logic of all boards remotely, even after installation.

The front-end digitizer boards are daisy-chained into 27 LVDS token rings of 12 boards each. Both ends of a chain terminate in a custom built VME Chain Read Out Controller (CROC) module.

LVDS signals will be transmitted around a ring on standard, commercially-available fire-resistant and halogen-free CAT-5e network cable approved by for safe underground use. The LVDS chains will also be used to transmit configuration and slow-control messages to the cards.

### 6.3.3 Read out and control of the front end electronics

Each CROC module will control four LVDS chains, requiring a total of 7 CROCs (plus spares) for the entire detector. These modules will reside in a VME crate alongside a crate controller and a custom-built timing distribution module.

The readout controller modules have the following functions:

1. Prior to the arrival of a spill, as signaled by the VME-resident timing module, to reset the timing counters of each front-end board and open a 10$\mu$sec gate to collect data from the spill.

2. Upon completion of a spill, to initiate readout of front-end digitizer data over the four associated LVDS rings, into internal RAM.

3. Upon completion of the parallel readout of all four chains, to raise an interrupt with the main DAQ computer, indicating that event data is available. The PVIC/VME interface/crate controller allows VME interrupts to be received directly by the main computer.

4. The internal RAM of each CROC is memory-mapped to the host computer's PCI bus, allowing block transfer of event data via the PVIC/VME interface/crate controller. The relatively long machine duty cycle and low data rate ensures that no deadtime will be associated with the readout itself.

5. Once per second, to globally synchronize the detector's TDCs over LVDS using a high-precision refresh signal from the timing distribution module. The need for this synchronization drives the choice of LVDS for the readout chains, as opposed a less performing alternative such as Ethernet.

6. Upon command of the main data acquisition computer, to control and monitor the Cockroft-Walton high-voltage power-supplies on the front-end digitizer boards, and to configure the firmware of these boards at run-startup.

Communication between the main data acquisition computer will be via commercially available PVIC/VME link, allowing block data transfers to and from VME and interrupts to be received by the computer in response to the spill gate.

The main DAQ and slow-control computer will be located near the VME electronics, with high-speed TCP/IP links (one for data, one for monitoring and control messages) to the laboratory network. A relatively modest, dual-CPU server model will be more than adequate for our purposes. One CPU will be dedicated to real-time data acquisition, and the other will handle control messages and monitoring. An on-board, RAID-5 disk cluster with sufficient capacity to store several weeks of data will serve as a buffer for the data, pending transfer to offline processing nodes and permanent storage.

# Chapter 7

# The Electromagnetic calorimeter

## 7.1 Introduction

The purpose of the electromagnetic calorimeter (ECAL) is to capture and characterize electromagnetic energy produced by neutrino interactions in the inner detectors (the P0D, the FGD, and the TPC), primarily photons produced by the decay of NC- or CC- produced $\pi^0$. The ECAL also acts as an active veto detector, shielding the internal detectors from particles produced by neutrino interactions in the magnet or other surrounding material. The low energy of the T2K beam makes the detection of photons from neutrino-produced $\pi^0$ very challenging. However the fact that NC-produced $\pi^0$ are one of the two major backgrounds to the $\nu_e$ appearance measurement makes their characterization essential. The nature of the challenge can be seen as follows. Figure 7.1 shows the energy vs. angle distribution for photons arising from the decay of $\pi^0$ generated in the P0D. Two things are apparent—first, a significant fraction of the photons are very soft ($<$100 MeV, or even $<$50 MeV). Secondly, while the photons are not isotropic, they do occur at all angles, requiring what is essentially a hermetic ECAL for good efficiency. Figure 7.2 shows the energy of the first photon from a $\pi^0$ vs. the energy of the second, which makes the (perhaps rather obvious) point that if one of the photons is hard, the other tends to be soft. Since a quantitative observation of both photons is required to reconstruct a $\pi^0$, this fact drives the need for a very low energy threshold in the ECAL. If the minimum energy threshold for reconstructing a photon is $E_{min}$, then all events to the left and below $E_{min}$ in Figure 7.2 are lost. This is plotted in Figure 7.3, which shows the fraction of $\pi^0$ which survive as a function of $E_{min}$. Even if photons down to 100 MeV can be reconstructed, the efficiency is less than 30% (just from this one effect, not counting all other losses of efficiency). The situation improves somewhat, but not much, if you cut out the lowest energy $\pi^0$ (which would not mimic electrons in the interesting range in Super-Kamiokande). The same curve for a $\pi^0$ from the beam with a minimum energy of 200 MeV is also shown in Figure 7.3. Looking at these plots, if we want to reconstruct all the $\pi^0$, $E_{min}$ must be $\approx$50 MeV if this effect is not to eliminate most of the $\pi^0$ sample. Note that $E_{min}$ is the minimum energy where a photon can be successfully reconstructed, not the minimum energy where a few hits are observed.

## 7.2 Baseline Design

The electromagnetic calorimeter (ECAL) as it was originally conceived was a simple sampling calorimeter constructed from alternate layers of scintillating bars and lead alloy, and for this design

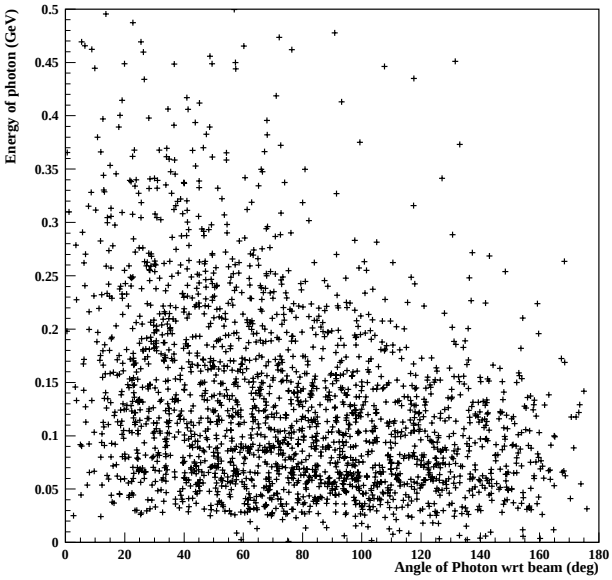


Figure 7.1: Plot of photon energy as a function of photon angle with respect to the beam direction for photons arising for $\pi^0$ decay in neutral current resonance and coherent interactions.

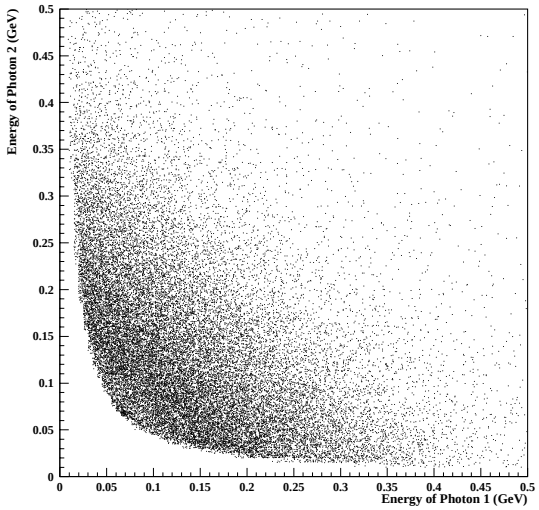


Figure 7.2: Scatter plot of the energy of the higher energy photon from $\pi^0$ decay vs. the energy of the lower energy.

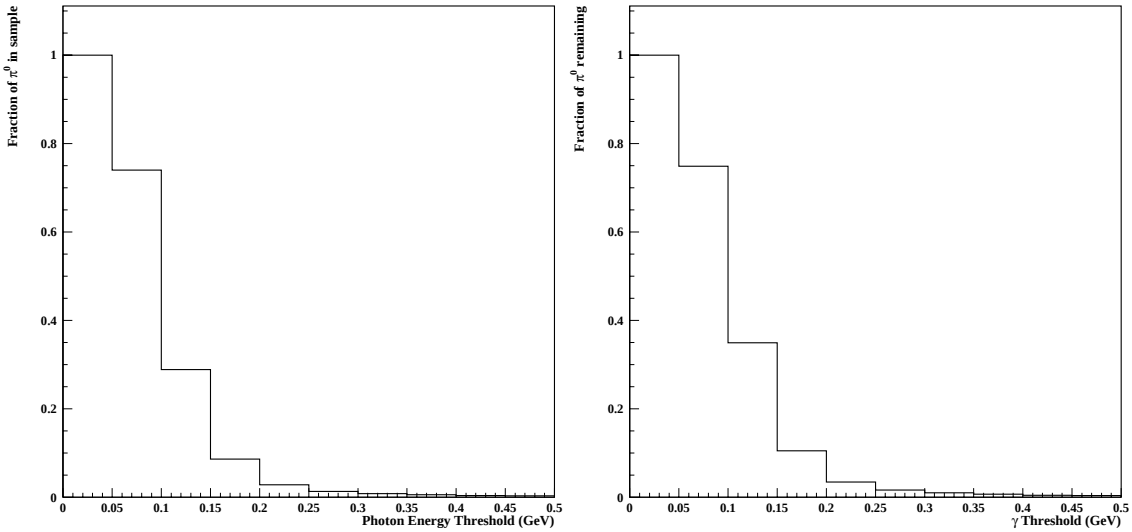


Figure 7.3: (Left) Fraction of $\pi^0$ events where both photons are above a threshold energy as a function of that energy for all $\pi^0$ created by the beam. (Right) Fraction of $\pi^0$ events for a minimum $\pi^0$ energy of 300 MeV.

the efficiency problem stated above is severe. In fact previous studies have indicated that a design with an all-plastic P0D detector surrounded by a monolithic set of ECAL modules could only reconstruct and identify neutral current $\pi^0$ events with an efficiency of approximately 10%. This low efficiency arises largely from two causes:

- Photons with energies of $\sim$ 100 MeV tend to Compton scatter in the low Z material of an all-plastic P0D, leading to either an electromagnetic shower which does not point back to the $\pi^0$ decay point, or else a discontinuous sequence of hits that cannot be identified as an electromagnetic shower.

- In approximately 40% of the events a photon leaves the P0D without interacting. These photons can propagate a few radiation lengths into the ECAL and are indistinguishable from background.

The prediction of a low $\pi^0$ reconstruction efficiency led to the current baseline conceptual design for the P0D and ECAL. First of all, as mentioned in the section on the P0D detector, high-Z material (Pb alloy sheets) has been added to the P0D to try to force the photons to convert. Secondly, we plan to add a "pre-radiator" section into the ECAL in an attempt to produce more elongated photon "showers" (at these relatively low energies photons have a very significant Compton scattering cross section, meaning that they do not "shower" so much as multiply scatter), which hopefully will provide more accurate tracking information. The basic components are 3 mm thick Pb alloy sheets and 1 cm thick $\times$ 5 cm wide plastic scintillator bars (with signal readout by optical fiber, as with most of the rest of the subdetectors in the ND280 detector). The "ECAL" section consists of 15 layers, each of which has one sheet of Pb alloy and one layer of scintillator bars. Interior to this section is the "pre-radiator" section, where each of the 3 layers consists of a sheet of Pb alloy backed by 3 layers of plastic scintillator bars. The orientation of the bars will be discussed below.

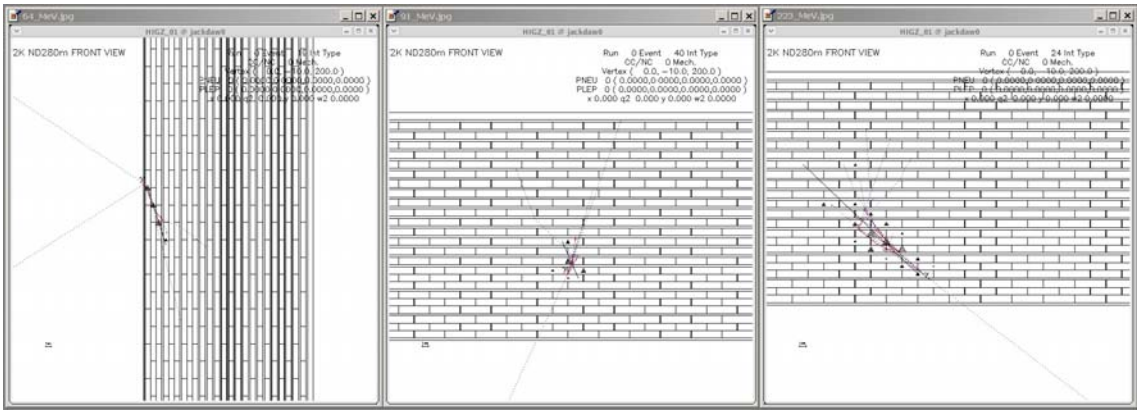


Figure 7.4: Hit patterns and reconstructed directions (solid lines) in ECAL for 3 selected (but reasonably typical) photons.

The problem we are trying to address is also shown in Figure 7.4, which shows a simulation of the energy deposition from three rather typical photons along with attempts to fit the photon direction by performing a simple weighted chi-squared fit to the hits. The first event is from a 64 MeV photon, which Compton scatters leaving a nice clean, easily reconstructed electron track in the detector which unfortunately points in the wrong direction. The second event, from a 91 MeV photon, shows a second common pathology for these low-energy photons: the photon converts into a localized "blob" of hits which do not yield much useful directional information. At higher energies, as shown by the third event (from a 223 MeV photon), well developed showers are seen which can be reconstructed (although, as shown above, in $\pi^0$ decay such a high-energy photon is usually accompanied by a low-energy photon that will be more difficult to reconstruct). One result of the combination of these effects is shown in the first panel of Figure 7.5, which shows the angular resolution in the plane perpendicular to the bars (the plane with the best resolution) for photons from $\pi^0$ decay as a function of the bar width. The resolution has an RMS of 24 degrees, which varies very little with bar width. This poor angular resolution makes it more difficult to do $\pi^0$ vertex reconstruction.

The ECAL conceptual design is still evolving, and none of the parameters of the proposed ECAL has been optimized. Nevertheless, it is useful at this point to consider a more detailed design to look for interferences with other systems and to get a rough estimate of costs. We will make various assumptions about geometry, etc., that need to be confirmed by further simulation and analysis. In our current design, with lead added to the P0D and pre-radiators in the ECAL, there is relatively little difference between these two subdetectors. Given this, rather than having ECAL modules transverse to the beam upstream and downstream of the P0D (and therefore inside the basket), it seems simpler to just increase the Pb/plastic ratio in the farthest upstream and downstream parts of the P0D. We also assume that extending the ECAL to surround the tracking region is desirable. This may assist in the measurement of $\nu_e$ beam background in the tracker, and as described in Appendix A might permit the identification of $\pi^0$ events in the tracker. We therefore assume that the ECAL must cover the sides and the downstream end of the basket.

The next question that must be answered is the orientation of the scintillator bars. It would greatly simplify the design and the placement of photosensors, and make it easier to achieve coverage of the entire solid angle, if all the bars could be oriented along the beam direction. Then all photosensors could be located at the ends of the detector and the ECAL could be mounted flush

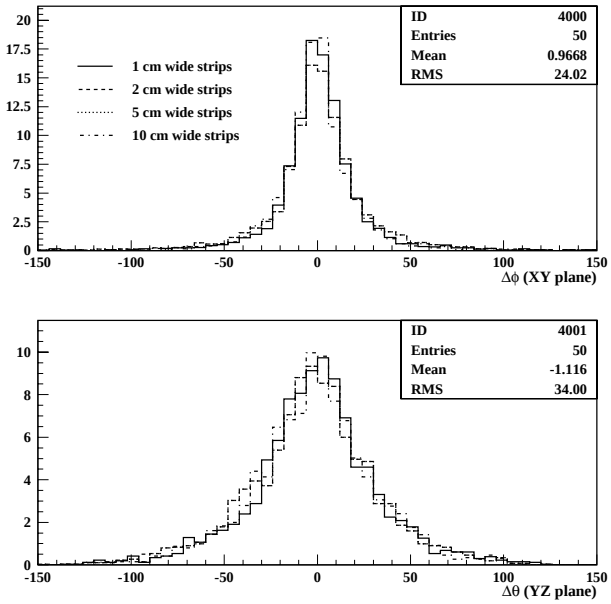


Figure 7.5: Angular resolution for double-ended readout from the ends, with an assumed error on the reconstruction along the bars of 10 cm (Gaussian sigma). The top panel shows the reconstruction in the plane perpendicular to the long dimension of the bars, while the bottom plot shows the reconstruction in the plane of the bars.

against the magnet (increasing the volume available to the basket and its contained detectors by, perhaps, as much as 20 cm on each side). In this design the track reconstruction in the XY plane is derived from looking at which bars are hit, while the track reconstruction in the Z plane is derived from measuring the position of each hit using time difference between readout at each end of the bar as demonstrated by Kudenko. A potential problem of this is seen in the second panel of Fig. 7.5, which shows the angular resolution when the (probably unrealistically optimistic) assumption is made that the hits can be located with a Gaussian RMS of 5 cm (on a bar of more than 6 m length, or in other words, better than 1% position resolution). Even with this optimistic position reconstruction, the RMS of the angular resolution is 34 degrees, making $\pi^0$ reconstruction even more problematic.

If this solution does turn out to be unworkable, the best alternative is probably to move to UV alignment of the bars (as shown in Fig 7.6). This arrangement has the advantage that all the bars are the same (shorter) length, (minimizing problems with photon attenuation), thereby perhaps allowing single-ended readout. It has the disadvantage that the photosensors must be deployed along the entire length of the detector, increasing the room needed and the construction complexity. This is sketched out in Fig 7.7, which shows the arrangement of the ECAL modules in the two schemes. Given that our current ECAL modules are only 30.7 cm thick, if we read out the bars from the ends of the magnet we could perhaps make the basket slightly larger. With side readout the basket is certainly not too small, and might even need to be made slightly smaller (although perhaps a bit longer). In both of these schemes there is another ECAL section downstream of the basket to catch forward going photons. Detailed design is needed, but for the moment it looks like this section would be slightly smaller in the end readout option than in the side readout option.

In terms of mechanical support for the ECAL, all ECAL sections would be fixed to the magnets and would open and close with them (so the top and bottom would be divided in half on the magnet

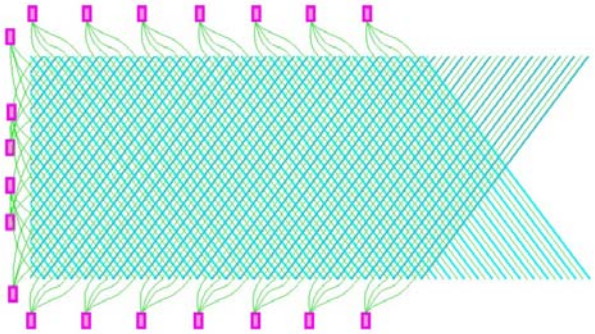

Figure 7.6: Sketch of the layout of the bars for a UV projection for ECAL. Readout could be either single-ended or two-ended with (hopefully) no additional space needed at the sides.

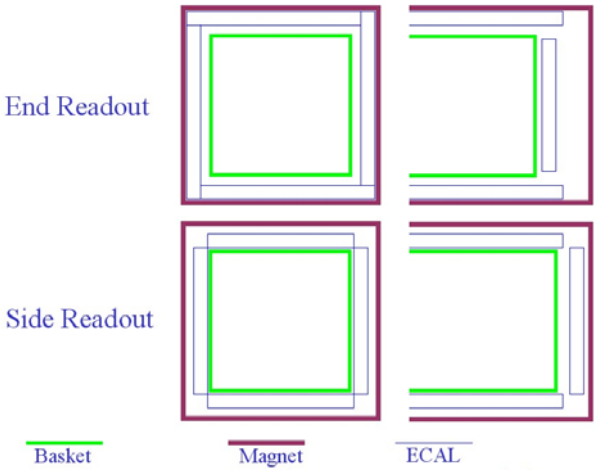


Figure 7.7: Layout of the ECAL modules for end and side readout. End readout produces a more hermetic layout that might allow the basket to be made bigger, but may not produce acceptable ECAL performance. The side readout is more complicated, and will require all the gap between the basket and magnet, but is safer from a detector performance point of view.

centre-line). The top would hang from the magnet (through the gaps in the coil), the bottom would sit on the magnet (once again through the coil gaps), while the side sections would be mounted on the magnet. Detailed engineering design of these supports is needed.

# Chapter 8

# The Muon Range Detector (SMRD)

## 8.1 Introduction

One of the main goals of the ND280 detector is the measurement of the neutrino energy spectrum. For charged current quasi-elastic (CC-QE) processes the neutrino energy is closely related to the muon energy. The neutrino energy can be reconstructed for CC-QE events using the muon momentum and its scattering angle if the Fermi motion is ignored. A full spectral measurement of the neutrino beam must include muons with large angles relative to the neutrino beam direction.

The ND280 detector (see Figure 2.1) will serve to measure CC-QE interactions. The target mass is largely concentrated in the FGD and the P0D, and the TPC will serve to measure muon momenta for forward muons. Muons which escape at large angles with respect to the beam cannot be measured by the TPC. However, these muons will intersect the iron yoke surrounding the entire detector, and therefore a muon's momentum can be inferred from its range by instrumenting the iron at various depths. We have performed a MC study to show the muon distributions across the various detector components. Muon vertices for muons originating from CC reactions are distributed throughout the FGD and P0D regions. Although precise numerical results depend on the precise assumptions about detector dimensions and fiducial volume, the following results can safely be used to define the average required SMRD performance.

The total fraction of muons from CC-QE reactions that is expected to intersect the SMRD amounts to nearly 40%. For CC non-QE reactions about 15% of all muons are expected to intersect the SMRD. A more detailed accounting of CC-QE and CC non-QE events is given in Table 8.1. Muon events are split into 4 different categories. Each event category is characterized by the detector components that the muon tracks intersect. The four categories are:

1. Events with muons that stop inside the FGD.

2. Events for which the muons escape in the forward direction and consequently intersect the TPC.

3. Events with muons that penetrate the FGD and TPC, then enter the SMRD.

4. Events for which the muon travels in the FGD and then only intersects the SMRD.

For each category in Table 8.1, the fraction of charged current quasi elastic (CC-QE) and non-quasi-elastic (Non-QE) events are specified. A significant fraction of muons are expected to be detected by the SMRD. Monte Carlo studies indicate that the mean momentum of the muons that

| | CC - QE | | CC non-QE | |
|---|---|---|---|---|
| | no. of events | ratio | no. of events | ratio |
| no. of events generated in FV | 7624 | | 6357 | |
| events stopping in FGD | 694 | 9% | 850 | 13% |
| events hit in TPC | 4017 | 53% | 4476 | 70% |
| TPC and SMRD | 2104 | 28% | 815 | 13% |
| FGD and SMRD only | 797 | 10% | 201 | 3% |

Table 8.1: Simulated muon acceptance for the conceptual ND280 detector configuration.

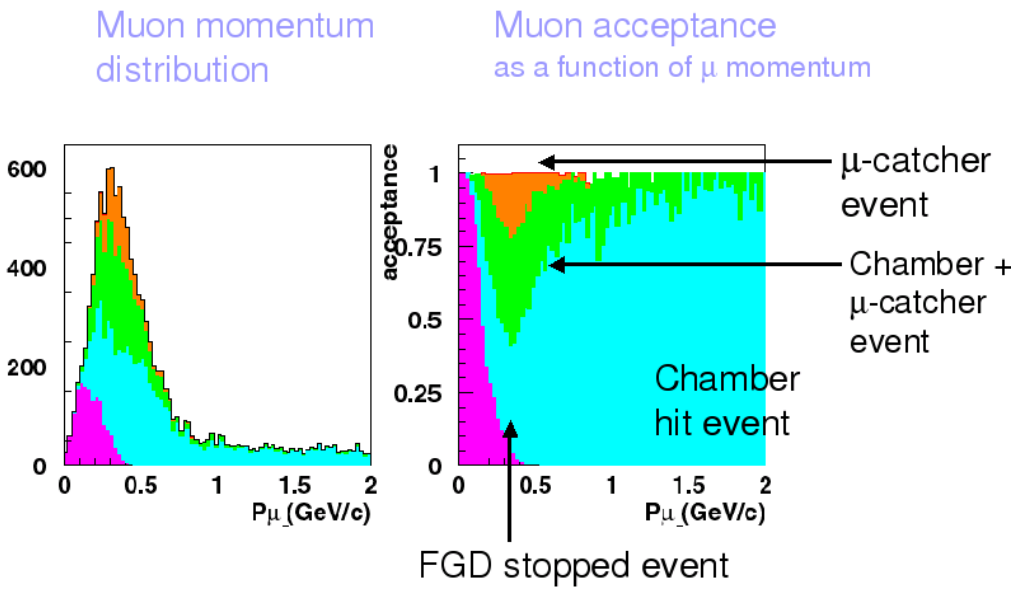


Figure 8.1: Muon momentum and momentum-acceptance distributions for the ND280 default design.

would have to be ranged out in the SMRD is on the order of 400 $\mathrm{MeV/c}$. The muon momentum and angular distribution as well as the muon acceptance distributions as function of muon momentum and muon angle are shown in Figures 8.1 and 8.2, respectively.

A fraction of the muons will intersect the TPC and the SMRD. For these muons the SMRD will significantly reduce the systematic uncertainties in the muon momentum measurement as provided by the TPC.

The SMRD will also serve to veto particles entering the detector from outside, and secondary particles from beam neutrino interactions in the iron of the magnet yokes, by the use of timing information.

## 8.2 Detector Requirements

The iron yoke consists of 16 C-shaped elements. One of these C-elements is shown in Figure 3.5. Each C is made of sixteen 5 cm thick iron plates, with 1.7 cm air gaps between the plates, and is

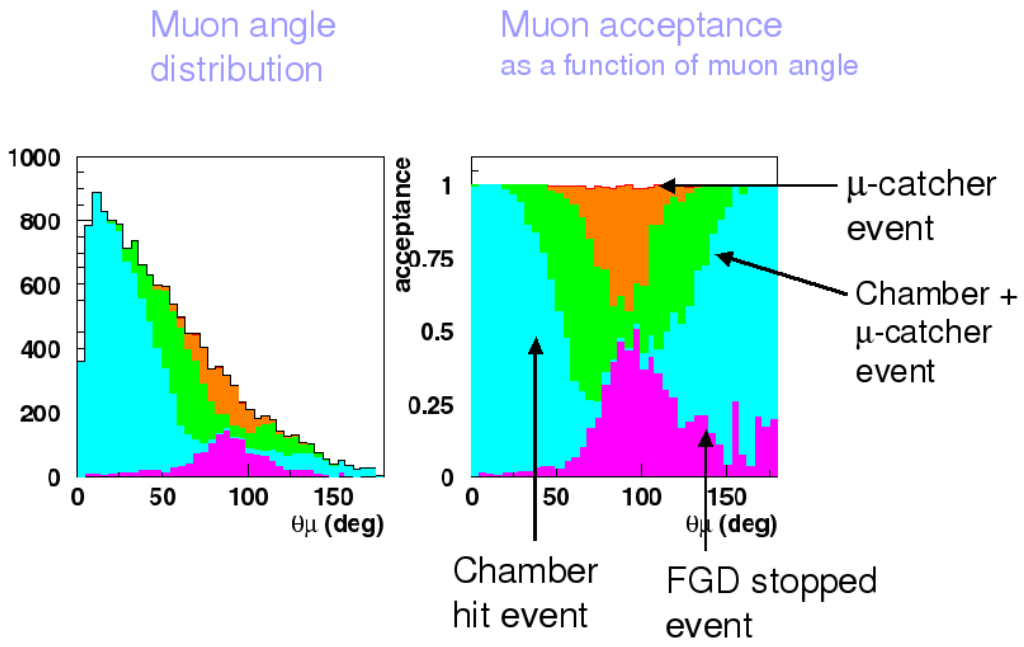


Figure 8.2: Muon angle and angle-acceptance distributions for the ND280 default design.

segmented in 12 azimuthal sections. To build the SMRD, the air gaps (88$\times$ 80$\times$1.7 cm) will be equipped with particle detectors.

The muon momentum distribution for CC-QE interactions that hit the SMRD is shown in Figure 8.3. The vast majority of large angle muons, namely 91% of all muons not escaping in the forward direction (e.g. $\cos\theta < 0.8$ ) have momenta of less than 600 $\mathrm{MeV/c}$.

Figure 8.4 shows an average energy slant depth relation for muons which were sampled from a flat angular distribution and an energy spectrum from 0 to 1 GeV which has been weighted according to figure 8.3. The slight rollover at muon energies around 1 GeV is due to the low flux for energies above 1 GeV. As can be seen in Figure 8.4 muons with energies less than 600 $\mathrm{MeV}$ will range out within less than 35 $\mathrm{cm}$ of iron. Since the iron plates in the previously described yokes (Section 3.4) are approximately 5 $\mathrm{cm}$ thick it would be sufficient to instrument 6 to 7 radial layers in order to completely range out 95% of all muons that are not escaping in the forward direction. Table 8.2 lists the range of muons in iron and the corresponding number of layers as functions of energy, along with the fraction of muons that is represented. First energy resolution estimates from a crude GEANT 3 based Monte Carlo study are shown in Figure 8.5. This Monte Carlo assumed a set of 5 $\mathrm{cm}$ thick parallel iron plates onto which a sample of 200 $\mathrm{MeV}$ to 1 $\mathrm{GeV}$ muons impinge at angles in the range from 0 to 90°.

The study indicates that a muon energy resolution of less than 10% can be achieved. As expected, the energy resolution is best for muons emitted at large angles (e.g. perpendicular to the beam direction) and worsens for muons emitted at smaller angles with respect to the beam direction.

In order for the ND280 detector to reliably identify CC-QE interactions and identify background events originating from the cavity and the iron yokes themselves, the SMRD is required to identify minimum ionizing particles (MIP) with very good efficiency. Hence the active detector medium has to provide uniform and high light yield. It is also desirable to have good inter-layer

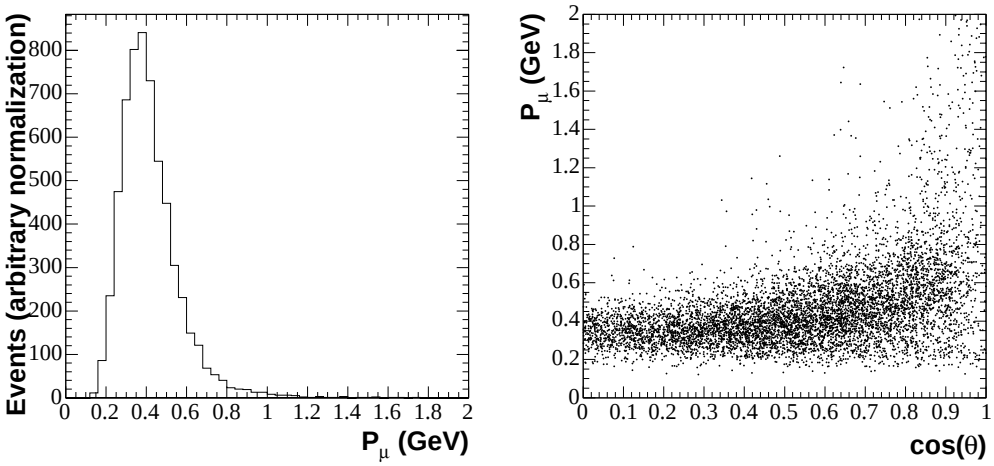


Figure 8.3: Left plot: muon momentum for CC-QE muons reaching the SMRD with $\cos\theta < 0.8$. Right plot: muon momentum for CC-QE muons reaching the SMRD versus $|\cos\theta|$.

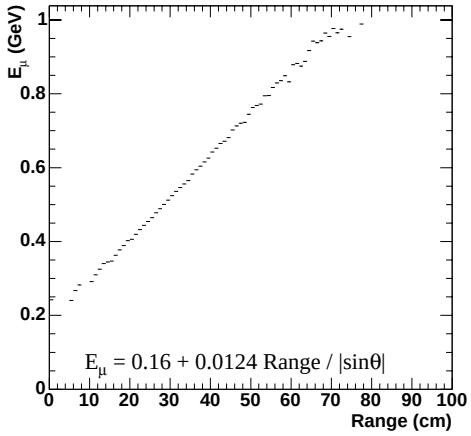


Figure 8.4: Relation between muon energy and range in iron as seen in data from Monte Carlo study [56].

| $P_\mu^{max}$ (GeV) | $f(\%)$ | Range (cm) | Layer |
|---|---|---|---|
| 0.5 | 79 | 24 | 5 |
| 0.6 | 91 | 31 | 6 |
| 0.7 | 96 | 37 | 7 |
| 0.8 | 98 | 44 | 9 |
| 0.9 | 99 | 51 | 10 |
| 1.0 | 99 | 57 | 12 |
| 1.1 | 100 | 65 | 13 |

Table 8.2: Maximum detected muon momentum and corresponding fraction $f$ of muons originating from CC-QE reactions with $|\cos\theta| < 0.8$. The penetration depth in iron and the corresponding number of layers in the SMRD are specified in the two right-hand columns.

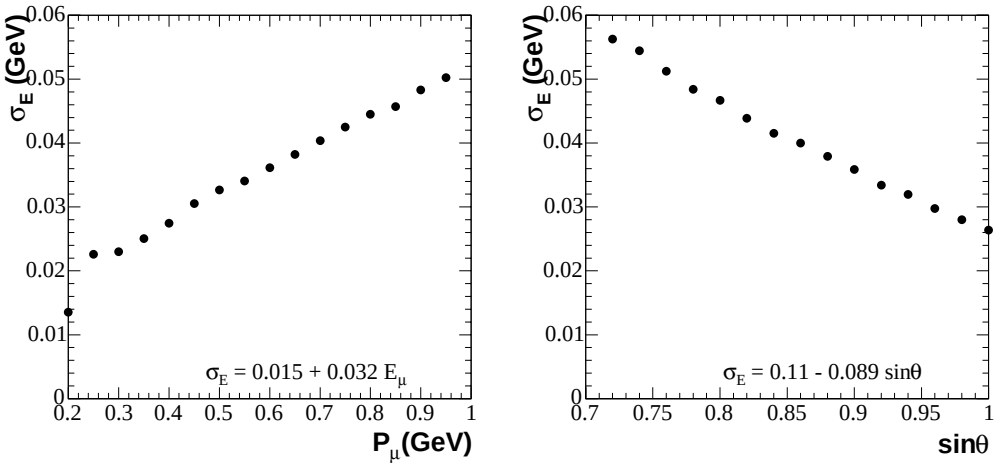


Figure 8.5: The muon energy resolution as function of muon momentum (left) and as a function of angle with respect to the beam (right) [56].

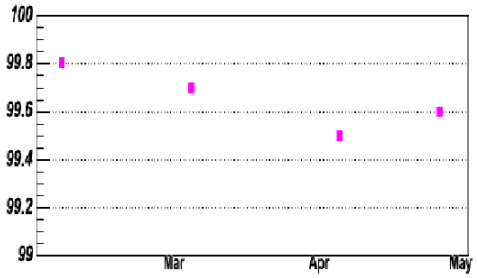


Figure 8.6: The MIP detection efficiency (in %) as function of calendar month for a prototype of scintillator with embedded WLS fibers. The fiber spacing for this prototype is 2 cm.

timing resolution to distinguish inward- from outward-going particles.

The neutrino beam will consist of 8 bunches with a time spread of about 60 $\mathrm{ns}$ each and a separation of about 360 $\mathrm{ns}$ between bunches. In order to clearly identify events with individual bunches in the beam, a time resolution of at least some tens of nanoseconds is required. However, more stringent timing is required in order to resolve events times within a bunch, achieve good position resolution, and obtain directional information. The final scintillator segmentation and the electronics and timing requirements will be defined on the basis of detailed Monte Carlo studies and test measurements currently in progress.

### 8.2.1 Detector Design and Technology

The baseline detector technology was chosen based on its ability to satisfy the minimum physics requirements, reliability, cost effectiveness, and availability.

**Scintillators and Wavelength Shifting Fibers** The active component of the SMRD will consist of slabs of 1 $\mathrm{cm}$ thick plastic scintillator. The scintillators will be sandwiched between the iron plates of the magnet yokes. Equidistant wavelength shifting fibers will be embedded into the scintillators in order to achieve good light yield and consequently high detection efficiencies of traversing minimum ionizing particles (MIP). Figure 8.6 shows the MIP detection efficiency for a prototype scintillator-WLS configuration as function of calendar month. The slope is not significant since the uncertainty on each data point is about 0.2%.

The WLS fiber will also serve to guide the light into the photo-detectors. The fibers can be read out on both sides or mirrored on one side and read out from one side, with the choice depending on the light yield. The scintillators will be coated with a chemical reflector to enhance the light yield. Similar combinations of scintillator slabs and WLS fibers have been used as muon or photon veto detectors in other experiments such as ZEUS [60], KOPIO [57], and E949 at BNL [58]. Furthermore, extensive R&D of this technology has been carried out for the SSC [61]. Figure 8.7 shows a $87\times17\times1$ cm slab of extruded scintillator with grooves for future insertion of WLS fibers. The left and right panel show the plastic before and after the application of a chemical reflector coating. The grooves are spaced at 2.5 $\mathrm{cm}$. The WLS fibers will be bend inside the scintillator with a radius of 3 cm to allow the fibers to exit parallel to the gap in between iron yokes. This setup aims to minimize the mechanical exposure of the sensitive fibers inside the inter-yoke gaps and naturally prevents the fibers from being buckled. For soft, 1 mm diameter multi-clad fibers

Figure 8.7: The left and right panel show a 87 $\mathrm{cm}$ long, 17 $\mathrm{cm}$ wide, and 1 $\mathrm{cm}$ thick scintillator with grooves to embed WLS fibers. The spacing between the grooves is 2.5 $\mathrm{cm}$. The scintillator shown in the right panel is coated with a chemical reflector.

(e.g.Y11) a bending radii larger than 1 cm does not represent a problem.

Figure 8.8 displays preliminary results from light yield measurements in response to traversing MIPs of a scintillator with embedded WLS fibers similar to the one shown in Figure 8.7. The very good timing characteristics of the scintillator-WLS fiber detector can be seen in Figure 8.9 which displays the time resolution of MIP signals as function of calendar month.

An alternative to the baseline design would be a slightly modified technology. A combination of extruded scintillators with embedded WLS fibers coupled to wavelength shifter bars or light guides is conceivable. The advantage would be to minimize the risk of fiber damage due to bending or interference with cables in the gaps between individual iron yokes. The wavelength shifter bars or light guides are more robust than the fibers. This option would come with the disadvantage of an additional interface which is estimated to cause a 10% light loss.

**Photosensors** Currently two readout options of the WLS fibers are considered. First, bundles of fibers will be read out by conventional but magnetically shielded multi-anode PMTs (MA-PMTs) or micro-channel plate photo-multiplier tubes (MCP-PMTs) which will be mounted on the outside of the iron yokes. Outside the magnet the magnetic field is expected to be inhomogeneous and below 0.005 T. The possibility of reusing MA-PMTs from the K2K experiment is being discussed. MCP-PMTs have the advantage to allow unshielded operation in magnetic fields without significant loss in performance. However, only limited experience with MCP-PMTs exists and further suitability studies are required to look at gain stability and dead time issues.
Alternatively, SiPMTs (as described in section 5.2.4) can be directly attached to the scintillator to read out the WLS fibers. The output of the SiPMTs would then be multiplexed to reduce the effective segmentation of the SMRD and to reduce the number of electronics channels to a level dictated by an optimization of physics requirements and cost. The choice of photo-sensor which will work inside or near a 0.2 T magnetic field is a common task for all inner ND280 detector components that use scintillator technology.

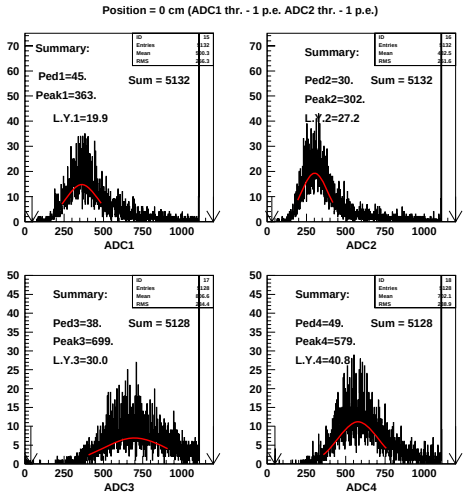


Figure 8.8: Preliminary ADC spectra from light yield measurements for cosmic muons intersecting the center of the scintillator slab [59]. The light yield (L.Y.) is given in units of photo electrons. The various panels correspond to different scintillator and fiber configurations.

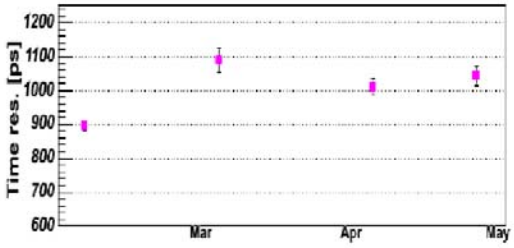


Figure 8.9: The timing resolution (in pico seconds) of MIP signals as function of calendar month for a prototype detector with 2 cm fiber spacing.

**Readout Electronics and Data Acquisition** The principal aim of the electronic system is to digitize the electric signal from the photo-detectors. Moreover, it can also supply the high voltages to the photo-detectors and provide monitor and control functions. The electronics has to measure and digitize the signal from each photo-detector exceeding a threshold, recording amplitude and hit time with a relative accuracy at the sub-nanosecond level, and to flag hits potentially corrupted by pileup from a previous hit. The electronics is required to cause no dead time during a spill so as not to miss any events during a spill. All events shall be zero suppressed and only channel data above a programmable threshold shall be read-out.

These requirements are very similar to those of the FGD, the P0D, and the Ecal and it is planned to use the same electronics. The Fermilab TRIP-T chip is a good candidate and is described along with more detailed requirements and characteristics in Section 5.2.4.

**Detector Trigger** The main event trigger will be formed from a coincidence of the overall spill trigger with individual scintillator panel triggers. Each scintillator panel will self trigger if a signal exceeds a set pulse threshold. Based on these self trigger signals coincidence triggers between two or more scintillator panels separated by iron layers can be constructed. This type of trigger can be used for calibration purposes as the constant flux of cosmic ray muons penetrates the detector.

### 8.2.2 Detector Calibration

Three different calibration systems, each aiming at a different task, are planned. These three systems are a light-injection system, cosmic ray muons, and a radioactive source system.

The baseline design of the light-injection system is based upon pulsed blue light-emitting diodes (LEDs) and aims to map the gain curve of the photo-multipliers, monitor short-term gain drifts, and to confirm the optical path integrity (e.g. check that no fibers are broken). We anticipate a system very similar to what is currently used for the SciBar [47] detector of the K2K experiment or in the MINOS [62] experiment.

The intensity of vertical muons above 1 GeV at sea level is $I \sim 1\ \mathrm{cm}^{-2}\mathrm{min}^{-1}$ [65]. Given a detector surface of $760 \times 560\ cm^2$, a total of 425,000 muons per minute (7,000 muons per second) hit the detector, and about 100 muons per second penetrate an individual scintillator. This constant flux of MIPs can be used to continuously monitor the response of the horizontally oriented scintillator slabs. If the position of individual cosmic muons can be derived accurately with the inner detector components, the attenuation of the WLS fibers can be measured and compared to measurements before installation.

A radioactive source system allows an absolute calibration of each scintillator-WLS-fiber unit. Short stainless steel tubes can be attached at either end of the scintillator slab and serve as a guide track for a radioactive source. This technique has been used by BaBar [63] and MINOS [64] where it helped to reduce the systematic uncertainties significantly.

### 8.2.3 Installation of active SMRD components

The mechanical implementation of the SMRD will allow access to each scintillator slab after the start of the experiment, so that repairs and adjustments can be accomplished. It is planned to place the scintillator slabs into thin aluminum drawers. Each of the drawers will fit into a gap in the iron yokes and individual drawers will be connected to each other with flexible but sturdy spacers. This will allow installation and access for repair to all scintillator slabs despite the limited detector access space and space constraints imposed by the iron yokes. Figure 8.10 shows a sketch of such

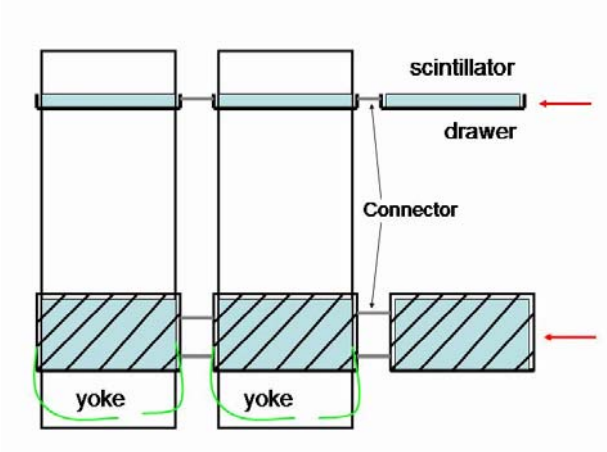


Figure 8.10: Illustration of the drawer system which will allow deployment and retrieval of the scintillator slabs.

a drawer configuration. The drawers provide mechanical stability and will also serve to protect the light tight wrapping from tear during installation and potential maintenance retrieval. It is anticipated that wavelength shifting fibers would exit the detector in between each (or every other) iron yoke. The MA-PMTs would be mounted at a distance from the iron yokes to minimize the impact of the magnetic field on their performance.

# Part I

# Appendix

# Appendix A

# $\pi^0$ detection in the tracker region

There are obvious advantages in measuring $\pi^0$ in the tracker region. The FGD+TPC detectors allows to measure the entire event at a time and allows to compare the different $\pi$ production with the same detector systematics and acceptances. The difficulty of achieving a complete measurement is the measurement of the $\pi^0$ production. To achieve these goals an electromagnetic calorimeter with some pointing capabilities has to be build surrounding the inner tracker region.

As an example, a set of pre-shower detector (PSD) and an electromagnetic calorimeter (Ecal) is considered which surrounds the entire tracking region. Photons from $\pi^0$ produced in FGD are detected by PSD/Ecal. PSD provides the starting point of the electromagnetic (EM) shower while Ecal provides a point of the shower-maximum. By connecting these two points, the direction of photon can be reconstructed. Key issues to be satisfied for the $\pi^0$ detection are as follows: (1) The $\pi^0$ vertex can be reconstructed so that the interaction in FGD and in other materials are separated, (2) background events such as events which occur in the surrounding materials can be rejected, and (3) events which have more than one $\pi^0$ can also be rejected.

For (1), the large gap of $\sim$ 1m between water-FGD and plastic-FGD helps us identifying which side the photons are coming from. As for (2), energy flow of photon can be used to identify if the event happens inside the tracking region or not. As for (3), high detection efficiency for photons in PSD/Ecal will help us rejecting the events which have more than two photons. The main background would be the events which happens inside the PSD and the FGD support structure close to its inner surface. By implementing a gap of $20-30$ cm between FGD and and PSD/Ecal, backgrounds from outside FGD fiducial can be separated for a vertex resolution of about $20-30$ cm. A Monte Carlo simulation (Toy-MC) was performed to study if such a vertex resolution is feasible.

In the Toy-MC $\pi^0$ is generated in the FGD volume with $\pi^0$ momentum given by NC-1$\pi^0$ events in NEUT simulation. The size of FGD is assumed to be 200 cm$\times$200 cm$\times$30 cm. Two gammas from $\pi^0$ decays are generated in the $\pi^0$ rest frame and are propagated to the PSD/Ecal and their crossing points with PSD/Ecal are calculated. PSD plane is assumed to be at $\pm 125$ cm in $x$ and $y$ and $\pm 100$ cm in $z$, and Ecal planes are set by 30 cm outside PSD planes. The each intersection is smeared in parallel directions to the plane by Gaussian function with $\sigma_{x,y}$ and $\sigma_z$ to make a reconstructed hit point. The energy of $\gamma$s is also smeared by Gaussian with $\sigma_E = 10\%/\sqrt{E\,[\mathrm{GeV}]}$. Three sets of values for $\sigma_{x,y}$ and $\sigma_z$ used in this study are summarized in Table A.1.

Figure A.1 shows the resulting vertex and momentum resolution for Setting 1. The results for other settings are summarized in Table A.1. With the photon direction resolution of $\sim 15$ degrees, the $\pi^0$ vertex resolution is $\sim 20$ cm in the FGD (xy) plane, which is comparable with the gap between the FGD and PSD/Ecal. The z resolution is $\sim$30 cm, which would be sufficient in sepa-

Table A.1: Summary of the settings for hit position resolution in Toy-MC study and the resulting vertex and momentum resolution with FGD + PSD + Ecal option.

| input hit point resolutions | | | | |
|---|---|---|---|---|
| | resolution@conversion | | resolution@shower-max | |
| Setting # | $\sigma_{x,y}$ [cm] | $\sigma_z$ [cm] | $\sigma_{x,y}$ [cm] | $\sigma_z$ [cm] |
| Setting 1 | 2.0 | 10.0 | 5.0 | 10.0 |
| Setting 2 | 2.0 | 2.0 | 5.0 | 10.0 |
| Setting 3 | 5.0 | 5.0 | 10.0 | 10.0 |

| resulting resolutions | | | | | |
|---|---|---|---|---|---|
| | | $\pi^0$ vertex resolution | | $\pi^0$ momentum resolution | |
| Setting # | $\sigma_{\theta_\gamma}$ [deg.] | $\sigma_{x,y}$ [cm] | $\sigma_z$ [cm] | $\sigma_p/p$ [%] | $\sigma_\theta$ [deg.] |
| Setting 1 | 15 | 18.0 | 28.6 | 6.4 | 18.0 |
| Setting 2 | 13 | 17.4 | 22.3 | 6.3 | 16.8 |
| Setting 3 | 22 | 30.7 | 30.4 | 6.5 | 24.3 |

rating the FGD from Ecal or another FGD. This indicates that we can select the $\pi^0$ events inside the FGD with the moderate photon direction resolution in PSD/Ecal.

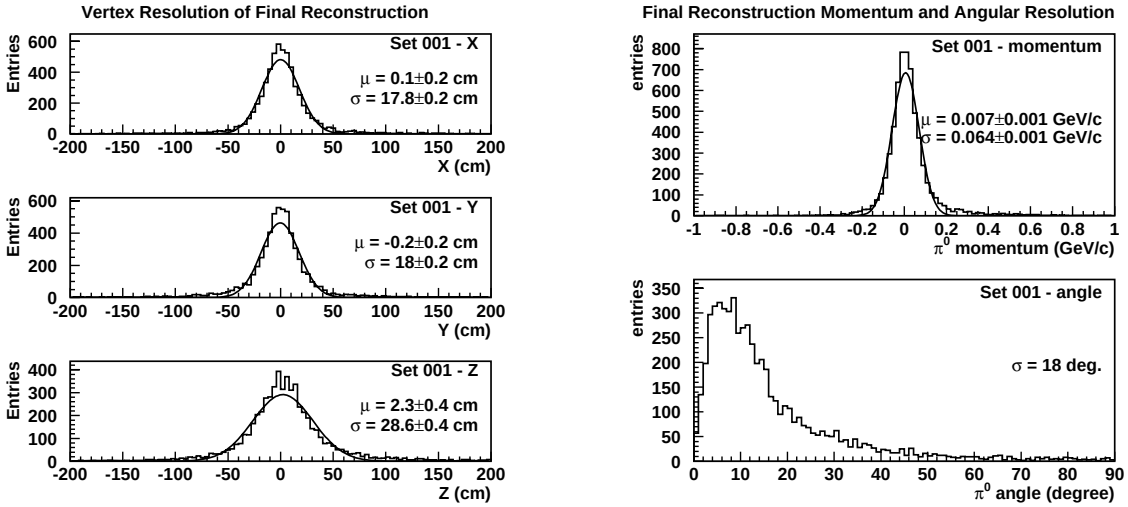


Figure A.1: The vertex and momentum resolution of $\pi^0$ reconstruction for Setting 1.

# Appendix B

# J-PARC Beam Power Expectation

The expected beam power of the J-PARC accelerator is shown in Figure B.1, which shows various JPARC beam intensity options. There are four solid curves with different colors, (Please ignore the dotted curve.), each of which corresponds to a different beam power. The 0.67 MW full power option previously presented publicly (different from the one in LOI) is shown by the line with black squares (the lowest beam power option). The orange curve with triangles shows the case for a factor of two increase in the beam power. A factor of two improvement can be achieved by doubling the number of proton bunches (for example by doubling the harmonics in the main ring from 9 to 18) while the beam intensity is relatively low. When the beam intensity approaches the original design value, we can instead double the beam intensity by increasing the repetition rate (instead of increasing the number of proton bunches), thereby keeping the energy deposit to the target and beam window within the current design of the neutrino beam line. In this case, a beam power of 1.34 MW at full intensity would be achievable. There are several other accelerator running options currently being studied by the J-PARC accelerator group. As an example, choosing the option currently considered most likely by the JPARC accelerator group, we assume that the beam intensity upgrade curve is the one shown by the orange triangles in Figure B.1.

With this configuration, which corresponds to a doubling of the previously presented beam power, the sensitivity to $\sin^2 2\theta_{13}$ as a function of Japanese fiscal year (JFY: April 1 to March 31) is shown in Figure B.2. Also shown in this figure, for comparison, is the sensitivity as a function of year for the previous option as shown by the black line in Figure B.1. These plots explicitly take into account the beam-turn-on profile, and for that reason, the limit improves at a different rate than that shown in the right panel of Figure 1.11 .

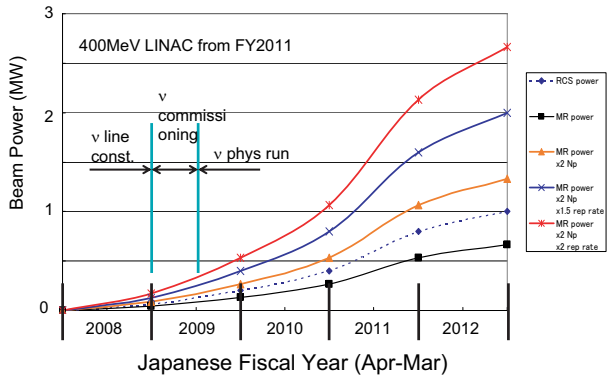


Figure B.1: Expected J-PARC beam power upgrade for various accelerator options.

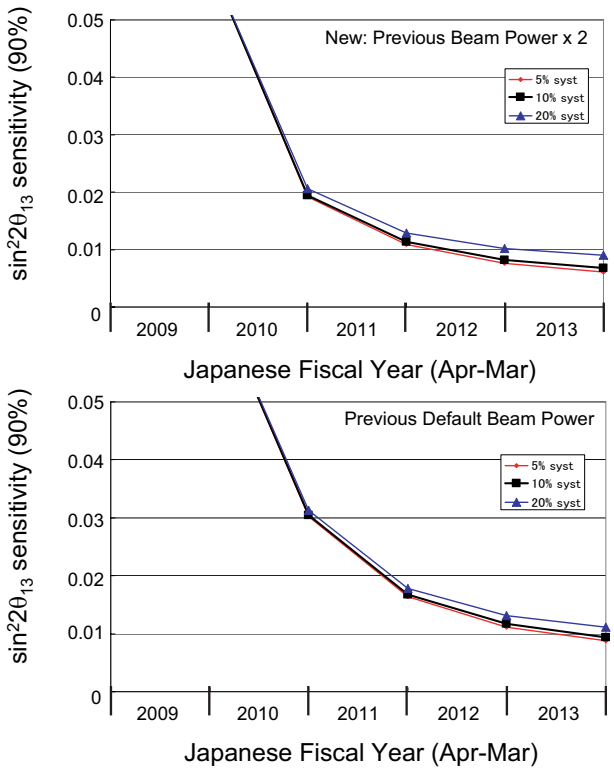


Figure B.2: Sensitivity to $\sin^2 2\theta_{13}$ as a function of year considering the beam power profile. The top plot (corresponding to the orange line on Figure B.1) is for the case where the beam power is doubled with respect to the previous default option shown as the bottom plot (corresponding to the black line in Figure B.1).

# List of Figures

# List of Tables

# Bibliography


[1] B. Cleveland, *et al.*, Astrophys. J. **496**, 505 (1998)

[2] Y. Fukuda, *et al.*, Phys. Rev. Lett. **77**, 1683-1686 (1996);
K.S. Hirata, *et al.*, Phys. Rev. D **44**, 2241-2260 (1991)

[3] V. Gavrin, *Results from the Russian American Gallium Experiment (SAGE)*, VIIIth International Conference on Topics in Astroparticle and Underground Physics (TAUP 2003), Seattle, September 5–9, 2003;
J.N. Abdurashitov *et al.*, J. Exp. Theor. Phys. **95**, 181 (2002);
the latest SAGE results were presented by C. Cattadori, *Results from Radiochemical Solar Neutrino Experiments*, XXIst International Conference on Neutrino Physics and Astrophysics (Neutrino 2004), Paris, June 14–19, 2004.

[4] E. Bellotti, *The Gallium Neutrino Observatory (GNO)*, VIIIth International Conference on Topics in Astroparticle and Underground Physics (TAUP 2003), Seattle, September 5–9, 2003;
M. Altmann *et al.*, Phys. Lett. B **490**, 16 (2000);
W. Hampel *et al.*, Phys. Lett. B **447**, 127 (1999)

[5] Y. Ashie, *et al.*, Phys. Rev. D **71**, 112005 (2005);
Y. Fukuda, *et al.*, Phys. Rev. Lett. **81**, 1562-1567 (1998)

[6] Q.R. Ahmad *et al.*, Phys. Rev. Lett. **87**, 071301 (2001);
Q.R. Ahmad *et al.*, Phys. Rev. Lett. **89**, 011301 (2002);
S.N. Ahmed *et al.*, Phys. Rev. Lett. **92**, 181301 (2004);
nucl-ex/0502021, submitted to Phys Rev C

[7] K. Eguchi*et al.*, Phys. Rev. Lett. **90**, 021802 (2003);
K. Eguchi *et al.*, Phys. Rev. Lett. **94**, 081801 (2005)

[8] E. Aliu *et al.*, Phys. Rev. Lett. **94**, 081802 (2005)

[9] Z. Maki, N. Nakagawa, and S. Sakata, Prog. Theor. Phys. **28**, 870 (1962);
V. Gribov and B. Pontecorvo, Phys. Lett. B **28**, 493 (1969)

[10] S. P. Mikheyev and A. Yu. Smirnov, Sov. J. Nucl. Phys. **42**, 913 (1985);
L. Wolfenstein, Phys. Rev. D **17**, 2369 (1978)

[11] C. Athanassopoulos, *et al.*, Phys. Rev. C542685-27081996, nucl-ex/9605001;
A. Aguilar, *et al.*, Phys. Rev. D641120072001

[12] B. Armbruster, *et al.*, Phys. Rev. D **65**, 112001 (2002);
E.D. Church, K. Eitel, G.B. Mills, M. Steidl, Phys. Rev. D **66**, 013001 (2002)

[13] E. Church, *et al.*, nucl-ex/9706011.

[14] M. Fukugita and T. Yanagida, Phys. Lett. B **174**, 45 (1986)

[15] M. Apollonio, *et al.*, Eur. Phys. J. **C27**, 331-374 (2003);
M. Apollonio, *et al.*, Phys. Lett. B **466**, 415-430 (1999).

[16] P-875: A Long Baseline Neutrino Oscillation Experiment at Fermilab, D. Ayres et al.. MINOS Proposal, NuMI-L-63. `http://www.hep.anl.gov/ndk/hypertext/numi_notes.html`.

[17] The OPERA experiment, H. Pessard, *et al.* (OPERA), hep-ex/0504033.

[18] The ICARUS experiment, a second-generation proton decay experiment and neutrino observatory at the Gran Sasso Laboratory, Arneodo, F, *et al.* (ICARUS), hep-ex/0103008.

[19] http://jkj.tokai.jaeri.go.jp/index-e.html

[20] Y. Fukuda, *et al.*, Nucl. Instrum. Methods **A**, 501 (2003)418-462

[21] D. Beavis, A. Carroll, I. Chiang, *et al.*, Proposal of BNL AGS E-889 (1995).

[22] S. Fukuda *et al.* (Super-Kamiokande Collaboration), Phys. Rev. Lett. **85**, 2000 (3999-4003)

[23] R. Ishida, Talk at the T2K280m meeting, October 25, 2003.
http://www-he.scphys.kyoto-u.ac.jp/ nakaya/jparc/index.htm
http://www-he.scphys.kyoto-u.ac.jp/ nakaya/jparc/doc/ND280m_Oct25-27-2003/r_ishida.pdf

[24] S.J.Barish et al, Phys. Rev. D**19**:2521,(1979).

[25] J. Spitz and E. D. Zimmerman, private communication.

[26] NuMI Technical Design Handbook, Chapter 4.4, 4.5

[27] RD42 Collaboration web page, `http://rd42.web.cern.ch/RD42/`

[28] Yu. G. Kudenko *et al.* Nucl. Instrum. Methods **A469**, 340-346 (2001)

[29] O. Mineev et al., NIM, A494 (200) 362-368; physics/0207033.

[30] N. Yershov et al., physics/0410080.

[31] T2K-TPC Group, *T2K TPC Feasibility Report*, T2K-TPC Note-001, December 2004.

[32] E. Radicioni, *Design considerations on a TPC for T2K-nd280m*, T2K-TPC Note-002, December 2004.

[33] H. Kuroiwa, et al., *The influence of oxygen contamination on the performance of a mini-jet-cell-type drift chamber for the JLC-CDC*, Nucl. Instrum. Methods **A**, 516 (2004)377.

[34] J. Wendland, *Electrostatic simulations of the TPC field cage designs*, T2K TPC-note-XXX.

[35] FEMLAB 3.1, COMSOL Inc., http://www.comsol.com.

[36] Sabine Blatt, "Konstruktion und Inbetriebnahme eines Feldkäfigs für eine TPC", Rheinisch-Westfälische Technische Hochschule Aachen (2004).

[37] W. Blum, L. Rolandi, "Particle detection with drift chambers", Springer-Verlag (1993).

[38] C. Altunbas, et al., *Construction, test and commissioning of the triple-gem tracking detector for compass*, Nucl. Instrum. Methods **A**, 490 (2002)177.

[39] A. Magnon et al., *Tracking with 40x40-cm**2 micromegas detectors in the high energy, high luminosity compass experiment*, Nucl. Instrum. Methods **A**, 478 (2002)210.

[40] I. Giomataris et al., *Micromegas in a Bulk*, physics/0501003, January 2005.

[41] E. Auge et al., *The front end board for the ATLAS liquid argon calorimeter*, 4th Workshop on Electronics for LHC Experiments (LEB 98), Rome, Italy, 21-25 Sep 1998.

[42] D. Breton, et al., *A 16 bit 40-Mhz readout system based on dual port analog memories for LHC experiments*, 2nd Workshop on Electronics for LHC Experiments, Balatonfured, Hungary, 23-27 Sep 1996.

[43] D. Karlen, P. Poffenberger and G. Rosenbaum, *TPC performance in magnetic fields with GEM and pad readout*, accepted by Nucl. Instr. Meth. A, arXiv:physics/0509051.

[44] D. Karlen, *Study of momentum resolution in the T2K TPC with full simulations*, T2K TPC-note-003.

[45] D. Karlen, *Update to the T2K TPC momentum resolution study - symmetric pad geometries*, T2K TPC-note-004.

[46] A.H. Walenta, et al., Nucl. Instrum. Methods , 161 (1979)45.

[47] K. Nitta et al.,The K2K SciBar detector, Nucl. Instrum. Methods **A**, 535 (2004)147-151

[48] H. Maesaka, The K2K SciBar Detector,

[49] http://www.zinsser-analytic.com

[50] G.Bondarenko,V.Golovin, M.Tarasov, Patent for invention in Russia No. 2142175, 1999.

[51] G.Bondarenko et al., Nucl. Phys. Proc. Suppl., 61B (1998)347.

[52] A. Akindinov et al., NIM, A494 (2002) 474.

[53] G.Bondarenko et al., NIM, A442 (2000) 187.

[54] V.Golovin, V.Saveliev, NIM, A518 (2004) 560.

[55] V. Andreev et al., NIM, A549 (2005) 368.

[56] F. Sanchez, Talk at the T2K280m meeting, October 7, 2004

[57] N.Yershov *et al*. arXiv: physics/0410080

[58] O. Mineev *et al.* arXiv: physics/0207033

[59] Yu. Kudenko, private communication, Feb. 2005

[60] ZEUS Experiment

[61] Proceedings of teh Symposium on 'Detector Research and Development for the Superconducting Super Collider', October 1990 ; editors: T. Dombeck, V. Kelly, G.P. Yost; World Scientific Publishing

[62] P.Adamson *et al.*, hep-ex/0204021.

[63] BaBar Collaboration, B. Aubert *et al.*, Nucl.Instrum.Meth.A 479 1, 2002.

[64] The MINOS Technical Design Report

[65] Particle Data Group, S. Eidelman *et al.*, Phys. Lett. B **592**, 1 (2004)